

Fractality and topology of optical singularities

Kevin O'Holleran
MSci

Submitted in fulfilment of the requirements for
the Degree of Doctor of Philosophy

Department of Physics & Astronomy
Faculty of Physical Sciences
University of Glasgow

October 27, 2008

© K. O'Holleran 2008

Abstract

Optical singularities are points in complex scalar and vector fields where a property of the field becomes undefined (singular). In complex scalar fields these are phase singularities and in vector fields they are polarisation singularities. In the former the phase of the field is singular and in the latter it is the polarisation ellipse axes. In three dimensions these singularities are lines and natural light fields are threaded by these lines.

The interference between three, four and five waves is investigated and inequalities are given which establish the topology of the singularity lines in fields composed of four plane waves. Beyond several waves, numerical simulations are used, supported by experiments, to establish that optical singularities in speckle fields have the fractal properties of a Brownian random walk. Approximately 73% of singularity lines percolate random optical fields, the remainder forming closed loops. The statistical results are found to be similar to those of vortices in random discrete lattice models of cosmic strings, implying that the statistics of singularities in random optical fields exhibit universal behavior.

It is also established that a random superposition of plane-waves, such as optical speckle, form singularities which not only map out fractal lines, but create topological features within them. These topological features are rare and include vortex loops which are threaded by infinitely long lines and pairs of loops that form links. Such structures should be not only limited to optical fields but will be present in all systems that can be modeled as random wave superpositions such as those found in cosmic strings and Bose-Einstein condensates.

Also reported are results from experiments that generated compact vortex knots and links in real Gaussian beams. These results were achieved through the use of algebraic knot theory and random search optimisation algorithms.

Finally, polarisation singularity densities are measured experimentally which confirm analytic predictions.

Author's declaration

I hereby declare that this thesis is the result of my own work, except where explicit reference is made to the work of others, and has not been presented in any previous application for a degree at this or any other institution.

.....

Kevin O'Holleran

Contents

Contents	3
List of Figures	6
List of Tables	9
1 Introduction	11
1.1 A brief history	11
1.2 Creating singularities	16
1.3 Optical angular momentum	18
1.4 Thesis format	20
2 Theory	22
2.1 Phase singularities in scalar fields	22
2.1.1 Basic properties	22
2.1.2 Reconnections	26
2.1.3 Vortex point densities	27
2.2 Polarisation singularities	28
3 Experimental apparatus	31
3.1 General apparatus	31
3.2 Spatial Light Modulator	33
3.3 Computer Generated Holograms	34
3.4 Phase measurements	38
3.5 Vortex finding	39
3.6 Apparatus test and examples	41
3.6.1 Propagation of a Gaussian spot	41
3.6.2 Laguerre-Gauss beams	42
3.7 Vortex structure as an indicator of beam purity	45
3.8 Polarisation measurements	46
3.8.1 Measuring Stokes parameters	47

<i>Contents</i>	4
3.8.2 Example polarisation measurements	49
3.9 Summary	51
4 Illustrations of vortices in 3D	52
4.1 The elliptic umbilic diffraction catastrophe	53
4.2 Vortex lines and a varying parameter	55
4.2.1 Four wave interference	56
4.2.2 Spiral phase plate	59
4.2.3 Vortex links	61
4.3 Discussion	62
5 Plane-wave interference	63
5.1 Phasors	63
5.2 Interference between two and three waves	65
5.3 Interference between four waves	67
5.4 Experimental results	70
5.5 Interference between more waves	71
5.6 High-order vortices and plane waves	72
5.7 Conclusions	73
6 Random wave-fields	76
6.1 Model	77
6.1.1 Talbot cells	78
6.1.2 Volume resolution	79
6.1.3 Vortex Sorting	80
6.2 Speckle fields	81
6.2.1 Model validation	86
6.3 Speckle model results	87
6.3.1 Loop to line length ratio and percolation	87
6.3.2 Fractality	89
6.3.3 Scale invariance	95
6.4 Experimental results	95
6.5 Discussion	101
7 Vortex topology in random fields	103
7.1 Links and threadings	103
7.1.1 Identifying crossing points	104
7.1.2 Links in speckle	105
7.1.3 Threadings in speckle	107
7.1.4 Results	108
7.2 Knots	109

7.2.1	Alexander polynomials	110
7.2.2	Multiple crossings	111
7.3	Test curves	111
7.4	Absence of knots	113
7.5	Discussion	115
8	Knots and links in the lab	116
8.1	Embedding algebraic knots in Gaussian beams	116
8.1.1	Algebraic fibred knots	117
8.2	Modal composition of structures	119
8.3	Optimisation for experiment	120
8.3.1	Search parameters	120
8.3.2	Merit function	123
8.4	Results	124
8.5	Discussion	129
9	Polarisation Singularities	131
9.1	Polarisation singularity statistics	131
9.2	Distinguishing singularity type	132
9.3	Experiment	133
9.4	Numerical experiments	134
9.5	Results	137
9.6	Summary	139
10	Conclusions	141
	Publications	143
	Bibliography	145

List of Figures

1.1	Ray caustic digram by daVinci	12
1.2	Wavefront interference sketch by Thomas Young	13
1.3	First diagram showing an optical phase singularity	14
1.4	Two methods of generating optical singularities	16
1.5	Helical phasefronts around an optical vortex	18
2.1	Vortices in phase/intensity cross-sections	23
2.2	Real and imaginary zero contours in 2D and 3D	24
2.3	Topological charge of vortices in 3D	25
2.4	Reconnections as a topology changing mechanism	26
2.5	Poincaré sphere	28
2.6	Classification of polarisation singularities	29
2.7	Elliptic and hyperbolic configurations of polarisation singularity	29
3.1	Apparatus for intensity and phase acquisition	32
3.2	Spatial light modulator	33
3.3	Basic hologram calculation	34
3.4	Blazed holograms	35
3.5	Intensity modulation of HG modes	37
3.6	Intensity modulation LG modes	37
3.7	Phase measurement process	39
3.8	Vortex finding from real data	40
3.9	Full 3D acquisition of phase and intensity of Gaussian beam . .	41
3.10	Laguerre-Gauss modes	42
3.11	Full complex field acquisition of LG_0^1 mode	43
3.12	Full complex field acquisition of LG_0^2 mode	43
3.13	Azimuthal phase values near axis of measurements	44
3.14	Vortex line structure in calculated and measured fields	46
3.15	Apparatus for measuring Stokes parameters.	46
3.16	Perspex ruler between crossed polarisers	49
3.17	Polarisation measurements of glass plate under stress — linear .	50

3.18	Polarisation measurements of glass plate under stress — circular	51
4.1	Elliptic umbilic diffraction catastrophe in 3D	53
4.2	Vortex lines in four wave interference	57
4.3	Vortex lines emerging from a spiral phase plate	58
4.4	Linked vortices under perturbation	60
5.1	Phasors in two-wave interference	64
5.2	Phasors in three-wave interference	65
5.3	Vortex structure from three-wave interference	66
5.4	Phasors in four-wave interference	68
5.5	Vortex topologies in four-wave interference	68
5.6	Reconnections in four-wave interference	69
5.7	Experimentally measured vortex structure in four-wave interference	71
5.8	Complexity in vortex structure from 5-wave interference	72
5.9	Charge 2 vortex from 5 waves	74
5.10	Charge 3 vortex from 7 waves	75
6.1	Periodic cells defining topology	78
6.2	k -space construction for periodic fields	79
6.3	Typical 27×27 k -space used in calculations	81
6.4	Intensity cross sections of Talbot cells	82
6.5	Full 21 k -space grid Talbot cell	83
6.6	Full 27 k -space grid Talbot cell	84
6.7	Full 41 k -space grid Talbot cell	85
6.8	Vortex point density as model parameters vary	86
6.9	Vortex loop to line length ratio	87
6.10	Individual vortex lines and displacement from origin	89
6.11	Fractal dimension of vortex lines in model	90
6.12	Brownian walks and vortex lines	92
6.13	Persistence length of random vortex lines	93
6.14	Radius of gyration of vortex loops vs. length	93
6.15	Vortex loop size distribution in model	94
6.16	Apparatus for intensity and phase acquisition of speckle	96
6.17	Example of cross-section intensity and phase measurements of speckle	97
6.18	Experimental results of vortex lines in speckle	98
6.19	Unit volume of speckle from experiment and model	99
6.20	Complex field correlations in speckle	100
6.21	Poisson distribution for number loops in sampled volume	102
7.1	Chord angle plot between two curves	104

7.2	Some linked vortex lines identified in model data	106
7.3	Three component link found in simulated speckle	107
7.4	Probability of a vortex loop being unthreaded	108
7.5	Multiple crossings in planar diagrams	112
7.6	Trefoil knot and chord plot	113
7.7	Figure eight knot and chord plot	114
8.1	Ideal vs. optimised beams: trefoil knot	121
8.2	Ideal vs. optimised beams: cinquefoil knot	122
8.3	Experimental result of a compact Hopf link	125
8.4	Experimental result of a compact trefoil knot	126
8.5	Trefoil fibre surface from experiment	127
8.6	Experimental result of a cinquefoil knot in a beam	128
8.7	Accidental experimental result of a twist link	129
9.1	Production of a polarisation speckle field	134
9.2	Streamlines around polarisation singularities	135
9.3	C-lines in polarisation speckle	136
9.4	L-surfaces in polarisation speckle	136
9.5	Polarisation singularity composition around a C-loop	137

List of Tables

9.1	C-point type ratios, experiment and predicted	138
9.2	Experimentally measured C-line ratios	138

Acknowledgements

This thesis would not have been possible, first and foremost, if not for the enthusiasm and dedication of my supervisor Miles Padgett. I would also like to thank and acknowledge Mark Dennis: without his vast knowledge and motivation, this thesis would not contain the quality of research that it does. I would also like to acknowledge Florian Flossmann, as the chapter on polarisation singularities owes its existence to his ingenuity in the laboratory and skill with Mathematica. As I continue my ‘withouts’ I must thank Johannes Courtial who has been a wonderful second supervisor and whom without, it just wouldn’t have been as much fun.

The greatest instrument in making the last four years as enjoyable as it was productive, and which is far greater than the sum of its parts: the Optics group. Listed in no particular order — thank you to Eric Yao, Sonja Franke-Arnold, Jonathan Leach, Graham Gibson, Ken Skeldon, Lesley McMillan, Martin O’Dwyer, Graeme Whyte, Laura Thomson, Claire Patterson, John Nelson, Steven Keen, Aline Vernier, Alisdair Hamilton, Daryl Preece and Barry Jack.

I also owe thanks to many guests that have visited our group over the years. Most importantly to Kurt Wulff, who I became good friends with, and to Gary Ruben who I am indebted to for his L^AT_EX expertise.

There is an Optics outsider I need to thank — Dan Clements, for providing me with a little time each day to have a coffee and talk about our work and whatever else was on our minds.

Finally, I would like to thank my parents, for all the wonderful and miscellaneous ways that they have helped over the years.

CHAPTER 1

Introduction

“Singularity is almost invariably a clue”

— Arthur Conan Doyle

Adventures of Sherlock Holmes, 1892

1.1 A brief history

Singularities have always been of great importance to physicists. They point the way towards new physics by highlighting the limitations of the current theory. The diffraction catastrophes of ray optics [Nye99] were understood through wave optics. Waves, however, come with their own brand of singularities. This thesis will cover two different types of optical singularities: phase singularities in complex scalar waves and polarisation singularities in vector waves. The former will be covered extensively, with the latter acting as an epilogue showing how the properties of phase singularities are inherited by their vector counterpart.

To open with a very old diagram, Fig. 1.1 shows what is possibly the first ray caustic diagram. It illustrates how equally spaced parallel straight lines can reflect from a surface such that they converge along a curved line. This

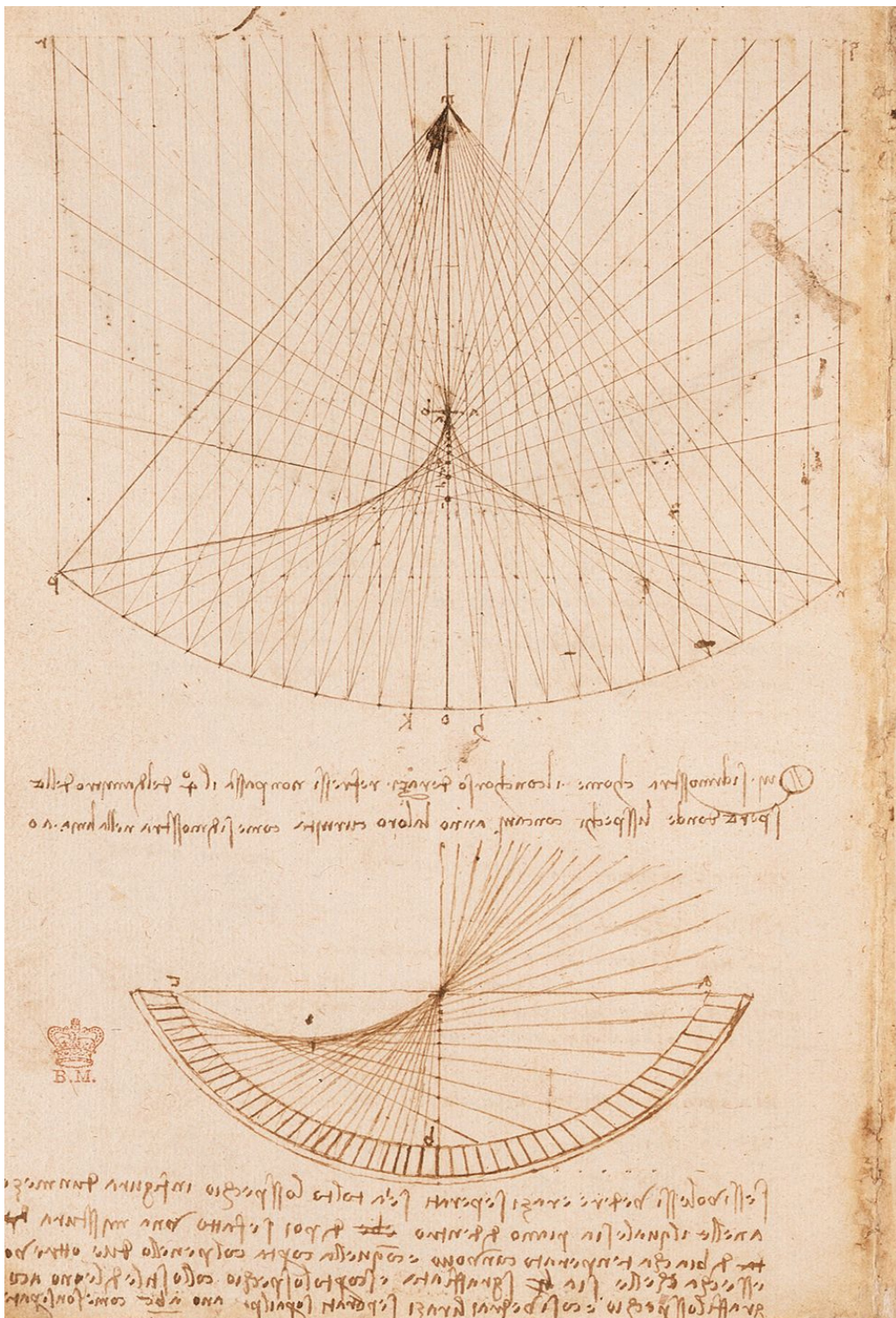


Figure 1.1: A drawing of a caustic by Leonardo da Vinci c. 1508. Possibly the first caustic/ray diagram drawn (British Library: codex Arundel 263. folio 87v).

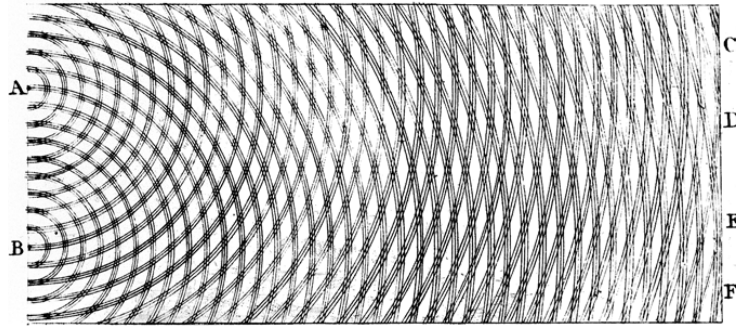


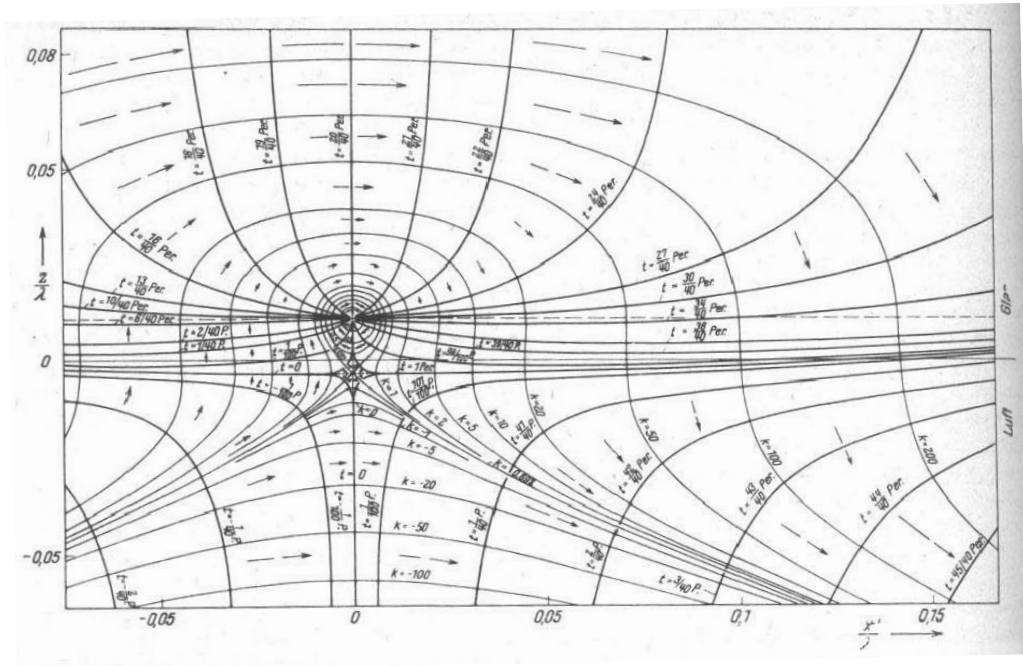
Figure 1.2: Thomas Young's sketch of wavefronts emanating from two slits, which he presented to the Royal Society in 1803.

line is called a caustic and in ray optics it is a line of infinite intensity (in fact the density of rays rises inversely with the distance from the caustic which is specifically known as a fold caustic). Caustics are the singularities of ray optics and are ubiquitous: they can be observed on the surface of fluid in a cup (caused by the reflection of natural light from the cup rim) or on swimming pool walls, and they are the mechanism behind rainbows [Nye99].

Wave optics explains why the intensity along a caustic does not rise infinitely. As Young demonstrated in 1803 (see Fig. 1.2) a feature of wave superposition is that one plus one does not necessarily equal two. In general, when three or more scalar waves interfere in space, complete destructive interference occurs on lines. These lines go by various names in the literature: nodal lines, phase singularities, wave dislocations and optical vortices. These terms are all correct and in different scenarios each can be used appropriately.

The singular nature of these nodes arises from the argument of the complex number describing the wave becoming undefined (singular), and nearby all phases between 0 and 2π occur, increasing in either a clockwise or counterclockwise sense [NB74]. The term vortex derives from the fact that the Poynting vector rotates around the singularity — making it a vortex of optical energy [CGR89].

Given that optical vortices arise when there are multiple wave components present and that each of the infinitely many rays forming a caustic is locally



waves and 1931 for electromagnetic waves [Dir31], the first image showing phase singularities in optics appeared in a paper by Wolter in 1951, which mentions a few properties of ‘special null points’ in the optical field while describing reflections from a half plane.

However, it was not until a paper by Nye and Berry in 1974 [NB74] that these “Dislocations in wave-trains” were studied in their own right as a physical phenomenon in waves, and more specifically in optics. The motivation to develop this theory was to understand radiowave reflections from the bottom of the Antarctic sheet. Experiments were conducted to replicate the phenomenon in ultrasonic pulses reflected from a rough surface — ultrasound’s relatively low frequency allowing phase observations to be made.

The following two decades saw various papers describing phase singularities in diffraction catastrophes [BNW79] and their statistics in Gaussian random waves [Ber78]. During this time polarisation singularities in electromagnetic wave fields were also introduced in the literature [Nye83b, Nye83a]. Other singularities of interest studied in the 1980s were singular filaments in chemical waves (here the phase is that of a chemical excitation cycle), superfluid vortices [Sch88] and cosmic strings [VV84]. A trilogy of papers by Winfree and Strogatz [WS83a, WS83b, WS83c] discusses the topology of the singularities (specifically in chemical waves) in three dimensions and the possibility of having knotted lines.

This leads on to the most recent work in optical vortices which does involve topology. In 2001 Berry and Dennis constructed a ‘recipe’ for creating knotted or linked phase singularities in monochromatic, or more generally, Helmholtz waves [BD01b, BD01a]. This was later confirmed by Leach et al. [LDCP04a, LDCP05] who created these structures in real Gaussian beams. Of course, to achieve this they needed to be able to create singular beams in the lab.

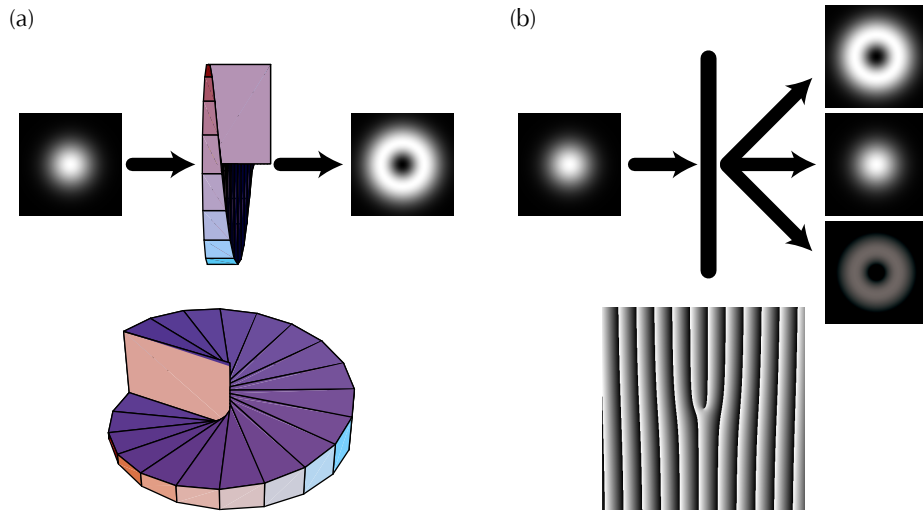


Figure 1.4: Illustration of a Gaussian beam incident on (a) a spiral phase plate of height $\lambda\theta/2\pi$ and (b) a hologram with phase modulation $\text{mod}2\pi|\lambda\theta/2\pi + \alpha x|$ where the second term adds a blazed diffraction grating, to preferentially diffract light into the positive first order.

1.2 Creating singularities

Alongside the theoretical work between 1980 and 2000 was an interest in realising singular beams experimentally. The first example of this came in 1979 when Vaughan [VW79] studied the properties of light beams having a helical phase structure, which (by inference) must contain an optical vortex along the beam axis.

In 1989 Coulet et al. [CGR89] used the term “optical vortex” to describe a possible laser mode that could occur in cavities with large Fresnel number. The natural laser mode containing an optical vortex is a Laguerre-Gaussian mode. Like the Hermite-Gaussian modes, the Laguerre-Gaussian modes are orthogonal to each other and form a complete basis set from which any arbitrary field distribution may be decomposed. The most iconic Laguerre-Gaussian mode, LG_0^1 , often referred to affectionately as the ‘doughnut mode’, comprises a single annular ring of intensity with a 2π phase singularity along the beam axis. Chapter 3 contains examples of LG_p^l modes of various l and

p values.

In the early 90s, experimenters began to explore the use of diffractive optical components to transform spatially coherent, planar-waved beams into beams containing optical vortices. In 1990 Soskin and co-workers recognized that if a diffraction grating was modified to include an edge dislocation at its centre, then the first order diffracted beam contained an optical singularity [BVS90]. This classic “forked” hologram design is now virtually synonymous with the generation of optical vortices. The forked design can be implemented either as an amplitude or phase grating, both of which can be calculated as the modulus 2π addition of a helical phase $\exp(i\ell\phi)$ with a diffraction grating. In parallel with the work of Soskin and colleagues, Heckenberg and co-workers used a variation design where the azimuthal phase term was added to a Fresnel lens such that the various diffraction orders were separated axially [HMS⁺92].

In 1993, Woerdman and co-workers pursued a new approach to the generation of vortex carrying beams. They built optical components termed “spiral phase plates”. These are discs of optical refractive index n with optical thickness (Δt) that increases with azimuthal angle, i.e. $\Delta t = \frac{\phi}{2\pi}(n-1)\ell\lambda$. Upon transmission, an incident plane wave will acquire an $\exp(i\ell\phi)$ phase term and consequently have an optical vortex along the beam axis. The motivation behind this work was to produce a vortex beam, with its associated orbital angular momentum, that was free from astigmatism. However, these spiral phase plates require precise matching of the $(n-1)\ell\lambda$ step height at the centre, which places extremely high demands on the engineering tolerance — particularly for optical wavelengths. At radio or millimeter-wave frequencies these tolerances are not so extreme [TRS⁺96]. In the original work, the plate was immersed in a temperature-controlled fluid bath. Changing the temperature of the bath ingeniously controlled the refractive index mismatch and hence allowed the step height to be tuned to exactly the correct value. Since then, a number of groups have employed precise micro-machining techniques to make spiral phase plates directly [WFW⁺04, TSM07].

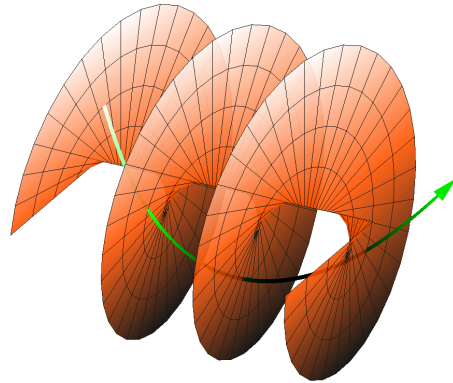


Figure 1.5: A diagram showing a surface of constant phase around an optical vortex with the Poynting vector indicated by a green line.

Despite the various methods which have been developed for generating vortex carrying beams ranging from cylindrical lenses, specially modified lasers and spiral phase plates, none match the ease and flexibility of computer generated holograms. The popularity of diffractive optical components for generating specific beams has been massively enhanced by the commercial availability of spatial light modulators (SLMs). These devices contain an array of pixels which can be addressed via a computer with an image that defines the spatial variation of the phase or intensity of the reflected light. Figure 1.4 shows how using a spiral phase plate and a diffractive optical element can result in similar beams containing vortices.

The majority of experiments whose results are presented throughout the following chapters were conducted using SLMs. The use of these devices will be discussed in chapter 3.

1.3 Optical angular momentum

One reason for there being so much interest in optical vortices is their link to optical angular momentum. A vortex line (in any plane other than the transverse plane) gives rise to helical phasefronts (see Fig. 1.5). The recogni-

tion in 1992 by Allen et al. [ABSW92] that a helically-phased beam carries orbital angular momentum has since linked the two fields of vortices and optical angular momentum. This orbital angular momentum arises from the azimuthal phase structure of the optical beam and hence it can be independent of the spin angular momentum, which is linked to the polarisation state. The link between singularities and angular momentum extends further once it is recognised that polarisation singularities are lines of circular polarisation and hence associated with the spin angular momentum of the field.

It is worth clarifying the relationship between optical vortices and orbital angular momentum, two terms that are often (incorrectly) used interchangeably. As detailed in chapter 2, an optical vortex is a position in space around which the optical phase advances or retards by a multiple of 2π . However, the intensity at the vortex centre is zero and therefore the vortex itself carries no linear, nor angular, momentum. By contrast, it is in the immediate vicinity of the vortex that the azimuthal phase term means that the phase-fronts of the optical field are helical. The associated Poynting vector has an azimuthal component and hence there is a net flow of both energy and momentum around the vortex line, which in turn gives an angular momentum directed along the line. An optical beam can have an azimuthal phase gradient without a nearby phase singularity meaning that light can still possess an orbital angular momentum without an optical vortex [CDAP97].

Despite this distinction, it is the case that the vast majority of studies involving orbital angular momentum have utilized beams containing optical vortices aligned along the beam axis. For an intensity-symmetric light beam with a helical phase structure described by $\exp(i\ell\phi)$, where ℓ is any integer value, the orbital angular momentum is equivalent to $\ell\hbar$ per photon.

1.4 Thesis format

Singular optics is a topic currently of great interest to researchers both theoretically and experimentally. This thesis makes original contributions to both areas but with an emphasis on numerical and laboratory experiment. The theoretical contributions are modest and rely on simple arguments but do contain significant results. The following paragraphs briefly describe the structure of the thesis.

Chapter 2 covers the basic properties of optical singularities, both scalar and vector. This chapter is entirely didactic and contains no original material.

Chapter 3 gives a full description of experimental methods and apparatus. During its course it will also cover some theory needed to understand the demonstration/calibration runs. A full 3D complex optical data-acquisition system and polarisation camera are the main features of this chapter.

Chapter 4 leads on from the basic properties of optical singularities and gives examples of optical vortex lines in three dimensions. The main purpose of this chapter is to phrase the language of singularities firmly in three dimensions and illustrate their three-dimensional properties and as such does not contain any original research. This chapter also contains a modern experimental approach to the elliptic umbilic diffraction catastrophe.

Chapter 5 describes how plane-wave interference affects vortex structure and topology. This chapter contains original insight into how fields are affected by complex amplitudes and gives inequalities that determine vortex topology in four-wave interference.

Chapters 6 and 7 establish a model for simulating Gaussian random fields and study empirically the topology and structure of vortex lines in these fields. It also includes newly developed methods for automating knot and link finding for arbitrary curves. This was the most significant body of work and is entirely the work of myself with guidance and assistance from Prof. Miles J. Padgett and Dr Mark R. Dennis.

Chapter 8 gives the first experimental results of compact knotted and linked vortex lines in Gaussian beams. This work was made possible by the original work and insight of Mark Dennis who provided me with Laguerre-Gauss decompositions for creating the beams reported here. There are three different types of vortex structures realised: the Hopf link, the trefoil knot and the cinquefoil knot. The experimental results and mode optimisations are the contributions of the author.

Chapter 9 considers polarisation singularities and is concerned with experiments conducted by Dr Florian Flossmann (who made the most significant contributions). Working alongside him on this experiment I have included the results here to complement the work on scalar phase singularities. Results are given for laboratory measurements of polarisation singularity type ratios and densities predicted in Ref. [Den02].

Chapter 10 summarises and concludes the thesis.

The notation used in the following chapters follows common literature, such as bold letters denoting vectors (notation will be clarified when necessary).

CHAPTER 2

Theory

“We expect to find a hole in the theory here ... a naked singularity would be very messy. The mathematics is inconsistent - like dividing zero by zero.”

— Larry Niven, *Singularities Make Me Nervous*, in
Convergent Series, 1980

In this chapter the basic properties of optical singularities will be covered. The majority of the chapter will deal with optical vortices in complex scalar fields followed by a brief overview of polarisation singularities in vector fields. Not every element of theory that appears in this thesis will be explained here, some will be covered when relevant during a chapter.

2.1 Phase singularities in scalar fields

2.1.1 Basic properties

An optical vortex is a point of zero intensity in an optical field at which the phase is undefined [NB74]. It is a phase singularity in the complex scalar

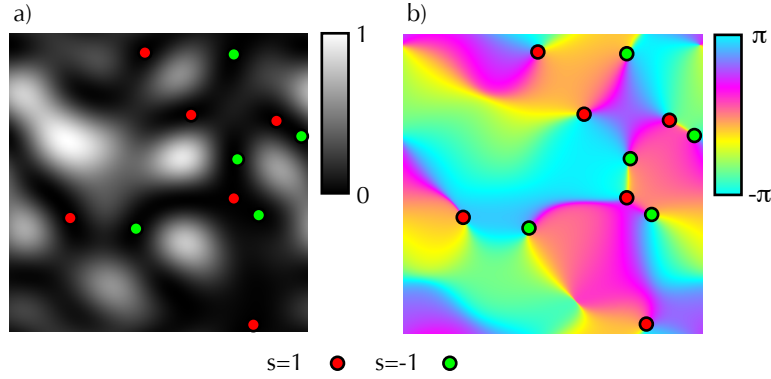


Figure 2.1: Cross-section of a field consisting of 25 plane waves showing (a) normalised intensity of field and (b) phase of field with colour representing phase. Vortices are marked here with their topological charge, $s = \pm 1$, indicated by the red and green spots.

representation of light fields. Around such a point all phase values converge (illustrated in Fig. 2.1). This type of phase structure results in a Poynting vector that rotates around the point of zero intensity [AP00], hence the term vortex.

Taking ψ to denote the complex scalar representation of an optical field. A vortex in ψ , satisfies the following condition:

$$\psi = \rho e^{i\phi} = \xi + i\eta = 0, \quad (2.1)$$

where ρ , ϕ , ξ and η are the amplitude, phase, real part and imaginary part of the field. Assuming that ψ is monochromatic (which will be the case for all following chapters), the vortex lines are exactly the zeros of the Helmholtz equation:

$$\nabla^2 \psi^2 + k^2 \psi = 0. \quad (2.2)$$

The current density in such a field is:

$$\mathbf{j} = \text{Im } \psi^* \nabla \psi = \rho^2 \nabla \phi = \xi \nabla \eta - \eta \nabla \xi, \quad (2.3)$$

and the current vorticity is:

$$\boldsymbol{\omega} = \frac{1}{2} \nabla \times \mathbf{j} = \nabla \xi \times \nabla \eta. \quad (2.4)$$

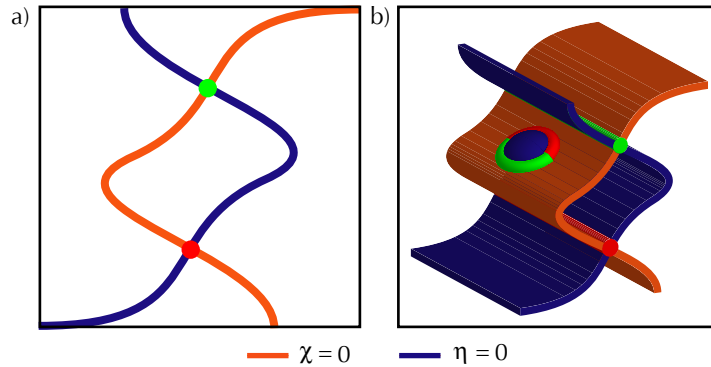


Figure 2.2: Illustration of how the dimension of the vortex arises from the field contours. In 2D the $\xi = 0$ (blue) and $\eta = 0$ (orange) contours are lines and therefore intersect at points ($s = -1$ and $s = 1$ indicated in red and green respectively). In 3D the contours are surfaces, intersecting along lines. The intersections shown here illustrate how loops may arise.

Integrating the phase along a non self-intersecting closed path, C , around a vortex results in a multiple of 2π ,

$$\oint_C d\phi = s2\pi. \quad (2.5)$$

This integer, s , is called the topological charge of a vortex. As s is generically ± 1 , it is usually taken to be the sign of the current vorticity of the field projected onto the z -axis,

$$s = \text{sign } \boldsymbol{\omega} \cdot \hat{z}, \quad (2.6)$$

however any choice of projection may be made.

The vortices exist where ϕ is singular, which can only be true if both ξ and η are zero. In terms of phase, the $\xi = 0$ contours correspond to joining the $\phi = \pi/2$ and $\phi = -\pi/2$ contours. The $\eta = 0$ contours correspond to joining the $\phi = 0$ and $\phi = \pi$ contours. Put simply, the crossing of these zero contours indicates the convergence of the phase values $\phi = -\pi/2, 0, \pi/2, \pi$, which only happens at a vortex.

These contours help visualise how vortex lines appear in different dimensions as vortices are exactly the intersections of the real and imaginary zero

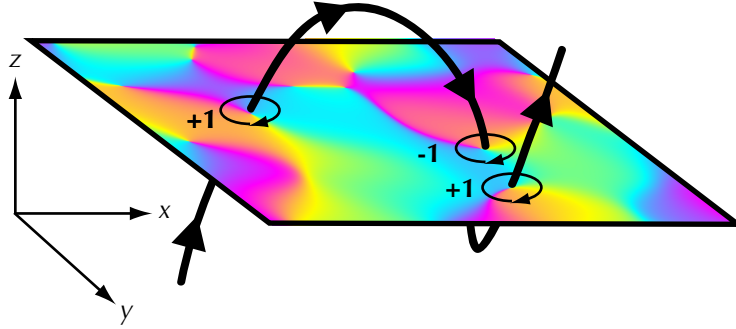


Figure 2.3: Illustration of how the sign of the topological charge of vortices arises from the underlying 3D structure of the vortex line. As the line ‘pierces’ the plane the sign of the topological charge alternates with each pass as a result of the topological current (indicated by arrowheads along the vortex line) remaining in a fixed sense. The small black circles indicate the direction of the line integral used to evaluate the charge.

contours. The imagery of two surfaces intersecting is very helpful in understanding the geometry and topology of vortex lines. For instance, if a peak of one surface just passes through the other, the perimeter of this ‘island’ would be a vortex loop. This can be seen in Fig. 2.2.

Put more formally, phase singularities are said to have a codimension of two as they depend on two separate conditions ($\xi = 0$ and $\eta = 0$). The dimensional extent of the singularity is then the dimension of the space they are embedded in minus their codimension. In a plane vortices are points and in a volume they are lines. In a time dependent field, with time constituting a fourth dimension, the vortices are surfaces (this can be imagined as the vortex lines in a volume sweeping out surfaces in time).

The topological charge is a 2-dimensional property of a vortex as it is evaluated over a closed line integral on a surface. The sign s in 2D is arbitrary and depends on the projection being considered ($s = 1$ viewed from $+z$ appears as $s = -1$ from $-z$). However, the charge with respect to the direction of ω is conserved along the entire length of the line. Due to this conservation it is useful to associate the direction of ω with a topological current. Figures 2.2 and 2.3 illustrate the role of the sign of the topological charge of

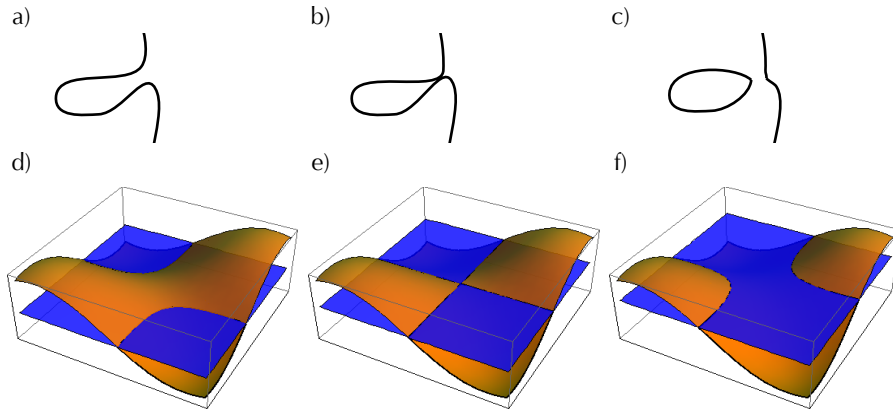


Figure 2.4: Illustration of reconnection changing topology of a vortex line. a) shows the vortex line before, (b) shows line at, and (c) shows the line after reconnection. Parts (d, e, f) show the zero contour surfaces of the real and imaginary parts of the field near the reconnection location with the reconnection occurring at (e).

vortex lines in 3D.

2.1.2 Reconnections

Reconnections are the process through which vortex lines can change topology. At a reconnection, vortex lines are degenerate in the sense that two possible line paths exist. Figure 2.4 illustrates a reconnection taking place resulting in a change of topology, also shown are the zero contours of the real and imaginary parts. Exactly at a reconnection the following condition is met:

$$\boldsymbol{\omega} = \nabla\xi \times \nabla\eta = 0. \quad (2.7)$$

So when the gradient of zero contours of χ and η are parallel, two vortex lines cross perfectly. Reconnections have codimension 4 as they are dependent on phase singularities occurring where $\boldsymbol{\omega} = 0$ and as $\boldsymbol{\omega}$ is a vector field, its zeros also have codimension 2. Due to the dependency on two codimension 2 events, reconnections have codimension 4. The result of this is that

reconnections are points in time dependent fields. A reconnection point can be seen in Fig. 2.4 part (e).

In monochromatic fields, reconnections almost surely never happen (their codimension being too high), but it is through these reconnections, as an external parameter (providing an extra dimension) is changed, that vortex lines change topology. This idea will be explored further in chapter 4.

2.1.3 Vortex point densities

One aspect of optical vortices which is very well understood is the statistics of point singularities in a plane [BD00]. With the condition that the plane-wave components of the field have Gaussian random real and imaginary parts the transverse and axial vortex densities, D_{xy} and D_z , are [Ber78]:

$$D_{xy} = \frac{K_2}{4\pi} \quad (2.8)$$

$$D_z = \frac{K_2^{\frac{3}{2}}}{4\sqrt{2\pi}k} \quad (2.9)$$

where K_2 is the second moment of the power-spectrum of the field. For a Gaussian spectrum the second moment is $K_2 = 2K_\sigma^2$. Putting this into Eqn.s 2.8 and 2.9, the densities become:

$$D_{xy} = 2\pi/\Lambda_{xy}^2 \quad (2.10)$$

$$D_{xz} = D_{yz} = 2\pi/(\Lambda_z\Lambda_{xy}), \quad (2.11)$$

where

$$\Lambda_{xy} = \lambda \left(\frac{k_0}{K_\sigma} \right) \text{ and } \Lambda_z = \lambda \left(\frac{k_0}{K_\sigma} \right)^2 \quad (2.12)$$

are the natural length scales in the xy and z axes ($\lambda = 2\pi/k$ as usual). These units allow any calculations to be scaled such that the vortex point densities are isotropic and as such both lengthscales, Λ_{xy} and Λ_z , can be referred to simply as Λ .

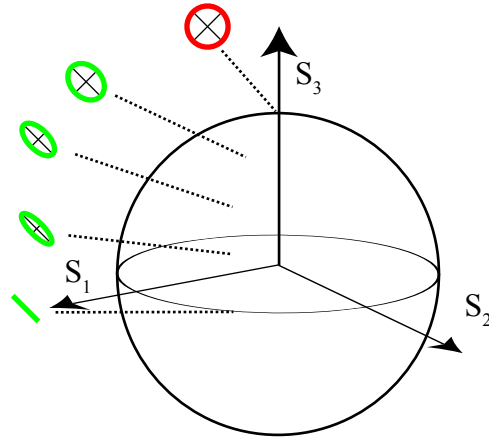


Figure 2.5: The Poincaré sphere representing all possible polarisation states. Four example polarisation ellipses are drawn on the $S_1 = S_2$ great circle, giving an ellipse major axis angle of $\pi/2$. A circularly polarised state is highlighted in red; this state is a polarisation singularity.

2.2 Polarisation singularities

A field describing polarisation is a complex vector field — each point can be written as (E_x, E_y, E_z) with E_i taking complex scalar values. For the case of transverse polarisation states let $E_z = 0$. As the phase of such a field is varied, the real part of the vector traces out an ellipse — the polarisation ellipse. All possibilities of polarisation ellipse exist on the Poincaré sphere with cartesian coordinates (S_1, S_2, S_3) , see Fig. 2.5 for a diagram of this sphere and example polarisation states on it. The poles of this sphere are polarisation singularities, where the ellipse becomes a circle.

Polarisation singularities have similar properties to phase singularities. However, due to the π rotational symmetry of the headless vector describing polarisation state there is considerably more variety. The topological index of a polarisation singularity is $s_p = \pm 1/2$ due to the π symmetry. Although there are two topological indices there are three different types of polarisation singularities: star, lemon and monstar.

The differences between the singularities can be seen easily in Fig. 2.6. Stars

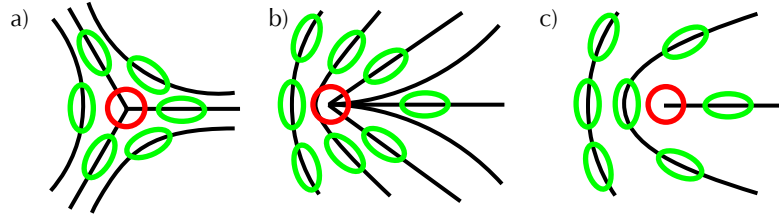


Figure 2.6: Classification of polarisation singularities a) Star ($s_p = -1$), b) Monstar ($s_p = +1$) and c) Lemon ($s_p = +1$).

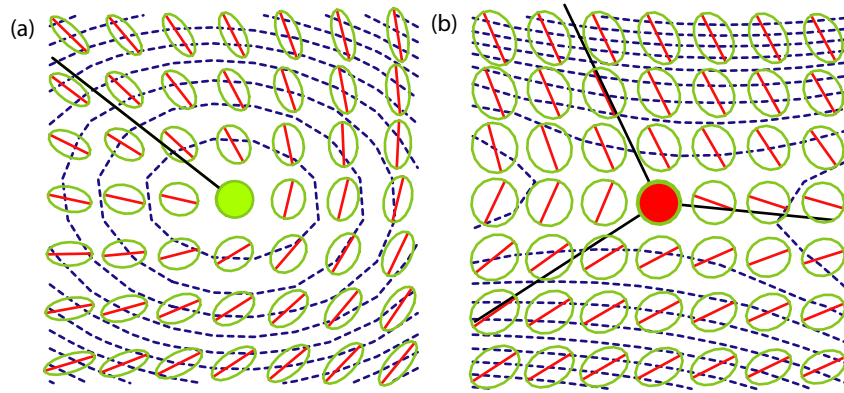


Figure 2.7: Elliptic and hyperbolic configurations of polarisation singularity.

have $s_p = -1/2$ whilst lemons and monstars have $s_p = +1/2$ corresponding to anti-clockwise ($-1/2$) and clockwise rotation ($+1/2$) of the polarisation ellipse major axis around the singularity. Each of these types of singularity can also be left or right circularly polarised (opposite poles on the Poincaré sphere). This would result in 6 different types of singularity — but there are more!

Polarisation singularities can also be classified into elliptic or hyperbolic types. The distinction can be seen visually in the contours of the polarisation ellipse major axis lengths seen in Fig. 2.7.

Between singularities of opposite handedness there must be points of complete linear polarisation (where the ellipse has become flat). This state corre-

sponds to the equator on the Poincare sphere and must be traversed to smoothly move from a right circularly polarised singularity to left.

In 2 dimensions (transverse polarisation) the combination of singularity index with left and right handedness results in a picture of points in the plane which are singular, of both left and right circular polarisation, with lines, called L-lines, of linear polarisation separating them. Extended into a volume of transverse polarisation states, the C-points become lines and the L-lines become L-surfaces separating volumes of left and right handed polarisation states.

The decomposition of polarisation fields into left and right circular polarisation is key in understanding how the statistics of singularities in scalar fields are inherited by vector fields. As the left or right circular components can be described by complex scalar fields, they themselves have phase singularities of the type described earlier in this chapter. The orthogonal addition of the left-handed and right-handed fields result in the network of zeros in each component being ‘filled’ by circularly polarised light of the opposite handedness. The network of scalar singularities becomes a network of C-lines. The density of C-points/lines is simply double that of phase singularities. However, this says nothing of the features in polarisation fields which occur due to the π symmetry of the polarisation vector.

This concludes the theoretical description of optical singularities required for the content of the thesis.

Experimental apparatus

This chapter will detail the experimental apparatus used to obtain results in following chapters. Also included will be detailed descriptions of methods used to analyse data. A full 3D complex optical data-acquisition system and polarisation camera are the main features of this chapter. Example calibration results will be given, demonstrating the scope of the apparatus.

3.1 General apparatus

The experiments required to study optical singularities in monochromatic beams are of a very general type. They involve measuring basic properties of light: intensity, phase and polarisation state. The first is the most straightforward to measure. Placing a CCD array in the observation plane allows the intensity to be measured to within the dynamic range of the device used. The phase of a linearly polarised beam can be measured by using interferometric techniques. The polarisation can be obtained by measuring different linear components and calculating Stoke's parameters.

A generic setup for shaping a beam and measuring the intensity is shown in Fig. 3.1. Here a source (a He-Ne laser with $\lambda = 632\text{nm}$) is expanded using a

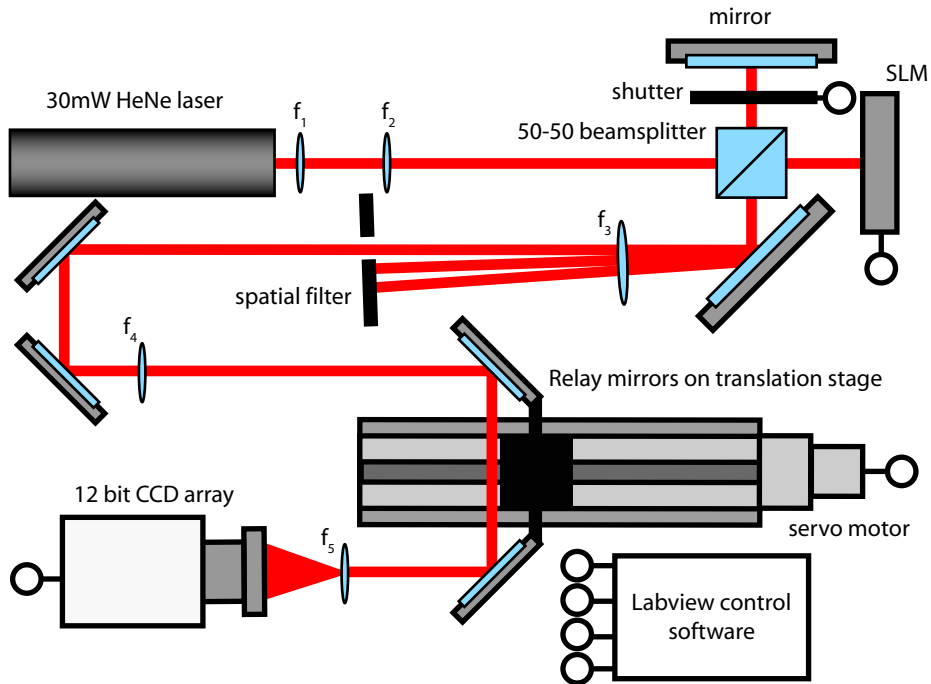


Figure 3.1: Experimental setup for intensity and phase acquisition.

telescope with lenses of focal length f_1 and f_2 . The expanded beam is then incident on a Spatial Light Modulator (SLM) controlled by a PC with custom written LabVIEW software (the use of an SLM will be discussed later). The reflected light is then filtered in the Fourier plane through use of a lens, f_3 , and a spatial filter (essentially a pinhole) positioned in the focal plane of this lens. A fourth lens, f_4 , can be used to image the plane of the SLM onto a CCD array via a fifth lens, f_5 , which magnifies the image. A translation stage, controlled again by LabVIEW software, mounted with relay mirrors is placed between lenses f_4 and f_5 . This allows the path difference between the final two lenses to be increased by adjusting the translation stage. This changes the plane being imaged onto the CCD, allowing a full 3D scan of the beam. The camera can be scanned either through the SLM plane or the Fourier plane. To this end, the apparatus depends somewhat on how the SLM is being used.

3.2 Spatial Light Modulator

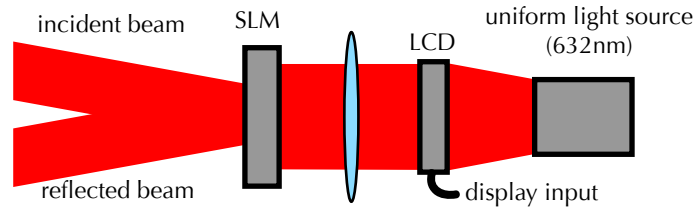


Figure 3.2: How an optically addressed SLM operates. Graphical input is received from a PC and displayed on the LCD. The transmitted light is then imaged onto the SLM. Light incident on the SLM now undergoes an optical delay proportional to the light intensity imaged onto the SLM.

An SLM is a device which can manipulate the wavefront of incident light. Most achieve this by using a nematic liquid crystal polymer which causes an optical delay dependent upon the electric field across a depth of liquid crystal. The device used in the following experiments was an optically addressed Hamamatsu SLM. This SLM has a resolution of 1024×768 with each pixel capable of $0 - 2\pi$ phase modulation across 256 levels (8-bit device). The SLM is treated as a second monitor on the controlling PC. Data to be written to the SLM is simply displayed as grayscale on a second monitor output from the appropriate graphics card.

The SLM operates by first displaying the phase values as a grayscale image on a basic LCD. This LCD is illuminated by a uniform light source of wavelength 632nm (coherence is not important). The transmitted light is imaged onto one side of the SLM. The light incident on the SLM causes an electric gradient across the liquid crystal. It is this gradient that is responsible for the optical delay on reflected light incident on the opposite surface. The brightest areas cause a 2π delay and the darkest cause none. A basic schematic is shown in Fig. 3.2.

The reflected light now has the desired phase modulation. However, there is still a strong surface reflection from the SLM which is unchanged. In order for the modulation to be of any use, this zero-order reflection must be

separated from the desired beam. The zero-order reflection can be removed, but at a cost of efficiency. How this is achieved will be described in the following section on Computer Generated Holograms (CHGs).

3.3 Computer Generated Holograms

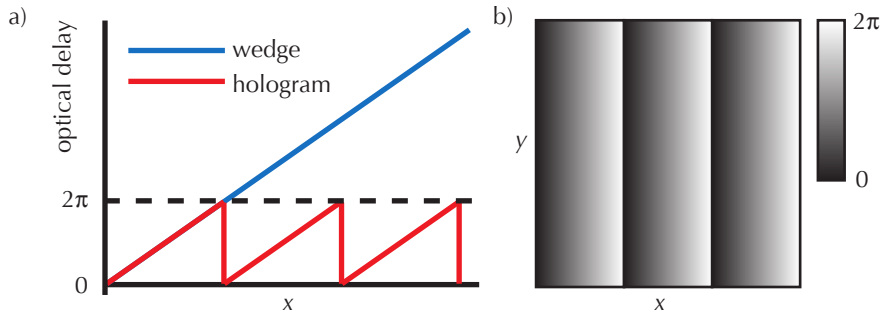


Figure 3.3: How the optical delay of a wedge is represented as a hologram. a) 1D slice showing how the optical delay of a wedge increases and how the hologram is calculated. b) 2D hologram of a wedge of dielectric (also called a blazed grating).

Holograms are planar devices that modulate light. Holograms are engineered to have a particular transmissive function, $T(\mathbf{r})$, desired for an experiment. Traditionally, holograms were recorded using interferometry on very high resolution photographic film (this is still how holograms for entertainment are made). As computing power became readily available the form of a hologram could be calculated, rather than recorded, and then printed directly to photographic film. The combination of a desktop PC and an SLM allows the ad-hoc calculation and display of holograms. In order to use Computer Generated Holograms (CGHs) effectively in experiments, the optical modulation desired must be understood well.

The way in which simple objects interact with light can be represented by a complex transmissive function, $T(\mathbf{r})$ (reflective objects can be treated in the same way). The effect of this function is to modulate incident light. Basic geometric apertures (such as an iris) are the most simple forms of this

function, being binary operators (an iris of radius R would have $T(\mathbf{r} \leq R) = 1, 0$ otherwise). Transparent dielectrics are represented with unit amplitude and phase (optical delay) proportional to the width of the material. Prisms increase in optical delay linearly and thin lenses parabolically. A hologram of a thin prism is shown in Fig. 3.3

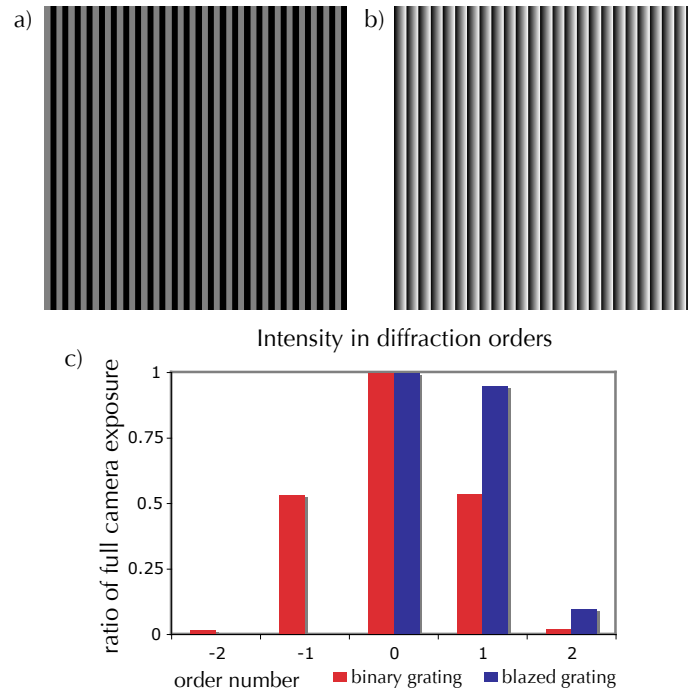


Figure 3.4: Grayscale images (a) and (b) show holograms of a binary phase grating and a blazed phase grating respectively. Intensity measurements of diffraction orders $-2, -1, 0, 1, 2$ are shown in (c). The zeroth order is overexposed in both sets of measurements (a value of 1 is assigned to 4095, the maximum output of the 12-bit camera used)

The shaping of the wavefront is not limited to optical components. Arbitrary phase profiles that may be difficult (or impossible) to engineer with ordinary optics are possible. In particular, superpositions of more exotic base modes (such as Laguerre-Gauss and Bessel modes) are now possible to generate. However, to shape light beams in this way, both the intensity and phase must be modulated. This can be achieved using a phase only SLM.

The first step to achieve the desired modulation of a beam is to add an

additional modulation which is in effect a phase diffraction grating. The effect of this is very apparent in the Fourier plane of the reflected beam. The addition of the desired phase with a diffraction grating results in a series of diffraction orders, each of which has the the desired phase (or conjugate). A single order may now be allowed to pass through a pin-hole and the others blocked. The modulated beam has now been removed from the reflected zero order. However, a grating distributes the power in the beam amongst orders either side of the central peak equally. This results in a relatively low efficiency.

To overcome this, the phase grating can be replaced with the hologram of a wedge, directing more power into the first order peak. There are still diffraction orders as the transmissive function of the hologram is not perfectly smooth, there exist real finite jumps between the values of $\phi = 0$ and $\phi = 2\pi$. These abrupt periodic changes cause the diffraction orders to remain, but now with a lower ratio of the total power. The effect of switching a binary phase grating with a wedge can be seen in Fig. 3.4. This technique is known as blazing.

If the SLM is now re-imaged, it will only contain the Fourier components that have passed through the filter in the Fourier plane (see apparatus in Fig. 3.1). The beam will now have the desired phase profile, but the intensity remains, mostly, unchanged.

To modulate the intensity appropriately, a factor is applied at each pixel mapping the range $[-\pi, \pi]$ to $\text{sinc}^2(\pi - I(\mathbf{r})\pi)[-\pi, \pi]$, where $I(\mathbf{r})$ is the normalised desired intensity. The multiplicative factor used here is determined from the diffractive efficiency of the SLM. In order to be effective this step must be carried out after adding a blazed diffraction grating to the desired phase profile. Essentially, the higher the contrast in the blazed grating's peaks and troughs, the more light is diffracted into the first order. The full calculation for the phase values to be displayed on the SLM is

$$\phi(\mathbf{r})_h = [((\phi(\mathbf{r})_d + \phi(\mathbf{r}, \Lambda)_b)_{\text{mod } 2\pi} - \pi)] \text{sinc}^2(\pi - I(\mathbf{r})\pi) + \pi. \quad (3.1)$$

Here, $\phi(\mathbf{r})_h$ is the phase pattern of the hologram, $\phi(\mathbf{r})_d$ is the phase of the

desired beam and $\phi(\mathbf{r}, \Lambda)_b$ is the phase of a blazed diffraction grating of period Λ . The constants in the equation simply shift the phase ranges from $[-\pi, \pi]$ to $[0, 2\pi]$. Figures 3.5 and 3.6 show intensity measurements for two different types of beam in the re-imaged plane of the SLM after filtering in the Fourier plane, both figures show results with and without the intensity modulation.

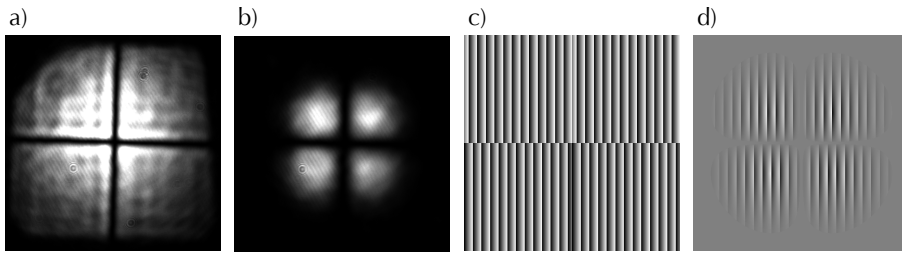


Figure 3.5: Intensity measurements in the SLM image plane of attempted beam shaping of HG_{11} after Fourier filtering, without (a) and with (b) intensity modulation. The holograms displayed on the SLM to generate beams (a) and (b) are shown in (c) and (d), grayscale represents $\phi_h = [0, 2\pi]$.

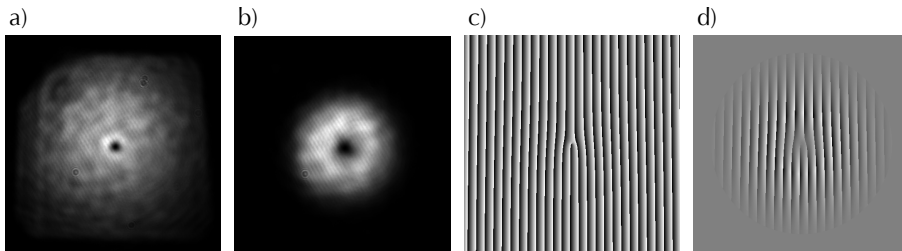


Figure 3.6: intensity measurements in the SLM image plane of attempted beam shaping of LG_1^0 after Fourier filtering, without (a) and with (b) intensity modulation. The holograms displayed on the SLM to generate beams (a) and (b) are shown in (c) and (d), grayscale represents $\phi_h = [0, 2\pi]$.

This method is very successful in shaping a beam into the correct intensity and phase profile.

3.4 Phase measurements

Phase can be measured by use of the reference beam which is diverted before the SLM and injected after the SLM modifies the object beam (see Fig. 3.1). The mirror that reflects the reference beam is angled so that the beam copropagates with the first-order diffracted beam from the SLM, allowing it to pass through the filter in the Fourier plane. The shutter allows the reference beam to be blocked, allowing simple intensity measurements to be taken.

Simply interfering the shaped beam with the reference beam does not easily allow phase measurements to be made. The relative phase between the beams must be shifted so that an intensity modulation at each pixel can be observed. Figure 3.7 illustrates this method. Figure 3.7(a) shows the intensity of the object beam, B_o , and Fig. 3.7(c) shows the resulting intensities, U , after introducing a reference beam, B_r with phase ϕ_r . Part (b) plots the intensity of the four pixels highlighted in part (a) as a function of reference beam phase, ϕ_r . The relative phase between B_o and B_r can be measured by taking N images of the resulting intensity, U_n with the reference beam having its phase shifted by $\phi_r = 2\pi n/N$.

$$U_n(\mathbf{r}) = \text{mod}[B_o(\mathbf{r}) + e^{i\frac{2\pi n}{N}} B_r(\mathbf{r})]^2 \quad (3.2)$$

The intensity measurements for each pixel form a discrete, equally spaced, set of interference measurements spanning $\phi_r = [0 - 2\pi]$. The argument of the first non-d.c. component of the Fourier transform of this set yields the relative phase between B_o and B_r .

$$\Phi(\mathbf{r}) = \arg \sum_{n=0}^N U_n(\mathbf{r}) e^{-i\frac{2\pi n}{N}} \quad (3.3)$$

Shannon's sampling theorem tells us that the minimum number of measurements required to retrieve the desired phase information is $N = 3$ (with $\phi_r = 0, 2\pi/3, 4\pi/3$). Typically in experiments performed in this thesis $N = 4, 8, 16$ depending on constraints of image acquisition and processing time. The greater N , the more accurate $\Phi(\mathbf{r})$ is. However, as it is the

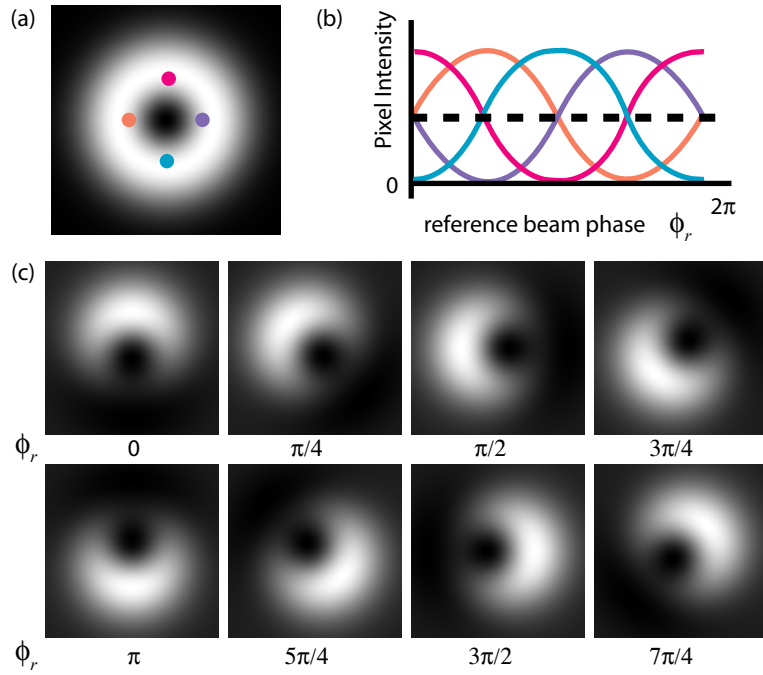


Figure 3.7: Illustration of how the phase of a beam cross-section is measured experimentally. (a) shows the intensity of an object beam, (b) shows the intensity modulation of pixels at the coloured spots in (a) as a co-propagating reference beam is introduced and phase shifted. (c) shows different intensity patterns created by the modulation of the reference beam phase, ϕ_r

singular points of the phase that are of interest, the exact form of the phase retrieved is not so important and $N = 4$ is sufficient for determining the positions of the singularities within a few pixels.

3.5 Vortex finding

Finding positions of singularities in a phase map is not difficult. It is the non-zero charge of a vortex that makes them easy to find. Any closed path integral around a vortex yields a non-zero result (see Eqn. 2.5). Figure 3.8 illustrates this method on simulated data. Each 2D section of phase can be searched pixel by pixel looking for vortices. However, if only the xy cross-

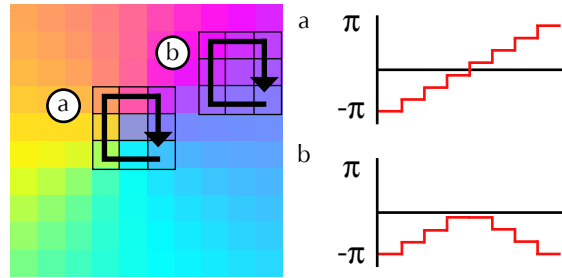


Figure 3.8: Two example integration paths on computed phase values. Path (a) encloses a vortex which can be identified by the overall change in phase as the path returns to its starting point. Path (b) does not enclose a vortex and the phase can be seen to return to its original value with no discontinuity.

sections of the 3D phase data were searched, the points found would form lines with sections missing. These missing sections are the line segments that are parallel to the xy plane. This is overcome by performing several integrations. The method outlined above for finding vortices is not restricted to any particular plane, meaning that the xy , yz and zx planes can all be searched. The result is a fully connected vortex pattern in 3D with topological charge information for each point. By performing these three closed integrals in three orthogonal planes the resulting topological charge is a vector, $\mathbf{s} = (s_{xy}, s_{yz}, s_{zx})$, that can take on 27 possible forms (due to each component being either 1, -1 or 0.) After every vortex location has been located assigned a charge, they need to be connected into individual vortex lines. This step will be described in chapter 6.

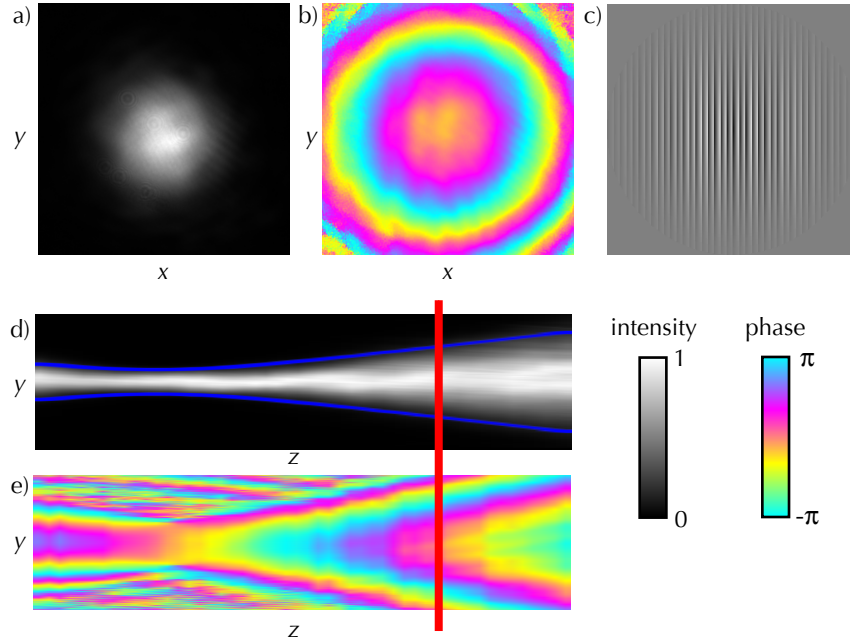


Figure 3.9: Transverse cross-sections (a,b) of the intensity and phase in the re-imaged plane of the SLM generated by the hologram shown in (c). Longitudinal cross-sections are also shown (d,e) at $x = 0$, with a red line showing the position of the cross-sections (a) and (b). The blue line in (d) marks $r = w(z)$ with $w_0 = 85\mu\text{m}$ and $z_r = 35.9\text{mm}$. The scan range shown is 189.2mm covering $-1.2z_r$ to $4z_r$.

3.6 Apparatus test and examples

3.6.1 Propagation of a Gaussian spot

A focussed Gaussian spot propagates without transversal intensity changes — it is said to be stable on propagation. The transverse pattern scales as

$$w(z) = w_0 \sqrt{1 + \left(\frac{z}{z_r}\right)^2}, \quad \text{where } z_r = \frac{\pi w_0^2}{\lambda}. \quad (3.4)$$

Here $w(z)$ is the beam waist size at axial position z , w_0 is the beam waist at $z = 0$, and z_r is the Rayleigh range of the beam (where $w(z_r) = \sqrt{2}w_0$). Figure 3.9 shows an intensity scan of a Gaussian beam, alongside the hologram used to create the focussed spot. This is a very basic test of the intensity

capture process and illustrates the scanning range of the apparatus. The beam waist size, w_0 , was known roughly but was measured accurately by first measuring the distance by which $w(z)$ of the transverse Gaussian profile doubled from its minimum value, giving z_r , and using Eqn. 3.4 to calculate w_0 . A full scan range of approximately $5z_r$ was deemed large enough for most applications (the full extent of the translation stage allows $7z_r$ with this setup).

3.6.2 Laguerre-Gauss beams

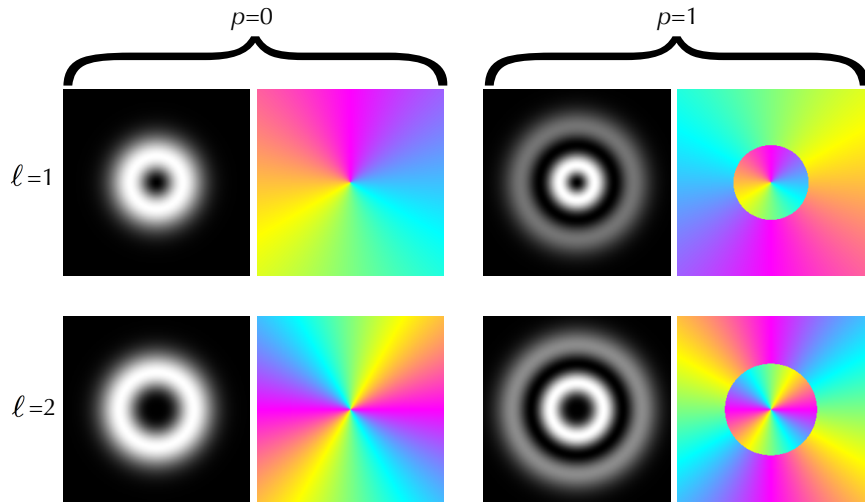


Figure 3.10: intensity and phase of Laguerre-Gauss modes LG_1^0 , LG_1^1 , LG_2^0 and LG_2^1 . The colour scales are as usual. The effects of the indices on phase and intensity structure are very clear — ℓ is responsible for the azimuthal variation in phase giving the distinctive ‘colour’ wheel appearance and p causes radial phase discontinuities of π .

A Laguerre-Gauss beam in cylindrical coordinates (R, θ, z) has the normalised form

$$\begin{aligned} \text{LG}_p^\ell(R, \theta, z; w) &= \sqrt{\frac{p!}{\pi(|\ell| + p)!}} \frac{R^{|\ell|} \exp(i\ell\theta)}{(w^2 + iz/k)^{|\ell|+1}} \exp\left(\frac{-R^2}{2(w^2 + iz/k)}\right) \\ &\times L_p^{|\ell|}\left(\frac{R^2}{w^2 + z^2/k^2 w^2}\right) \left(\frac{w^2 - iz/k}{w^2 + iz/k}\right)^p \end{aligned} \quad (3.5)$$

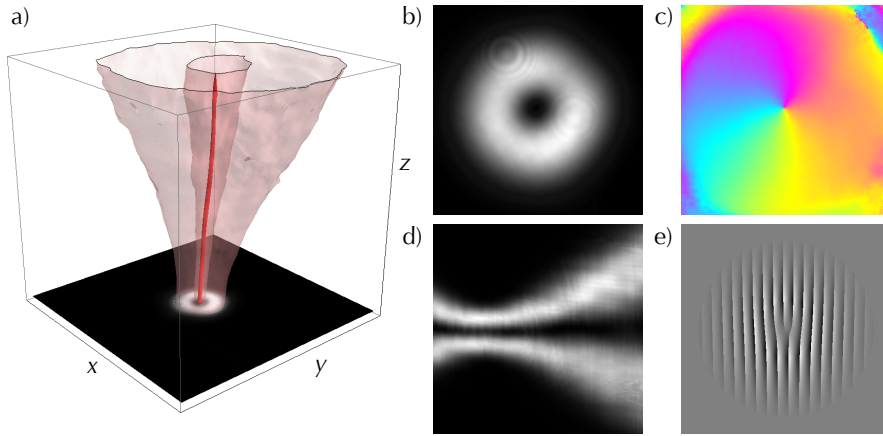


Figure 3.11: Laguerre-Gauss beam with $\ell = 1$. a) Contours shows half the maximum intensity, optical vortex as a red line. b) intensity at the beam waist ($z=0$) and (c) measured phase at $z = 0$.

where k is the the wavenumber and w is the beam waist as described for the Gaussian beam. The two indices ℓ and p are integral to the nodal structure of these beams. An on-axis optical vortex of charge $s = \ell$ is present due to the phase term $e^{i\ell\theta}$ and p is the number of concentric ring nodes that envelope the centre. To illustrate this some modes are plotted in Fig. 3.10.

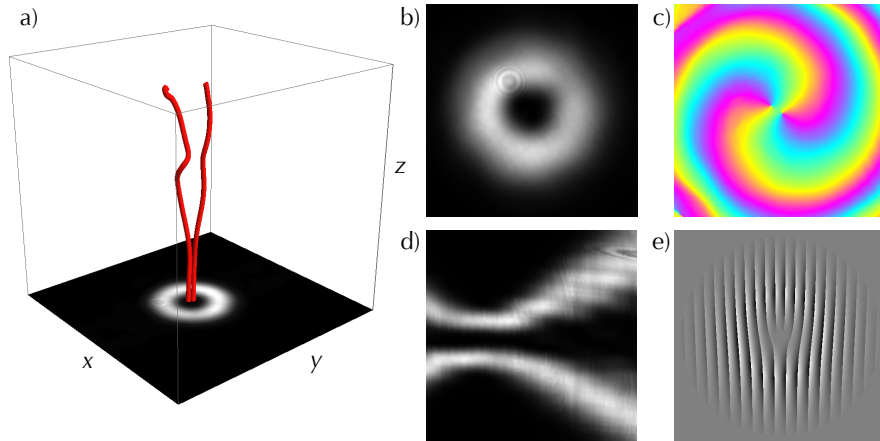


Figure 3.12: Laguerre-Gauss beam with $\ell = 2$. a) Contours shows half the maximum intensity, optical vortex as a red tube. b) intensity at the beam waist ($z=0$) and (c) measured phase at $z = 0$.

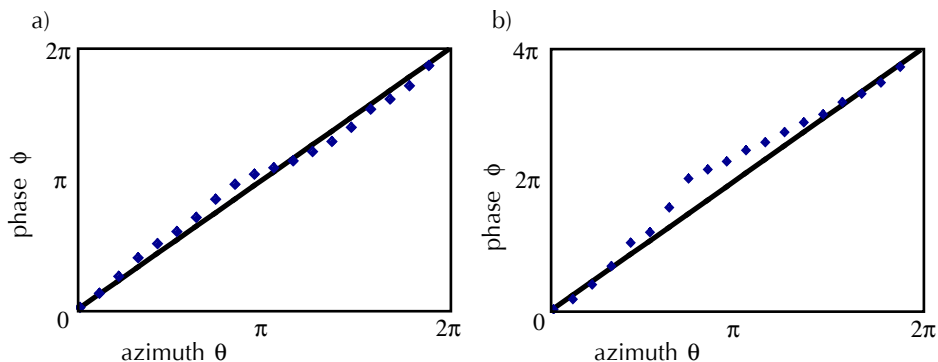


Figure 3.13: Unwrapped phase values around the beam axis for results shown in (a) Fig. 3.11 and (b) Fig. 3.12. The straight lines in both plots show $\phi = \ell\theta$.

The azimuthal variation in phase of these beams and isolated vortex makes them ideal for testing the phase measuring and vortex finding algorithms. Figures 3.11 and 3.12 show the results from scans of LG_0^1 and LG_0^2 beams respectively. The LG_0^1 looks very good and indeed the azimuthal variation of phase is very clear with a vortex in the middle. Figure 3.13 shows the measured phase around the axes of beams shown in Figs. 3.11 and 3.12 (at a 10 pixel radius). The match between the expected linear dependency of phase on azimuth is better for the $\ell = 1$ beam than the $\ell = 2$ beam. This is due to the splitting of the high-charge vortex into two singles. The splitting has created anisotropy of the phase contours close to the axis.

The 3D analysis of the data shows the vortex in the LG_0^1 beam as a near straight line following the axis (shown as a red line in Fig. 3.11). However, although the intensity images show the LG_0^2 to look very clean, analysis of the phase reveals that the high charge vortex is split into two single charge vortices. This is not so surprising considering the fragility of high charge vortices — any level of perturbation will cause a split, the closer the single charge vortices, the purer the LG mode. The separation of the vortices at $4z_r$ is very visible but still only a small fraction of w . The spiralling of the phase contours in Fig. 3.12 is also evidence that the curvature between the object and reference beams is slightly mismatched. This mismatch will cause

slight deformation to the phase fronts but will not change the positions of the vortices. As it is the vortex lines that are of interest, this mismatch can be tolerated.

3.7 Vortex structure as an indicator of beam purity

Although vortices are stable features of wavefields, the exact curve which a vortex line makes in real space can be very sensitive to perturbations (an extreme example being the high charge vortices just described). This can be useful if generating a beam to have very particular weightings of mode coefficients in that the vortex lines can act as a marker of beam purity, especially if the desired beam has near loop nucleation/annihilation or reconnection events.

In contributing to a paper on fractional orbital angular momentum [GOP⁺08] the apparatus and methods described earlier in this chapter were used to generate a beam composed of ten LG modes with an expectation of the orbital angular momentum per photon to be 6.5. The interference between the ten modes, largely due to the differing Gouy phases between them, caused transverse intensity variations and hence curved vortex lines.

The complex beam waist was calculated and propagated using a standard Fourier transform technique. This allowed the generation of a complex volume which could be searched for vortex lines. The resulting 3D vortex structure would then be used in comparison to experimentally acquired data. Figure 3.14 shows the vortex structures from both simulated and experimental data. The match is not perfect but several important matches, such as the opposing hairpin bends and similar deviations from straight line vortices indicate that the beam is indeed composed of the required mode weightings.

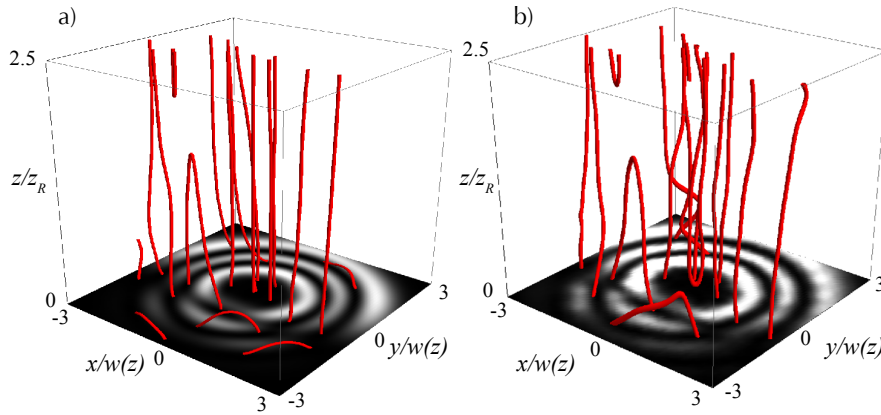


Figure 3.14: Three dimensional view of the vortex structure for a superposition of 10 modes and $M = 6.5$. (a) shows the numerical results and (b) the experimental measurements. Both vortex structures exhibit a number of topological features such as formation of a line of vortices and the existence of 'hairpins', connected nodal lines which cumulate in a turning point.

3.8 Polarisation measurements

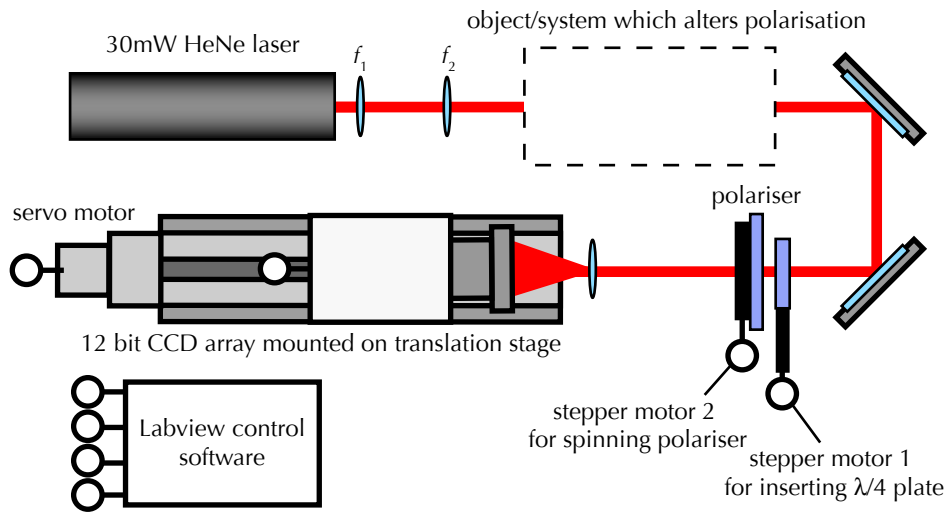


Figure 3.15: Apparatus for measuring Stokes parameters.

A different apparatus must be used to measure the polarisation state of a beam. Figure 3.15 shows the setup for measuring polarisation states. The

apparatus is much simpler than that in Fig. 3.1. Neither a reference beam or an SLM are required for the polarisation experiments. However, the algorithms used to acquire Stokes parameters (which uniquely define polarisation states) are very similar to those employed to extract phase information through interferometry.

3.8.1 Measuring Stokes parameters

The polarisation state at each point of a light beam is completely described by the Stokes parameters [BW59]:

$$\mathbf{S} = \begin{bmatrix} S_0 \\ S_1 \\ S_2 \\ S_3 \end{bmatrix} \quad (3.6)$$

Traditionally there are six measurements required to calculate stokes parameters, four measuring intensity of different linear components and two measuring the intensity of circular components. S_0 is the overall intensity, and the others are given by

$$S_1 = I_{0^\circ} - I_{90^\circ}, \quad S_2 = I_{45^\circ} - I_{135^\circ}, \quad S_3 = I_{\text{left}} - I_{\text{right}}, \quad (3.7)$$

where I_θ is the intensity of the linear polarisation at angle θ , and $I_{\text{left/right}}$ the intensity of the left/right circular polarisation.

These measurements can be laborious to complete manually, especially when many planes of measurements are required. Once automated, the parameters can be measured in a different way by making use of more than six measurements and using Fourier techniques similar to those used to measure phase in the previous sections.

A 12-bit CCD camera and imaging lens, mounted on a motorised stage, can be positioned to image any cross-section within the volume of interest [OPD06]. The camera is preceded by a linear polariser, which is rotated

continuously as measurements are taken [TGCS06]. For any specific cross-section, the polarisation at each point is obtained by acquiring a series of images corresponding to an advancing angular position of this polariser. Every pixel in the series (typically 16) of resulting images undergoes a sinusoidal intensity modulation. The Stokes parameters for each pixel are calculated from the Fourier components of this sinusoidal intensity (exactly as phase was extracted from interference measurements earlier),

$$S_0 = \sqrt{2/\pi}|\mathfrak{F}_1|, \quad S_1 + iS_2 = 2\sqrt{2/\pi}\mathfrak{F}_2, \quad (3.8)$$

where \mathfrak{F}_1 and \mathfrak{F}_2 are the complex first and second Fourier components. Inserting a $\lambda/4$ -waveplate before the polariser gives, after another full rotation of the polariser, a different Fourier transform for each pixel from whose second component $\mathfrak{F}_2^{\lambda/4}$, S_3 can be calculated:

$$S_3 = 2\sqrt{2/\pi}\text{Im}(\mathfrak{F}_2^{\lambda/4}). \quad (3.9)$$

Determining the polarisation in this way, based on many images, gives good measurement precision and a high degree of noise immunity. The process is automated and the Stokes parameters for every pixel in the cross-section of 1024×768 pixels can be found in approximately 10 seconds.

Once \mathbf{S} has been measured, the ellipticity and polarisation angle can be calculated by converting to spherical coordinates on the Poincare sphere (illustrated in chapter 2) using:

$$I = S_0, \quad (3.10)$$

$$p = \frac{\sqrt{S_1^2 + S_2^2 + S_3^2}}{S_0}, \quad (3.11)$$

$$2\theta = \arctan \frac{S_2}{S_1} \quad \text{and} \quad (3.12)$$

$$2\phi = \arctan \frac{S_3}{\sqrt{S_1^2 + S_2^2}}. \quad (3.13)$$

The topological features of interest are the polarisation singularities, C-points, and the lines of linear polarisation, L-lines. Extended into three-dimensions these features become C-lines and L-surfaces.

L surfaces are those on which $S_3 = 0$ and C lines are defined as the intersections of $S_1 = 0$ and $S_2 = 0$ (just as phase singularities are the intersections of $\xi = 0$ and $\eta = 0$). As described later, in chapter 9, the type of C line singularity may be determined using the Stokes parameters and their spatial derivatives.

3.8.2 Example polarisation measurements

Stress birefringence was used to create a light field with interesting yet simple enough properties to test measurement and data processing. A disc of glass contained in an aperture, with symmetrically placed screws around the perimeter, can be easily subject to enough stress to change the refractive properties across the disc without shattering it. Once stress has been applied to the disk, incident light will emerge with a spatially varying polarisation. An example of stress birefringence altering light can be seen in Fig. 3.16, where a Perspex ruler has been placed between crossed polarisers. Any light emerging from the final polariser can only do so as its polarisation state has been altered sufficiently to let it pass.

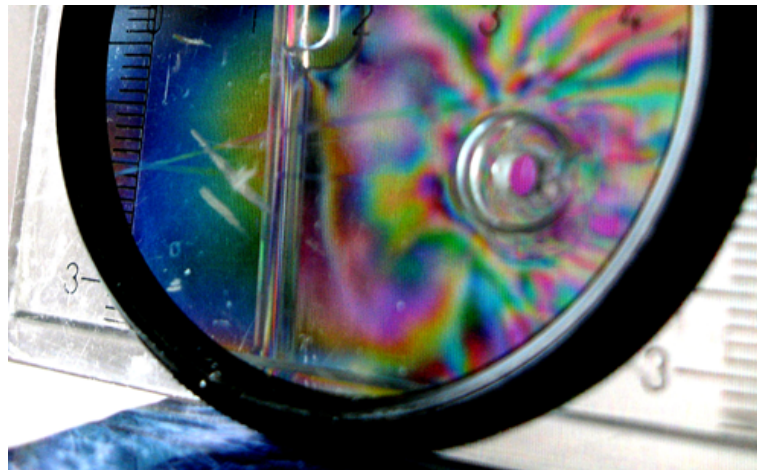


Figure 3.16: Perspex ruler between crossed polarisers. The stress birefringence is visible due to the different phase shifts undergone by different wavelengths .

Figures 3.17 and 3.18 show the results of automated measurements of Stokes parameters by drawing the polarisation ellipses and lines of linear polarisation described by $\mathbf{S}(\mathbf{r})$ over the intensity image $I = S_0$. Figure 3.17 shows the polarisation states of a beam (which was initially linearly polarised) after passing through a glass disk under stress. Figure 3.18 shows a result from the same setup but with the beam being initially circularly polarised. Both examples show Lemons and Stars and lines of linear polarisation separating regions of left- and right-handed polarisation.

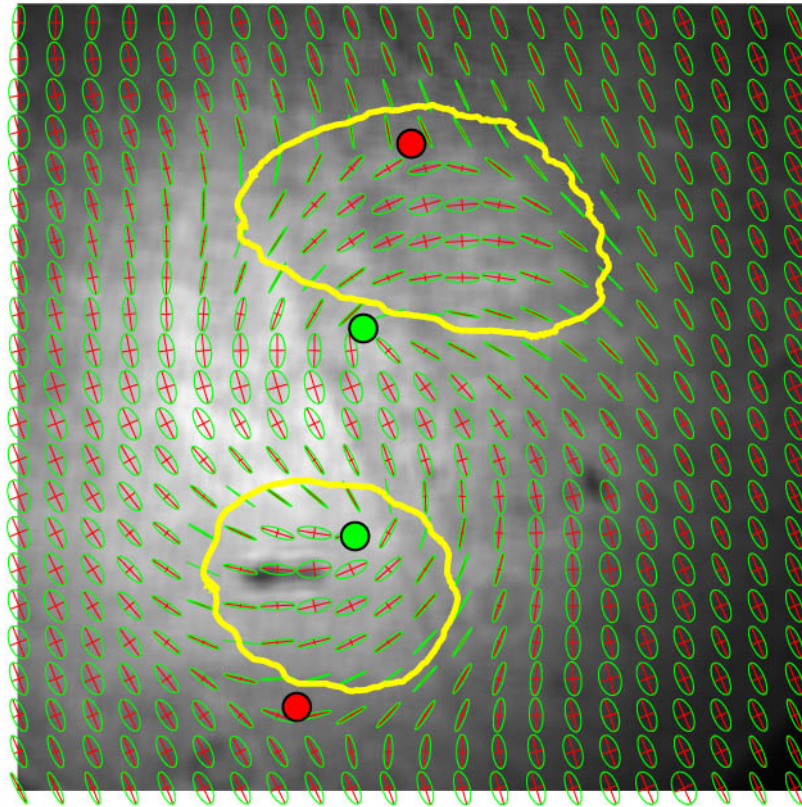


Figure 3.17: Measurement of polarisation state of a beam after linearly polarised light passed through a glass plate under stress. Lemon and Star type singularities are green and red dots respectively. The L lines are drawn in yellow.

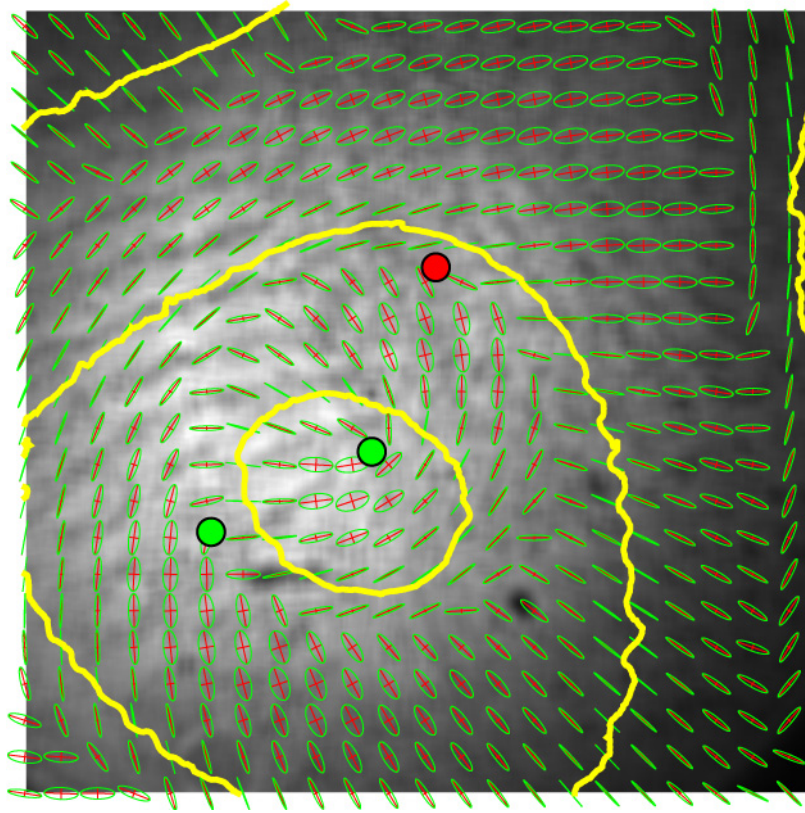


Figure 3.18: Measurement of polarisation state of a beam after circularly polarised light passed through a glass plate under stress. Lemon and Star type singularities are green and red dots respectively. The L lines are drawn in yellow

3.9 Summary

This chapter has described the general experimental setup to obtain volumetric complex data of optical fields, both scalar and vector. The demonstrations have shown how the vortex locating algorithms work and demonstrated the use of the apparatus for various types of optical fields from carefully created mode superpositions to arbitrary fields transmitted through glass plates. Throughout the thesis experimental results will be given and unless stated otherwise, they were obtained through use of the methods described here.

Illustrations of vortices in three dimensions

“The soul can not think without a picture”

— Aristotle, 384–322 BC

Chapters 1 and 2 explored the origins of research into optical vortices and described the basic properties of optical singularities. The purpose of this chapter is to describe various three dimensional structures that have been of interest to researchers and can be created in real Gaussian beams. It will highlight the three dimensional properties of the vortex lines and demonstrate changes in topology through changes in field parameters.

The first section will give a description of the elliptic umbilic diffraction catastrophe, which is an illustration of a field with both vortex lines and loops, experimental results will be given. The following sections will discuss vortex topology in four wave interference, linked vortex lines and the vortex structure resulting from a spiral phase plate. These three situations will be re-examined through numerical simulation observing the vortex lines evolve as an additional parameter is varied. The specific parameter changes are: the addition of a fourth wave to a field composed of three waves; the increase in

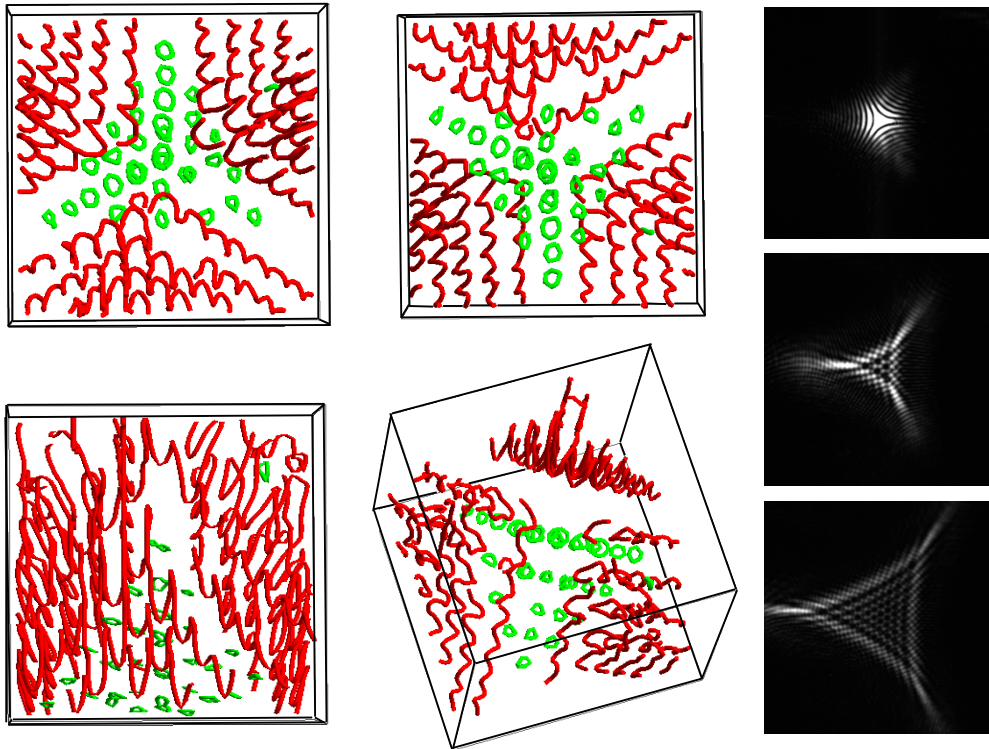


Figure 4.1: Experimental results of the elliptic umbilic diffraction catastrophe. Three different viewpoints are shown of the vortex structure with loops in green and lines in red. Three cross sections of intensity are also shown on the right.

height of a non-integer spiral phase step, and the perturbation that creates, and then dissolves, a vortex link in a specific combination of Laguerre-Gauss modes.

4.1 The elliptic umbilic diffraction catastrophe

The elliptic umbilic diffraction catastrophe was the first of the three diffraction catastrophes to be studied. It was also the first study that emphasised

the 3 dimensional nature of vortex lines. The easiest way to form an elliptic umbilic is to create a triangular lens by cutting a small equilateral triangle in a piece of cardboard and filling it with a drop of water. Light directed through this lens will create an elliptic umbilic diffraction catastrophe. This is how the experiment was carried out by Berry et. al. with the different cross sections corresponding to different heights above the lens being taken at the same plane as the drop evaporated, effectively scanning the focus through the imaging plane.

The elliptic umbilic is formed by six cusps creating a caustic surface, or focus (to aid this imagine two three sided pyramids one inverted on top of the other with each pyramid side being a cusp instead of a triangle). The vortex lines on the interior of this shape are hexagonal puckered loops in a regular array. On the outside the vortex lines form hairpins — coming in from infinity and turning around as they approach the caustic surface. The difference between the two regions is that one is dominated by four wave interference and the other by three. Why this would lead to the marked difference in topology of these regions will be examined in chapter 5.

Figure 4.1 shows a modern version of the experiment described in Ref. [BNW79]. These measurements were made by making a hologram according to the height mapping described by Berry for a water droplet, namely:

$$h(x, y) = H(1 - 9(x^2 + y^2)/L^2 + 6\sqrt{3}(x^3 - 3xy^2)/L^3). \quad (4.1)$$

Where h is the height of the droplet, H is the maximum height, and L is the length of the triangle side. For use on an SLM this height function was mapped to phase and added to a diffraction grating to diffract the elliptic umbilic away from the reflected zero order.

It can be seen from the results that space has been divided into two domains: vortex loops and vortex lines. This explanation as to why there is a distinct difference in topology on either side of the caustic surface is answered by looking at the number of interfering components. The interior of the caustic surface is dominated by four wave interference whilst the exterior is domi-

nated by three and two wave interference (see Ref. [BNW79] for a complete discussion). Four wave interference can result in vortex loops whereas three waves cannot. The manner in which these different areas of competing wave interference determine topology will be examined in chapter 5.

4.2 Vortex lines and a varying parameter

Optical vortex lines can evolve and undergo topological events. As a fourth parameter is varied (beyond the three spatial coordinates), small loops may nucleate or shrink to nothing, and lines may reconnect [BD01b, Nye04]. These topological events are analogous to the behaviour of quantized vortices in other physical systems [RA01].

For the examples below, the interference pattern between the constituent waves is calculated on a 256×256 lateral grid for 256 different planes, producing a cube of interference data. Examining the phase for each 2×2 grid of pixels allows the vortex locations to be identified by phase unwrapping. Within any single cross section the positions of vortex hairpins can be ambiguous and consequently the interference cube is examined along the three cartesian directions (as described in chapter 3). Once the list of vortex positions is generated, the vortex lines are plotted using the ray-tracing software, POVray. Repeating the calculations as one or more parameters are varied allows an animated sequence to be constructed. On a standard desktop computer (Pentium 4 3.2GHz), calculation times for each of these animated sequences amounts to a few hours.

The purpose of numerically calculating and illustrating the evolution of vortex line geometry in 3D is to elucidate important attributes of optical vortex behaviour which are difficult to understand in 2D.

The first situation considered is the addition of a fourth wave of varying amplitude into a superposition of three plane waves. Secondly, the vortex structure in a field propagating from a spiral phase plate is studied as the

height of the step varies. Finally, the creation and destruction of a vortex link in a specific superposition of Laguerre-Gauss beams as the amplitude of the perturbing beam changes is investigated.

4.2.1 Four wave interference

For two interfering plane waves, complete destructive interference can only occur when the two wave amplitudes are equal, resulting in interference fringes which, in three dimensions, are planes of zero intensity. More generally, a pre-requisite for complete destructive interference is that none of the interfering waves has an amplitude which exceeds the sum of the others. With three plane waves, the vortex lines are always straight and parallel, with a direction such that each wavevector has the same propagation component.

If a fourth wave is added, with an amplitude increasing from zero, the straight vortex lines become helices [Nye99]. As the amplitude increases, the vortex helices approach, touch, and undergo a reconnection, so the infinite vortex lines become closed vortex loops. The loops shrink to points and vanish as the amplitude of the fourth wave continues to increase beyond the sum of the other three [OPD06]. Thus, as a single parameter is varied in the interference of four plane waves, both types of topological event [BD07] occur.

Figure 4.2 is an animated sequence showing the four-wave interference pattern with three wave amplitudes fixed at $a_1 = a_2 = a_3 = 1$ while the fourth wave amplitude, a_4 , increases from zero to equal the sum of the other three. Although three amplitudes have been fixed, the adjustment of the fourth amplitude provides all possible topological configurations of four wave interference.

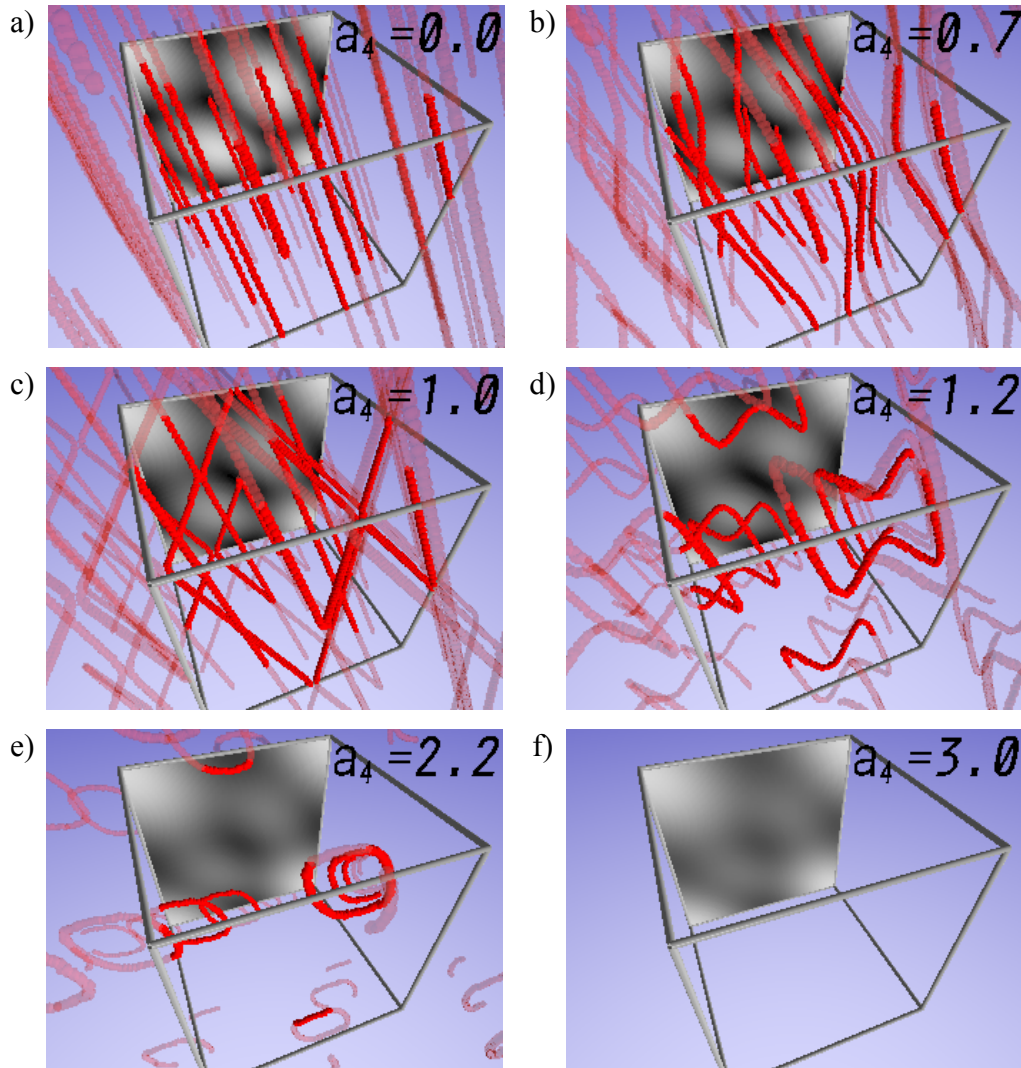


Figure 4.2: Vortex structure arising from four plane wave interference. The cube frame shows calculated volume extent. The (a – f) frames show how the vortex topology changes from lines to loops to smaller loops. Eventually as the amplitude is increased further (to $a_4 > a_1 + a_2 + a_3$), the loops vanish entirely.

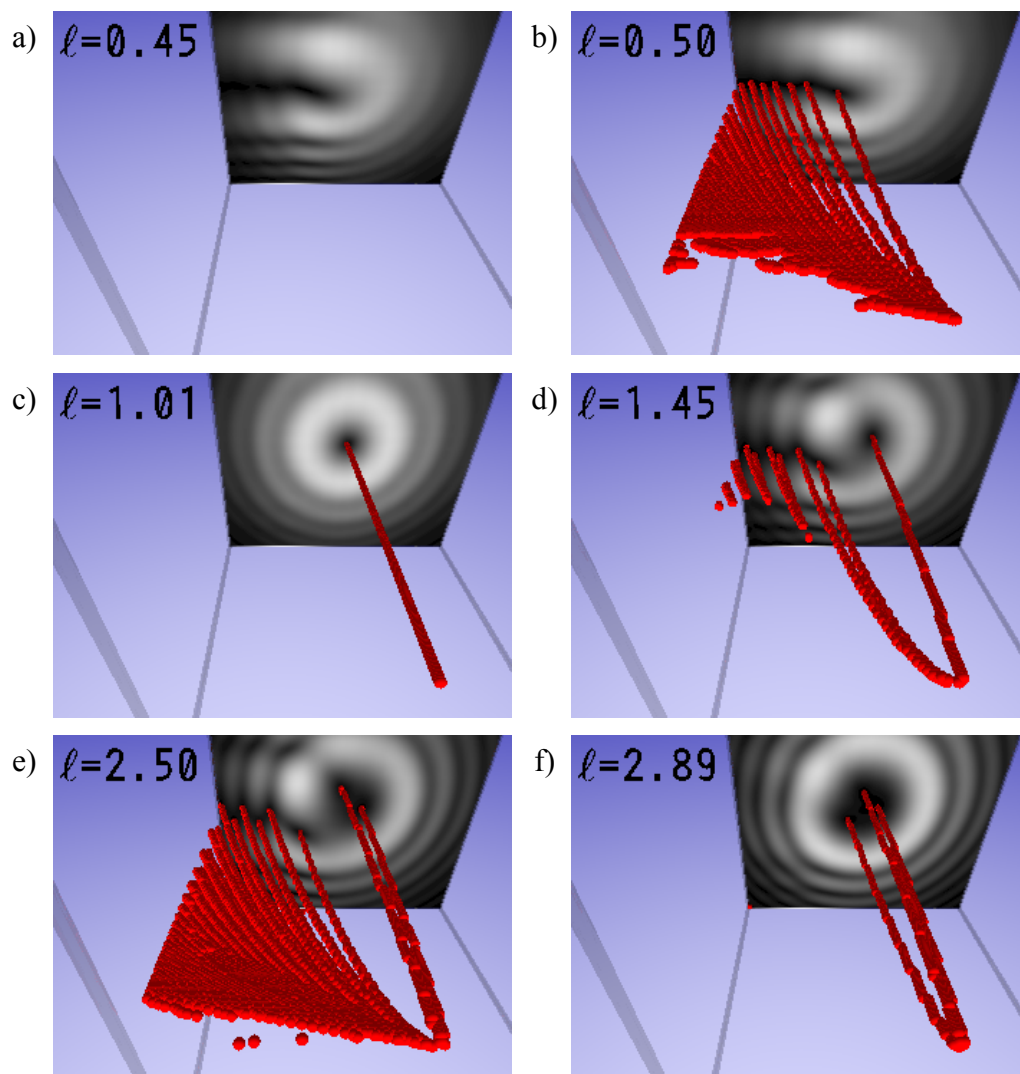


Figure 4.3: The vortex structure of a beam after passing through a spiral phase plate of step height $\ell\lambda$. Frames (a – f) show how this 3D structure changes as the step height is increased from $\ell = 0$ to $\ell = 3$. The greyscale plot represents the intensity after propagation of a small fraction of the Rayleigh range of the beam.

4.2.2 Spiral phase plate

For studies of optical orbital angular momentum, it is common to create a single optical vortex line along the beam axis. A common method is to use a spiral phase plate, whose optical thickness increases with azimuthal angle, so that a normally incident, phase flat wave of the correct wavelength acquires a phase factor $\exp(i\ell\phi)$ and an associated orbital angular momentum of $\ell\hbar$ per photon. There are practical difficulties in matching the discontinuity height exactly to the illumination wavelength, so that in experimental realizations, the azimuthal phase change ℓ is not an integer multiple of 2π .

It was shown theoretically in Ref. [Ber04] that when a plane wave illuminates a spiral phase plate, the discontinuity from half-integer ℓ leads to a radial sequence of vortices of alternating handedness along the original discontinuity. In the far field, this string of vortices is present whenever ℓ is not an integer. These predictions have been confirmed by experiment [LYP04], in which plane wave illumination was approximated by a large-waist Gaussian beam.

The far field of such a large Gaussian beam contains a sequence of alternating-sign vortices. The 3D vortex structure that generates such a sequence must be that of ‘hairpin’ vortex lines, where adjacent pairs of (opposite charge) vortex points in the far field are part of the same vortex line. The turning point of each hairpin extends towards the near field of the phase plate, and is closest to the phase plate for half integer values of ℓ . The total number of hairpins and their proximity to the phase plate depends upon the size of the illuminating Gaussian beam.

Figure 4.3 is an animated sequence of the vortex structure as the step height of the spiral phase plate is varied from $\ell = 0$ to $\ell = 3$.

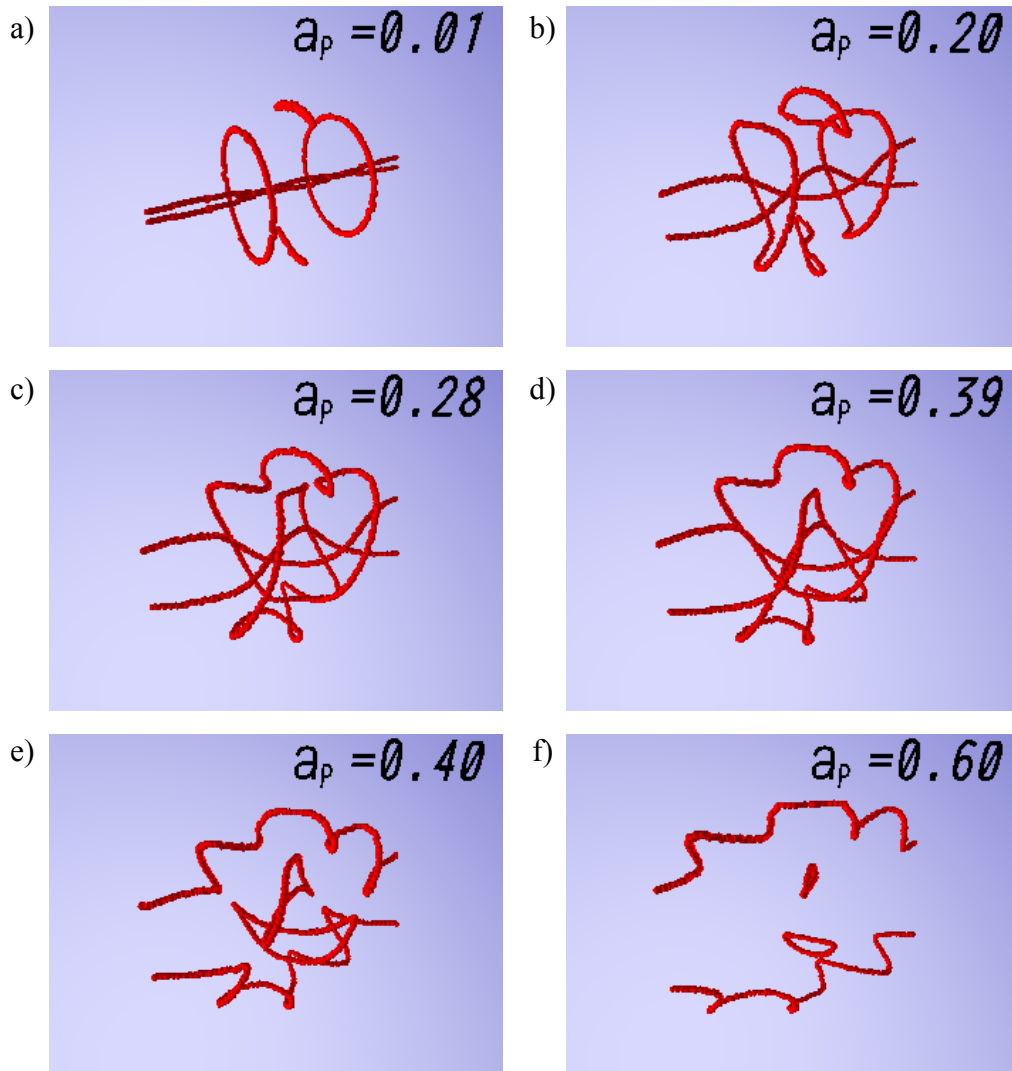


Figure 4.4: Vortex configuration of Laguerre-Gauss beam superposition giving a vortex link [LDCP05]. The figure depicts the vortex structure of the initial field which is perturbed to create a vortex link. The frames (a –f) show the structure undergoing a topological transition as the perturbation, a_p is increased from 0 to 0.6 the link is created through reconnection when $a_p = 0.3$, and dissolves through further reconnections when $a_p = 0.5$. The vortex loops are linked in frames (c) and (d).

4.2.3 Vortex links

In real beams of finite extent, the topology of optical vortices can be quite intricate, but may still be controlled. It was proposed in Ref. [BD01b] that certain combinations of four beams would have vortices that are linked or knotted; in principle, any torus knot or link is possible with this construction. The superposition in the knot construction involves three coaxial, copropagating beams carrying equal, nonzero angular momentum (e.g. Bessel beams [BD01b], polynomial beams [BD01a] or Laguerre-Gauss beams [LDCP05]), with particular amplitudes. These are perturbed by a further beam with no vortices (e.g. a J_0 Bessel beam, plane wave, or Gaussian beam).

In paraxial beams, the unperturbed vortex configuration consists of a system of unlinked, axisymmetric rings, one of which has zero strength (the phase does not change in a loop around it). As the amplitude of the perturbation increases, these rings deform, crescent-shaped loops nucleate from the zero strength loop, and the central vortex line unfolds to an n -stranded helix [BD01c]. At some lower critical value of the perturbation amplitude, the vortex loops reconnect to give the appropriate torus knot or link. At an upper critical value, there are further reconnections between the knot or link and the axial helix, dissolving the knot. This controlled method of knot and link creation was implemented experimentally in Refs. [LDCP04b, LDCP05], in which a Hopf link ((2,2) torus link) and trefoil knot ((3,2) torus knot) were synthesized.

The process in which the trefoil link forms and then dissolves via reconnections, as the amplitude of the perturbing beam is increased, is illustrated in Figure 4.4.

4.3 Discussion

The evolution of optical vortex points in a 2D observation plane can be better understood as a pattern of lines embedded within the volume of a light beam. For monochromatic fields, the vortex lines are stationary in space, so possess no temporal dynamics.

The elliptic umbilic diffraction catastrophe serves as the simplest example of a 3D vortex structure involving multiple topologies resulting from a basic optical process. It also contains an example of how differing number of waves can interfere to produce different vortex topologies, and indeed was an inspiration to understand why this occurs (see chapter 5).

Simple examples of how the vortex lines evolve under the change of an additional parameter have been illustrated here. In the first and third examples, this parameter was the amplitude of an additional wave in the superposition whereas in the second it was the change of an initial field profile). Other examples of vortex line evolution have been discussed elsewhere, such as Refs. [Nye03, Nye06], in which vortices in diffraction patterns approach the characteristic configuration of the canonical diffraction catastrophes, as the dimension of the diffraction aperture approaches infinity.

Since the vortices are zeros in the complex scalar amplitude, the dependence of their position with respect to the parameters in the situations illustrated is highly nonlinear, just as the vortex lines are not straight upon propagation [RLS97]. The most significant events in the evolution of vortex lines are loop nucleation/vanishing and reconnection; these events occur stably as a parameter is varied [Nye04] (they are codimension 4); with dependence on further parameters, more complicated topological interactions may occur [Nye03].

Plane-wave interference

As optical vortices are zeroes of a complex scalar field it is helpful to examine the interference between plane waves and examine how the nodal structure is affected by amplitudes and phases of individual components. This chapter details how vortex structure and topology is related to the plane-wave components of the field, showing how for superpositions of four waves the topology is defined solely by the real amplitudes of the plane-wave components.

5.1 Phasors

The arguments that follow in this chapter rely on an understanding of the phasor representation of waves [Goo85]. A point in a complex field can be represented as an addition of vectors, called phasors, on the complex plane. That is, the total field at a point is calculated in the Argand plane by the vector addition of the individual phasors, $\boldsymbol{\psi}_n$, for $n = 1, \dots, N$. Each of these vectors corresponds to a wavevector, \mathbf{k}_n , and has amplitude $a_n = |\boldsymbol{\psi}_n|$ and phase $\phi_n = \arg \boldsymbol{\psi}_n$. The phasors are labeled in order of decreasing magnitude $a_1 \geq a_2 \geq \dots \geq a_N$. A simple example of phasor addition is

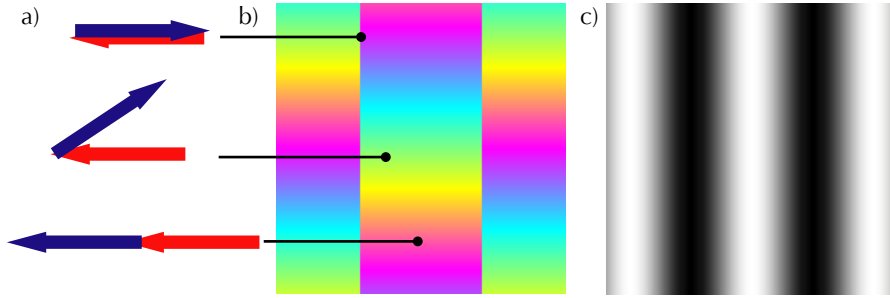


Figure 5.1: Two wave interference (equal-amplitude). a) Three possible phasor arrangements of $(\psi_1 + \psi_2)$ corresponding to zero intensity (top), intermediate intensity (middle) and maximum intensity (bottom). The corresponding spatial locations marked on a phase and intensity cross-section of the 3D field are shown in (b) and (c) respectively.

shown in Fig. 5.1 for two equal-amplitude plane waves.

If the point under study is now moved smoothly through the field, each phasor will begin to rotate at a rate dependent on the path taken. The rate of rotation along a path is related to the projection of the wavevector onto the path taken, $(\hat{\mathbf{k}}_n \cdot \hat{\mathbf{t}})$, where $\hat{\mathbf{t}}$ is the unit tangent of the path and \mathbf{k}_n is the wavevector of the phasor in question. If the path is a straight line then the phasor will rotate at a constant rate.

Using this description, a point is on a vortex line if the sum of the phasors is zero,

$$\sum_{n=1}^N \psi_n = 0. \quad (5.1)$$

This leads to the result that vortex structure and topology of three, four and five wave interference is constrained by the geometrical properties of triangles, quadrilaterals and pentagons respectively. These constraints will be explored in the next few sections.

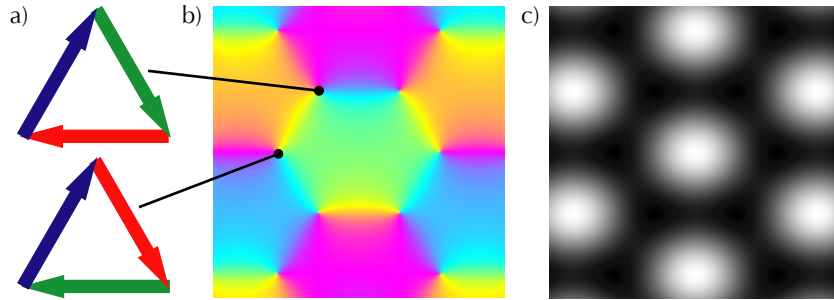


Figure 5.2: Three-wave interference. a) The only possible phasor arrangements that satisfy $(\psi_1 + \psi_2 + \psi_3) = 0$. Two examples are marked on a phase cross-section (b) of the 3D field and the intensity is shown in (c). Each phasor arrangement (corresponding to $s = \pm 1$) appears in a close-packed hexagonal lattice. The displacement of the two results in the honeycomb lattice observed.

5.2 Interference between two and three waves

Interference between two waves is relatively simple. Cancellation between the waves can only occur if both waves have the same amplitude and opposite phase, $\psi_1 = -\psi_2$. When both amplitudes are the same, a volume of the field will contain equally spaced parallel planes of zero intensity (see Fig. 5.1 for a cross-section of two-wave interference). This is a very special and unstable case. In this field there are no vortices; however, the slightest perturbation breaks these planes into an array of vortex lines — a structure governed by three-wave interference.

Since labeling is in order of decreasing magnitude, for a superposition of three waves, cancellation can occur only if $a_1 \leq a_2 + a_3$, allowing a triangular configuration of the phasors, i.e.

$$\psi_1 + \psi_2 + \psi_3 = 0. \quad (5.2)$$

Fig. 5.2 shows an illustration of this configuration alongside cross-sections of phase and intensity of the corresponding field.

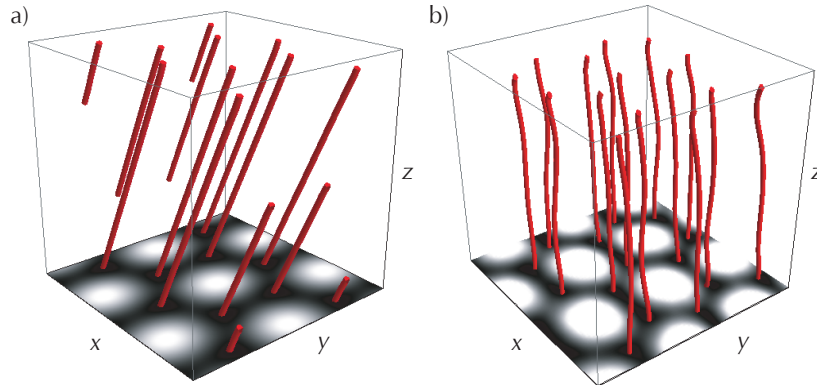


Figure 5.3: Examples of vortex structure arising from three-wave interference. The two frames show an intensity cross-section (bottom) and vortex lines in a simulated field (a) and a different, experimentally created and measured, field (b).

Depending on the ordering of the phasor addition, this triangle may be reflected or rotated but its shape cannot be changed along a vortex line. When moving along a vortex line, the phasor triangle rotates. The triangle can only remain closed if the three phasors rotate with the same frequency. This happens along a straight line, and the direction is [NN87]

$$\mathbf{k}_1 \times \mathbf{k}_2 + \mathbf{k}_2 \times \mathbf{k}_3 + \mathbf{k}_3 \times \mathbf{k}_1. \quad (5.3)$$

Therefore the vortex lines are straight and parallel to each other. Figure 5.3 shows the vortex lines from both simulated and experimentally measured fields. The experimental figure was produced using the methods outlined in chapter 3.

The honeycomb-lattice arrangement of these lines can be understood by looking at the clockwise arrangement of the phasors. The two possibilities of phase configurations that close the phasor triangle differ in that the vortex lines corresponding to them have different topological charge. The positions in a plane that satisfy Eqn. 5.1 are close-packed hexagonal for each charge. Two hexagonal lattices displaced from each other result in the honeycomb lattice observed in Fig. 5.2.

5.3 Interference between four waves

Four wave interference allows more flexibility in the phasor configuration. This flexibility extends to allowing different topologies. However, the limitations are still very apparent. Firstly, the vortex lines must be curved as there is no direction in space in which the phasors will all rotate with the same frequency — the phasor addition may only remain closed if they rotate at different, varying frequencies (there is one special case in which all \mathbf{k}_n have the same \mathbf{k}_r i.e. in which they are distributed on a ring). The exact path of a vortex line is a result of the particular \mathbf{k}_n in the superposition. However, due to the geometrical constraints of the quadrilateral configuration of phasors, topological questions can be answered about general four-wave superpositions.

For a superposition of four waves, cancellation can only occur if $a_1 \leq a_2 + a_3 + a_4$. With the magnitudes and wavevectors of the four waves fixed, the relative phases constitute three additional degrees of freedom. All possible phase relationships are explored throughout the three-dimensional field (i.e. all possible shapes of quadrilateral with sides a_1, a_2, a_3 and a_4). Consequently, a change to the initial phase of any of the superposed waves results only in a spatial translation, and does not affect any aspect of the vortex geometry.

The result is that vortex topology in such fields is governed by the real amplitudes of the waves. In fact, two topologies are possible, with a transition in between. The topology depends upon the following relations:

$$a_1 + a_4 < a_2 + a_3 \quad (\text{lines}), \quad (5.4)$$

$$a_1 + a_4 = a_2 + a_3 \quad (\text{reconnections}), \quad (5.5)$$

$$a_1 + a_4 > a_2 + a_3 \quad (\text{loops}). \quad (5.6)$$

When Eqn. 5.4 is satisfied, the phasor addition is similar to the three-wave case but with the addition of a small fourth phasor that can execute full 2π revolutions around the other three. This allows the straight-line vortices of the three-wave interference to deviate from their original path to form

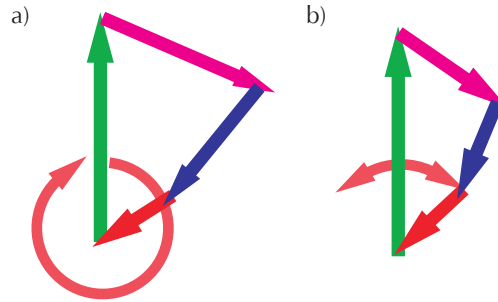


Figure 5.4: Four-wave interference. The amplitudes in (a) satisfy $a_1 + a_4 < a_2 + a_3$, allowing one of the phasors to make full 2π revolutions around the other three, resulting in an array of helical vortex lines. The amplitudes in (b) satisfy $a_1 + a_4 > a_2 + a_3$, restricting the phasors to make maximum angles less than 2π with each other, resulting in an array of vortex loops.

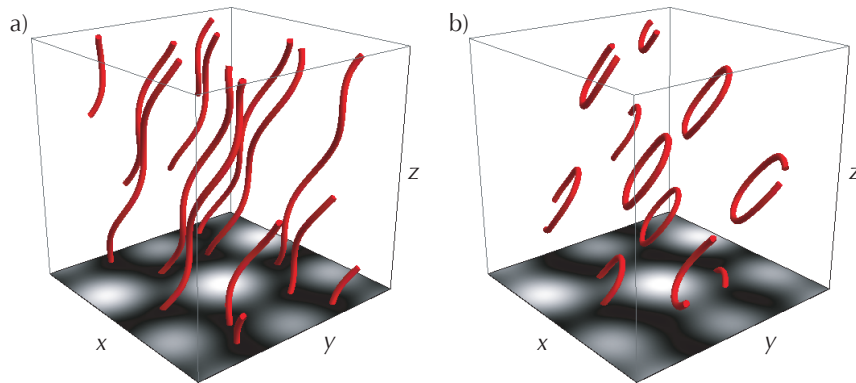


Figure 5.5: Possible vortex topologies resulting from four-wave interference. The amplitudes in (a) satisfy $a_1 + a_4 < a_2 + a_3$, resulting in an array of helical vortex lines. The amplitudes in (b) satisfy $a_1 + a_4 > a_2 + a_3$, resulting in an array of vortex loops.

irregular helices which have an ‘axis’ in the direction of Eqn. 5.3.

Now consider the smallest amplitude wave, a_4 , growing in size relative to a_1 . At some point the situation is reached where Eqn. 5.6 is satisfied. Now the quadrilateral formed by the phasors can only deform to some maximum angle between phasors. Constant clockwise or counter-clockwise movement between phasors is equivalent to moving in some spatial direction in the field. As phasors can only move to a maximum angle, vortex lines can exist

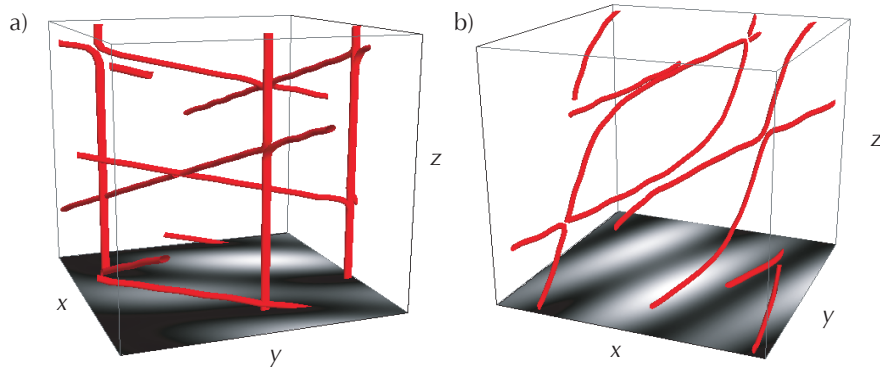


Figure 5.6: Vortex structure resulting from four-wave interference with $a_1 + a_4 = a_2 + a_3$. In (a), $a_1 = a_2 = a_3 = a_4$, resulting in three arrays of straight vortex lines which intersect. In (b), $a_1 = 1, a_2 = 0.7, a_3 = 0.6$ and $a_4 = 0.3$, resulting in curved but intersecting vortex lines. Both have ambiguous topologies.

within a maximum space — they are compact, existing within a certain range $(\Delta x, \Delta y, \Delta z)$. Therefore the vortex lines form loops. The phasor additions are illustrated in Fig. 5.4 and examples of the two possible vortex topologies are shown in Fig. 5.5.

It is helpful to imagine the helices of Eqn. 5.4 becoming more deformed, with larger curves as the smallest amplitude, a_4 , increases. At some point the increase in this amplitude causes the curves to extend far enough to connect with adjacent lines. As this point is passed each pair of helices (one of each $s = \pm 1$) ‘dissolves’ into a series of closely spaced, identical loops.

The transition between the two topologies is the point at which Eqn. 5.5 is satisfied and it is now possible for the phasor quadrilateral to become flat. The result of this flat phasor configuration is highlighted by looking at four waves of equal amplitude.

When the four waves have the same magnitude, the closed loop of phasors forms a rhombus, where $\psi_1 = -\psi_3$ and $\psi_2 = -\psi_4$. The vortex follows the intersection of two planes, determined by the two-wave interference described above (for waves 1 and 3, and 2 and 4), and is therefore again a straight line. However, under different orderings, a rhombus is also possible

if $\psi_1 = -\psi_2$ and $\psi_3 = -\psi_4$ or $\psi_1 = -\psi_4$ and $\psi_2 = -\psi_3$. Hence, there are three characteristic straight line vortex directions, along which the rhombus rotates and deforms. As the rhombus deforms, it may pass through a flat configuration. At this point, the phasor pairs are identical, and the vortex lines cross. So the vortex structure for four waves of equal amplitude consists of three arrays of straight lines which intersect, making the vortex topology degenerate. More generally when Eqn. 5.5 is satisfied the vortex lines are curved, but still cross at reconnections when the phasor quadrilateral becomes flat. Figure 5.6 shows two examples of vortex lines in four-wave superpositions with reconnections.

5.4 Experimental results

The four-wave superpositions described here were synthesized experimentally using a spatial light modulator (SLM) as a hologram. The SLM is addressed to produce a k -space distribution of plane waves. The plane of the SLM is imaged to a CCD array where the interference patterns are recorded as described in chapter 3. The results for amplitudes corresponding to lines and loops are plotted in Fig. 5.7. The transition between these two topologies was not experimentally observed due to the unstable nature of reconnections — very slight perturbations cause the field to be in either a line or loop state.

The configurations of waves chosen for the experiment were those with a rational relation between their k_x and k_y numbers. This causes the field to be periodic across the overlapping region between waves. This periodicity aids in observing the topology of the vortex lines. It can also be seen from the Fourier-plane images in Fig. 5.7 that the waves have a Gaussian spread around the four desired wave vectors. This spread in k -space does not affect the topology of the field as each Gaussian spot is coherent and will not cause additional destructive interference in the field. At most it could cause minor perturbations in the magnitude of the phasors ψ_n on propagation, which is

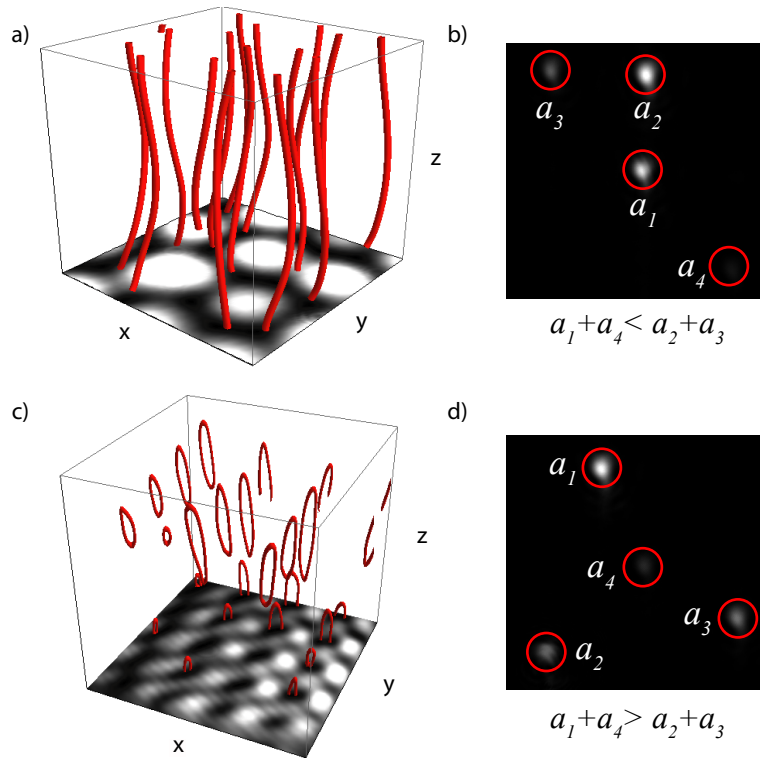


Figure 5.7: Measured vortex lines obtained by interfering four waves and manipulating the amplitudes using an SLM to satisfy (a) Eqn. 5.4, resulting in helical vortex lines and (c) Eqn. 5.6, resulting in vortex loops. Parts (b) and (d) show intensity images captured in the Fourier plane of (a) and (c) respectively, the red circles highlight the locations of the waves. The waves are ordered in decreasing amplitude.

only important if the field is close to the reconnection state described by Eqn 5.5.

5.5 Interference between more waves

For interference between five waves, cancellation requires the phasors to lie on a pentagon (up to reordering), and the geometry of the curved vortex lines cannot be simply described. Figure 5.8 shows superpositions with the same configuration of waves but with different choices of relative phases. There

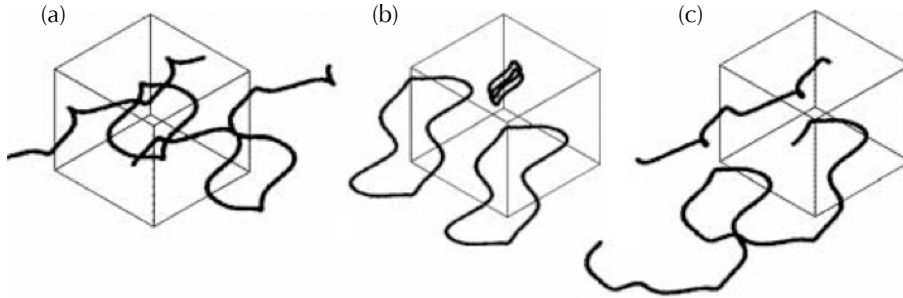


Figure 5.8: Illustration of how vortex topology is sensitive to phase values for 5 or more waves. In (a) the vortex lines are formed by a 5 wave superposition, there are two loops and two lines. In (b) the phase of one wave is changed by $\pi/2$ resulting in four loops. In (c) the phase of the same wave is now adjusted to $\pi/3$ resulting in two lines.

are four relative phases, so translation in three dimensions is insufficient to account for all possible phase relationships — the pattern is not specified uniquely by the magnitudes alone. This extends to arbitrary numbers of interfering waves, where optical-vortex topology is generally complicated.

5.6 High-order vortices and plane waves

It is possible to create a high-charge vortex with just five plane waves. In fact, to create a vortex of charge s the field must be composed of at least $N = (2s + 1)$ waves. Each of these waves must be equidistant from each other on the ring in k -space of radius \mathbf{k}_r and have a complex amplitude of $\exp(is\theta)$. This is essentially a sampled Bessel ring. Figures 5.9 and 5.10 show experimentally generated high-charge vortices from a few plane waves. Close inspection reveals that the high-charge vortex is actually split into several single-charge vortices. Again this is due to small perturbations in the system. Integrating the phase azimuthally very close to the axis (around 20 pixels away, corresponding to a few microns) encloses the single vortices and s can be measured. Figures 5.9 and 5.10 show the expected result, $s = (N - 1)/2$. Due to the waves composing these beams having the same \mathbf{k}_r , the resulting

field is propagation-invariant and the vortex lines are straight and parallel to the z axis.

5.7 Conclusions

In this chapter the topology of optical vortex lines in three-dimensional superpositions of small numbers of plane waves has been explained. Unlike superpositions of many plane waves, the topology of vortices in three- and four-wave superpositions is relatively restricted, and can be understood completely using phasor geometry. The characteristic tangle of vortex lines that is familiar for more general, many-wave superpositions begins for five waves. Some of the features described here occur in diffraction catastrophes [BNW79], where certain domains can be asymptotically approximated by superpositions of a few plane waves. In particular, four-wave interference patterns occur in the hyperbolic umbilic diffraction catastrophe [Nye06], which notably has a region in which phase singularities intersect and can be asymptotically approximated by a superposition of four plane waves of equal amplitude. It should be noted that, although the experimental and numerical illustrations required periodicity, the theoretical justification of these geometries using phasors does not, and applies for general superpositions of plane waves. The phasor methods we have employed here might prove useful more generally in the analysis of optical vortices, for instance in describing the anisotropy of optical vortex cores [BD00], as well as how the curvature, phase structure and anisotropy changes along an optical vortex line [Den04].

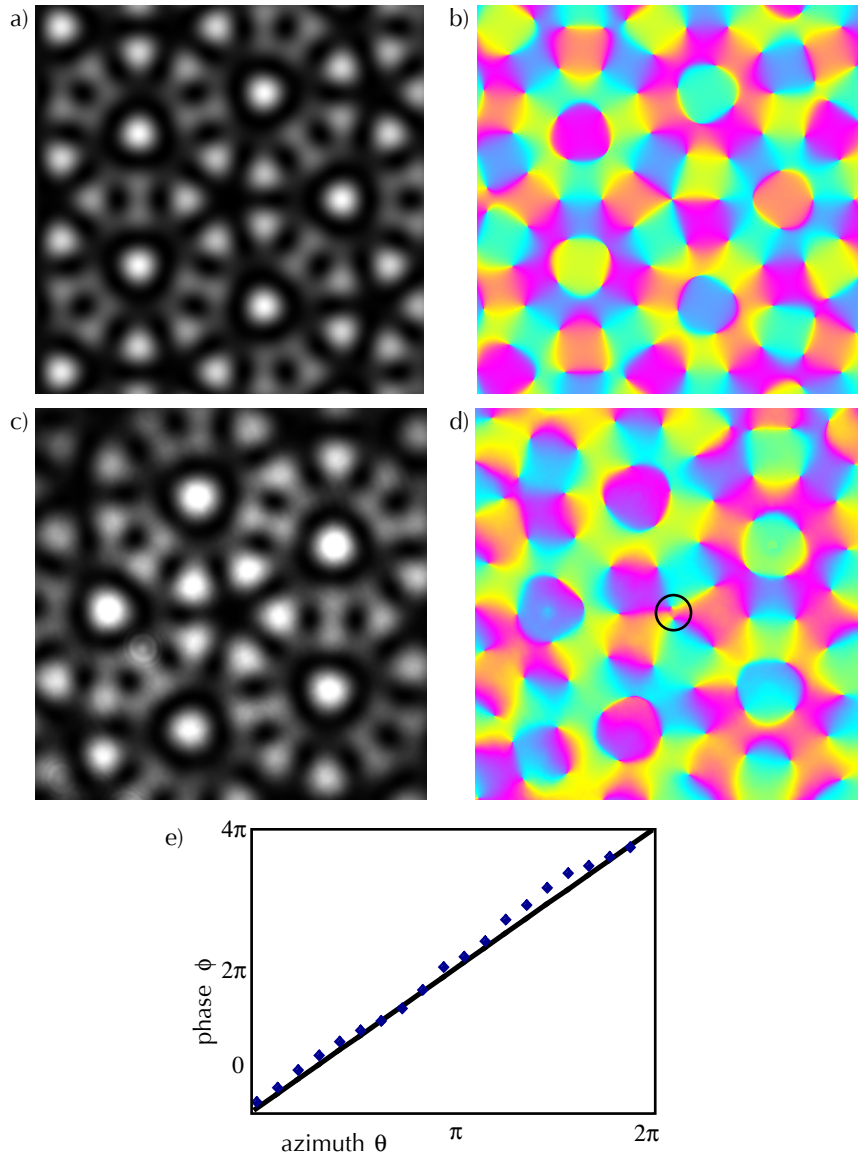


Figure 5.9: Vortex of charge $s = 2$ created by the addition of 5 plane waves. Shown are the intensity and phase of the simulated fields (a, b) and experimental measurements (c, d). The black ring in (d) shows the integration path for the unwrapped phase data in (e). The straight line in the plot is the expected $\phi = 2\theta$ near the axis.

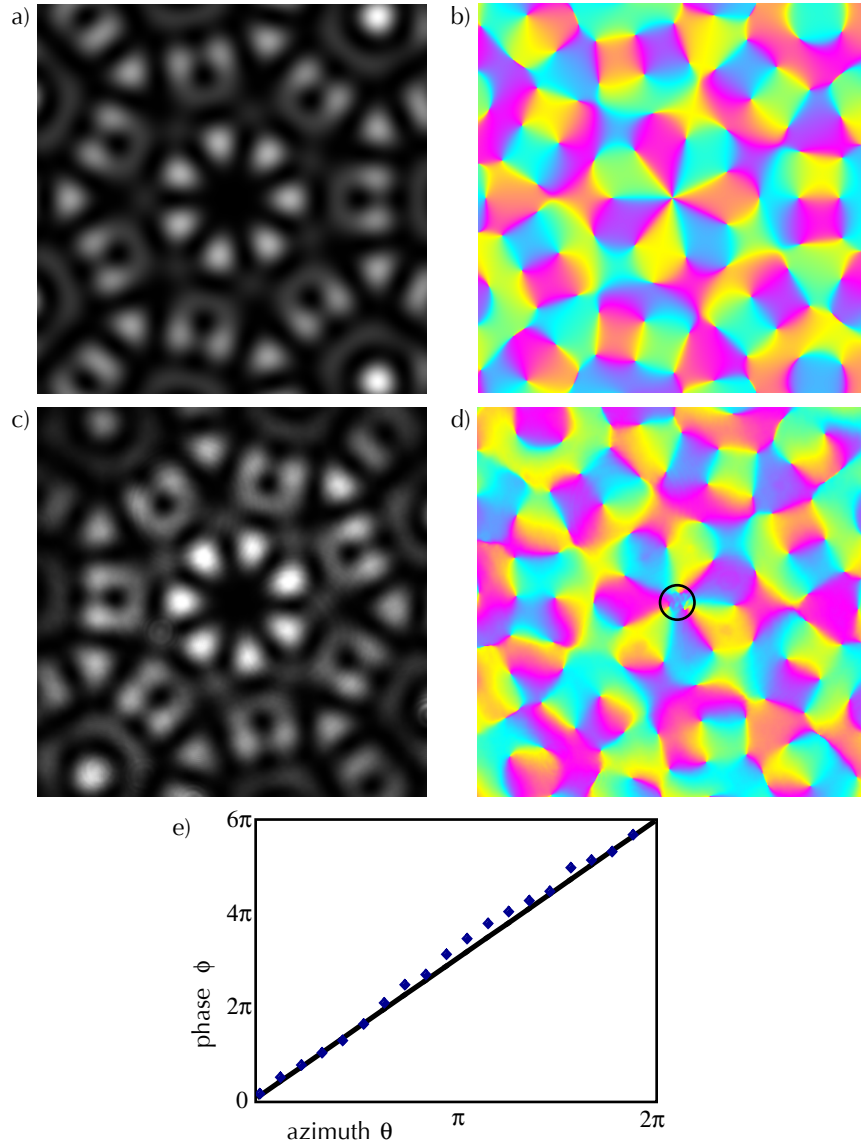


Figure 5.10: Vortex of charge $s = 3$ created by the addition of 7 plane waves. Shown are the intensity and phase of the simulated fields (a, b) and experimental measurements (c, d). The black ring in (d) shows the integration path for the unwrapped phase data in (e). The straight line in the plot is the expected $\phi = 3\theta$ near the axis.

CHAPTER 6

Random wave-fields

“Nature uses only the longest threads to weave her patterns, so that each small piece of her fabric reveals the organization of the entire tapestry”

— Richard P. Feynman

As laser speckle is the interference pattern generated by the random scattering of a coherent source, it can be described as a superposition of a large number of random plane waves. For three and four plane waves, the possible vortex topologies are arrays of infinite straight or helical lines, or planar loops (see Chapter 5). When more plane waves are added at random, the three-dimensional topology becomes more complicated, and its statistics has hitherto lacked any systematic study. Nevertheless, this statistical topology is universal to random linear wave superpositions regardless of the physical system that they describe [Kib07]. Superficially similar quantized vortex line structures have been much studied in fields as diverse as BECs [SWNA07], superfluid turbulence [Sch88] and cosmic strings [VV84, HK95].

This chapter will detail the model and algorithms used to generate and analyse the random wave-field vortex data.

6.1 Model

The results from simulation are derived from calculating the values of complex scalar fields at discrete points on a 3D grid (representing real space) and then searching the grid for vortices before sorting them into separate vortex structures for analysis.

The field values are calculated by summing a discrete number of plane waves with wavevectors, \mathbf{k} :

$$\Psi(\mathbf{r}) = \sum_{\mathbf{k}} \psi_{\mathbf{k}} e^{i(\mathbf{k}\cdot\mathbf{r})}, \quad (6.1)$$

where the complex amplitudes of each wave is:

$$\psi_{\mathbf{k}} = a_{\mathbf{k}} e^{i\phi_{\mathbf{k}}} \quad (6.2)$$

As we are interested in random fields, the real and imaginary parts of the complex amplitude are Gaussian randomly distributed. This results in a uniform distribution of phases, $\phi_{\mathbf{k}}$, and a Rayleigh distribution [Pap84] of real amplitudes, $a_{\mathbf{k}}$.

Any finite number of plane waves with random magnitude, phase and direction can be combined and the resulting interference pattern calculated over a finite volume, the scale of the calculation being limited only by the computer's processing power and memory capacity. The next step is to search element by element (voxel by voxel) for vortices. As singularities of the phase, the vortices can be located with very small closed integral paths (see chapter 3 for further details on vortex finding).

The end result is a 3D array with certain voxels being 'flagged' as containing a vortex. These vortex positions form connected lines through the 3D array, either connecting back onto themselves or terminating at the edge of the modeled volume. Once such an array has been obtained, the vortex positions can be sorted into individual structures. However, the topology of the vortex lines that connect to the edge of the volume is ambiguous and cannot be resolved for any finite calculation.

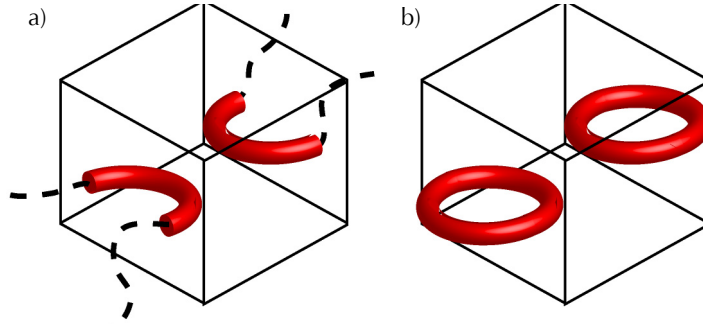


Figure 6.1: Illustration of how a periodic cell can be used to determine topology. In (a) the topology of the two vortex lines is ambiguous as the edge of the calculated volume intersects them. In (b) the cell is periodic and the topology of the vortex lines can be determined by wrapping the faces onto each other.

6.1.1 Talbot cells

One approach to solving this ambiguity is to create a field which is both laterally and axially periodic. In this case the lines can be ‘wrapped’ back through the array and will always connect back to their respective origins. Any vortex line can be traced out of the initial volume, if necessary, and through the neighbouring (identical) cell and traced back to its starting point, with a full path either (a) wholly within the initial cell, (b) entering neighbouring cells but then returning to the initial cell (illustrated in Fig. 6.1), or (c) terminating at the corresponding initial position but in a translated cell. a) and b) correspond to closed vortex loops and (c) is an infinite vortex line, albeit one whose structure is periodically repeated.

To model such superpositions, sets of plane waves of wavelength $\lambda = 2\pi/k_0$, are generated on a k -space grid of spacing δk and extent ΔK (shown in Fig. 6.2). The periodic cells that result from such superpositions are called Talbot cells, in reference to the Talbot effect in which a grating is periodically imaged along the propagation axis [Tal36]. Using the paraxial approxima-

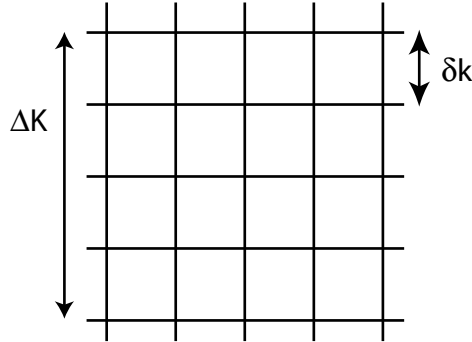


Figure 6.2: The construction of k -space to create a periodic 3D wavefield using the paraxial approximation. The grid shown is a 5×5 k -space (allowing for fields composed of up to 25 waves) where ΔK is the full width of the array and δk is the grid spacing which results in the Talbot effect. The sites of this grid are the locations of the plane wave components of the periodic field.

tion, the transverse, x_T, y_T , and axial, z_T , periodicities are:

$$x_T = y_T = \frac{2\pi}{\delta k} \quad (6.3)$$

$$z_T = \frac{4\pi k_0}{\delta k^2}. \quad (6.4)$$

The scaling between the periodicities mean that a light field of low numerical aperture ($\delta k/k_0 \approx 10^{-3}$) corresponds to a Talbot cell millimetres wide and metres in length. This allows the paraxial approximation to be used in propagating the waves in real space.

So far, a model has been constructed which uses gaussian random waves on a square grid in k -space to create a periodic spatial 3D array.

6.1.2 Volume resolution

In order to calculate fields and identify the vortex structure, the volumetric resolution must be set so as to fully resolve the vortex lines. One benefit of the nature of these singularities is that it is impossible for the lines to simply end in the calculated volume. No matter how horribly unresolved a field is,

the vortex lines will be continuous, either spanning the volume or forming loops. However, it is in the interest of analysis to generate fields which are relatively smooth on the scale of a few voxels.

Using the Talbot periods x_T, y_T and z_T with the definition of natural units from Chapter 2 for a speckle field, the volume resolution (X, Y, Z) can be set such that the vortex point densities are isotropic by:

$$X = Y = \frac{K_\sigma}{\delta k} \times \text{desired pixels}/\Lambda \quad (6.5)$$

$$Z = \frac{2K_\sigma^2}{\delta k^2} \times \text{desired pixels}/\Lambda. \quad (6.6)$$

For the field shown in Fig. 6.3, a possible resolution for the real space field could be $(X, Y, Z) = (498, 498, 3887)$. If the phase of the field (which allows the vortex points to be found) is stored by mapping the range $[-\pi, \pi]$ to integers in the range $[0, 255]$ then this resolution corresponds to roughly 1Gb of RAM. There are ways of reducing this by a factor eight but these details will not be discussed.

6.1.3 Vortex Sorting

The result of calculating a volume of phase and searching for vortex points is a sparse array of resolution (X, Y, Z) in which some elements are flagged as being vortex points. At the most basic level this could be a boolean array of TRUE and FALSE but as this occupies the same amount of RAM as an array of single byte integers it is usefull to store information about the topological charge of a vortex with the 27 possible vectors (s_{xy}, s_{yz}, s_{xz}) (with $s_{ij} = \pm 1, 0$) mapped to 27 different scalar values in the range $[0, 255]$ with a look-up table stored to retrieve the vector information.

Once the 3D array of vortex data has been created it must be searched and sorted into individual vortex structures. This is achieved using a simple method of searching the local surroundings of 'flagged' vortex elements. Taking the first non-zero element as a seed, a sub-array of size $3 \times 3 \times 3$ is extracted with the seed at the centre. The seed is flipped to being zero and

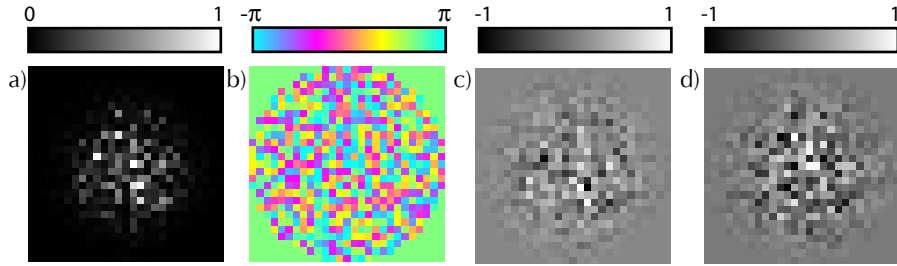


Figure 6.3: A typical 27×27 k -space power spectrum. a) Intensity, b) phase, c) real part and d) imaginary part of the spectrum. A circular aperture is applied to give a maximum k_r which removes the corners of the square array.

its information (position and charge vector) stored at the beginning of a list which will eventually store the sorted positions of the vortex line of which the seed was a part. The sub-array is now searched for another non-zero element which will become the new seed. This process continues until a seeding point is identified as being within one voxel of the original seed. At this point the entire length of vortex line, of which the original seed was a part, has been removed from the array and its information (a chronological list of seeds) stored in a list.

The effect of this process is to continually empty the main array of vortex positions and convert them into ordered lists. Once the array is empty the lists of sorted vortex positions are saved and a new field as generated. This allows many fields to be generated and the analysis done in one batch operation on all the resulting data files.

The following section discusses the results from this model using a speckle spectrum and vortex sorting.

6.2 Speckle fields

A good approximation for laser speckle spectrum is a k -space with gaussian randomly distributed real and imaginary parts with an overall gaussian en-

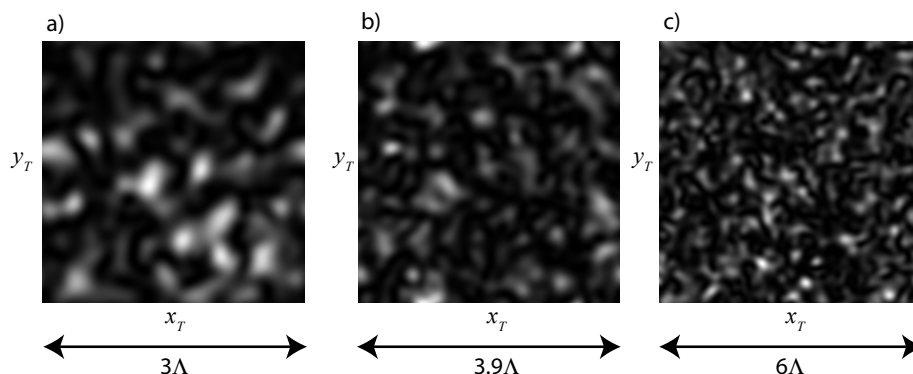


Figure 6.4: Cross sections of intensity in Talbot cells resulting from k -space grid sizes of (a) 21×21 , (b) 27×27 and (c) 41×41 .

velope of standard deviation K_σ centered around \mathbf{k}_0 . From chapter 2 the 2D vortex point density of such a field is $2\pi/\Lambda^2$ where Λ is the natural length scale.

Figure 6.3 shows a typical speckle spectra used with the model described in the previous section. In this example $K_\sigma = 0.15\Delta K \approx 4\delta k$. Example intensity cross-sections from various k -space sizes are displayed in Fig. 6.4.

Calculating the Talbot cell, on a $434 \times 434 \times 2609$ grid, of a field like that in Fig. 6.4(a) and sorting the vortex positions results in the flattened vortex structure shown in Fig. 6.5. In this figure the vortex lines have been coloured to show topology; white lines are vortex loops while red lines are periodic vortex lines. The topology is resolved by unwrapping the positions of each vortex line (as they are stored as modulus of the resolution of the Talbot cell) and querying whether the start position and end position are the same. A loop will return to the same spatial position while a periodic line ends in a different spatial position, some integer multiple of Talbot cells away. This simple check is carried out as each vortex line is found during the sorting of each Talbot cell as it aids further analysis to know quickly if a given structure is a loop or an infinite line.

Figure 6.5 was made using data from a k -space grid size of 21 — corresponding to $K_\sigma/\delta k \approx 3$ — as the aspect ratio of z_T/x_T allows the entire Talbot

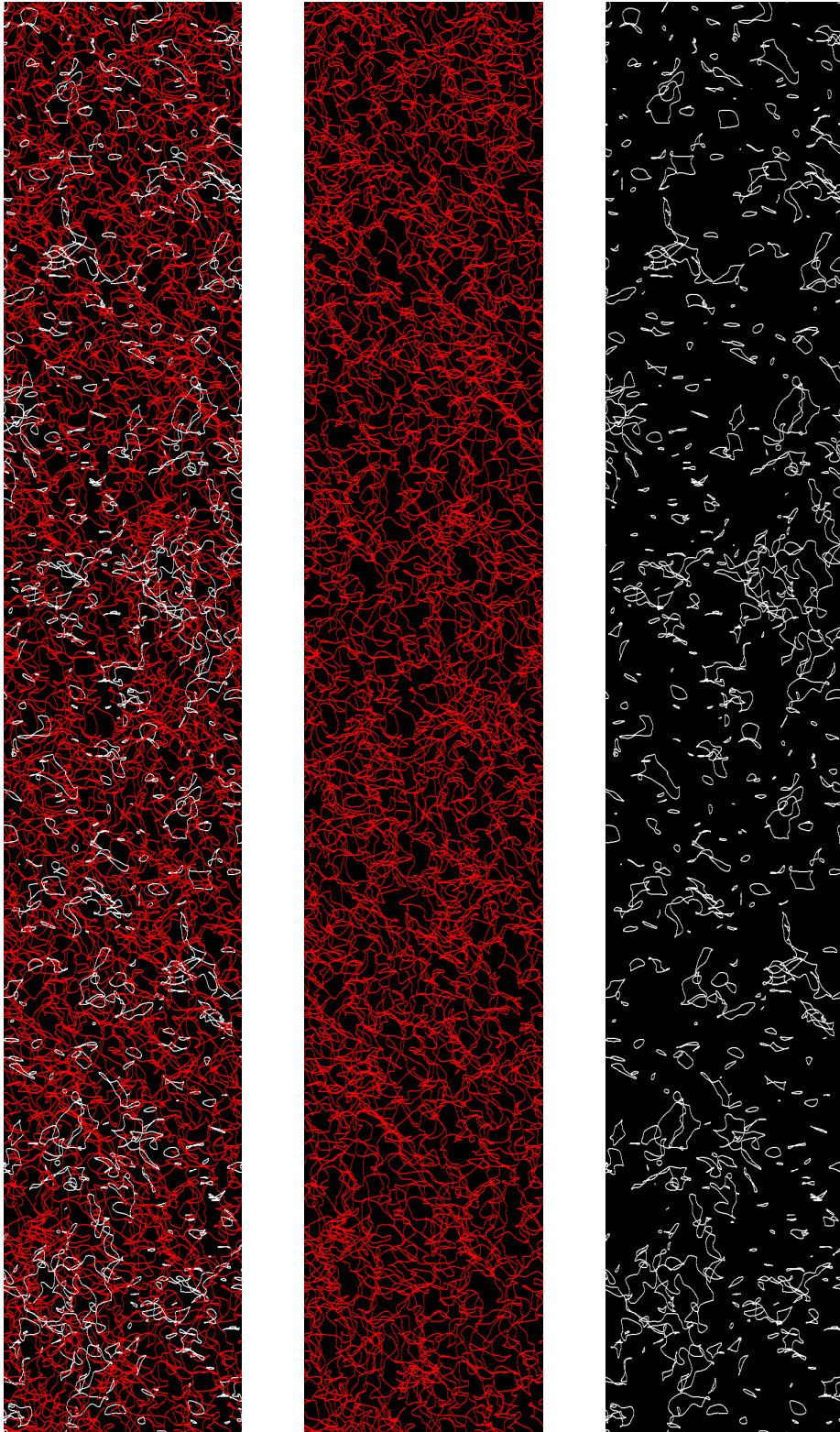


Figure 6.5: Vortex lines of an entire Talbot cell projected onto the xz plane. The entire z period is displayed vertically. Left most shows both loops (in white) and lines (in red) in the Talbot cell while the other projections show only the lines (middle) and loops (right). The volume of the cell is $162\Lambda^3$.

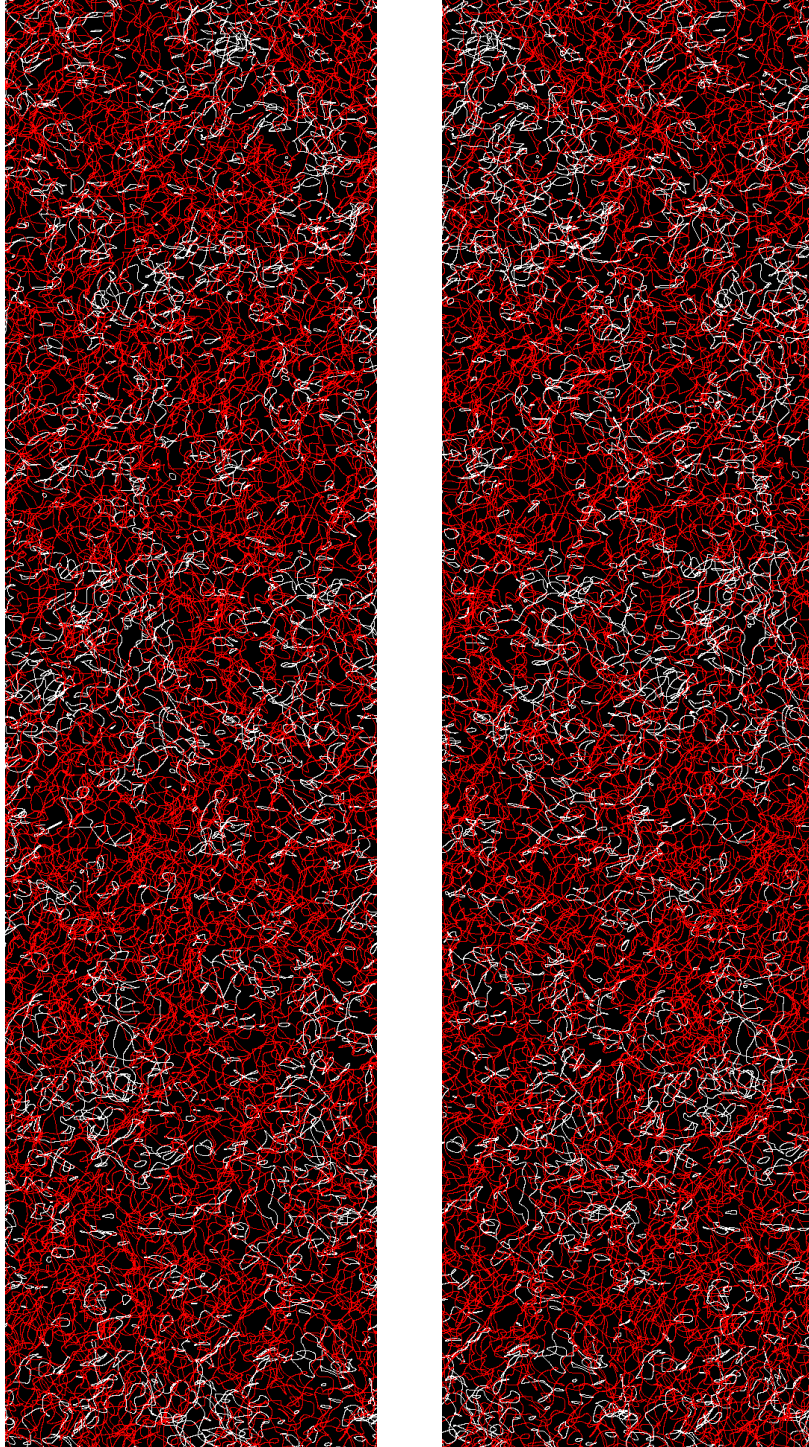


Figure 6.6: Vortex lines of a Talbot cell generated from a 27×27 k -space grid projected onto the xz plane, loops are shown in white and lines in red. The aspect ratio gives a cell volume of $3.9\Lambda \times 3.9\Lambda \times 30.4\Lambda \approx 462\Lambda^3$. The cell is split along the z axis (vertical) to display the entire cell in two section.

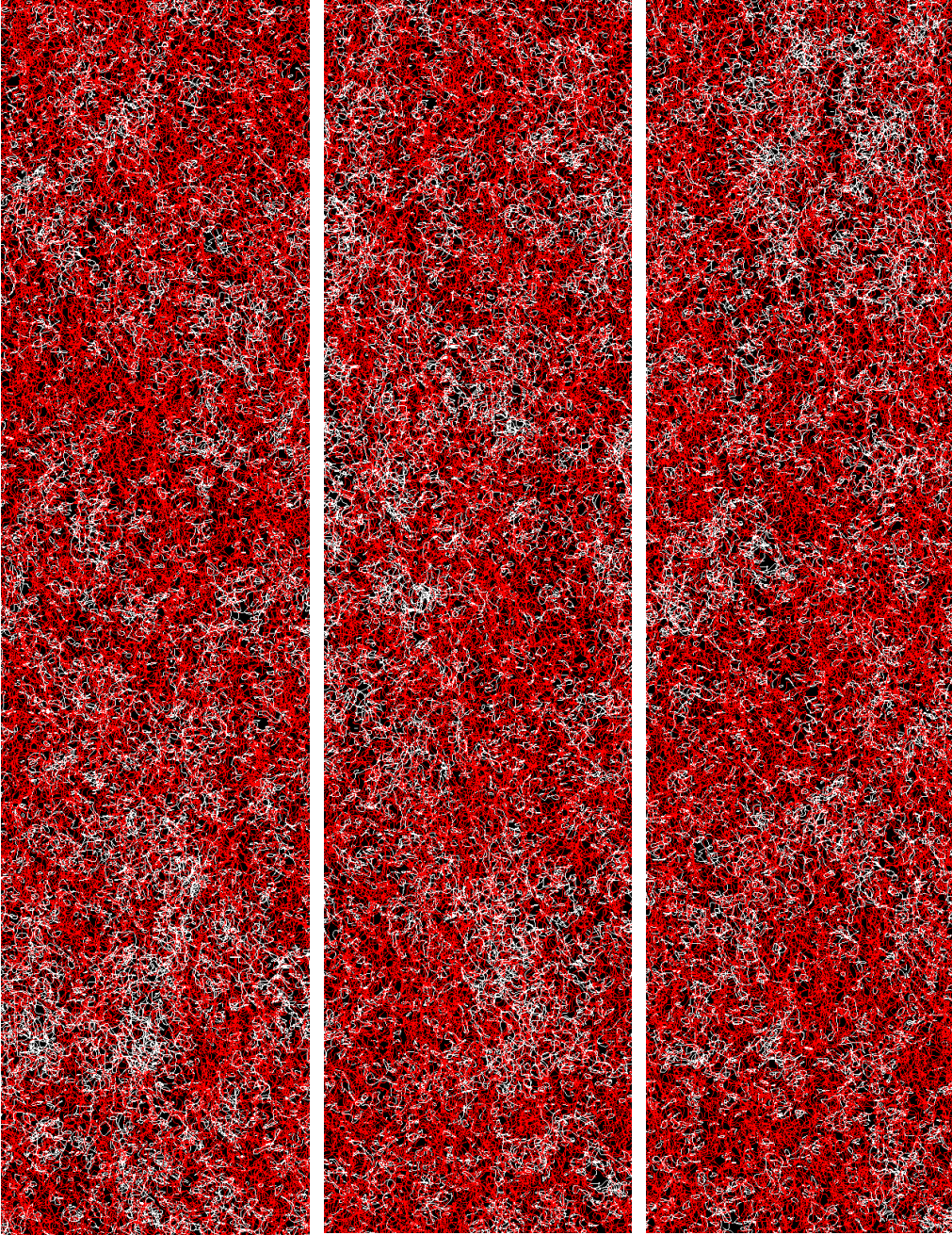


Figure 6.7: Vortex lines of a Talbot cell generated from a 41×41 k -space grid projected onto the xz plane, loops are shown in white and lines in red. The aspect ratio of the cell x_T/z_T is $1/12$ corresponding to a volume $6\Lambda \times 6\Lambda \times 72\Lambda = 2592\Lambda^3$. The cell is split along the z axis (vertical) to display the entire cell in three sections.

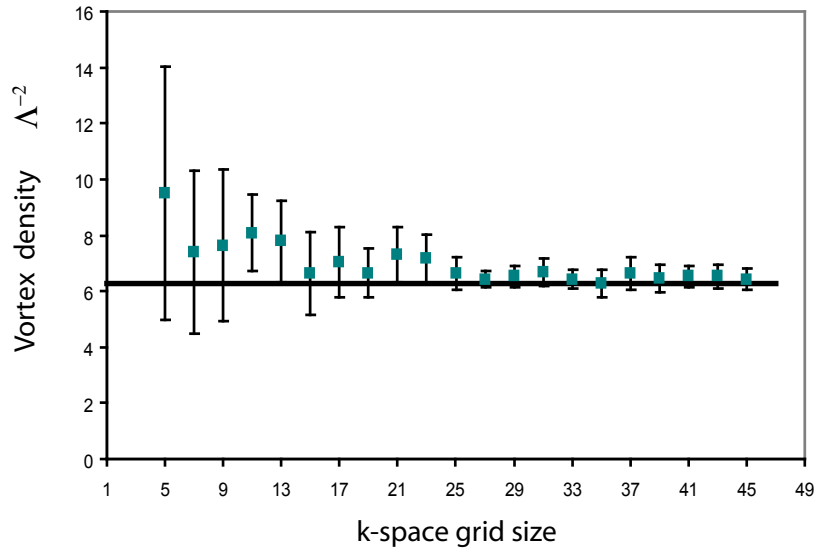


Figure 6.8: Vortex point density in the xy plane with increasing k -space grid size. The horizontal black line shows the theoretical prediction for a continuous k -space distribution with gaussian random waves and a gaussian profile.

cell to appear on an A4 page with reasonable detail. Vortex structures in Talbot cells from a 27×27 and a 41×41 k -space grid are shown in Figs 6.6 and 6.7 for comparison.

6.2.1 Model validation

A potential concern is that the periodic interference patterns resulting from a discrete and finite k -space may not be representative of those generated from a continuous distribution. For k -space grids larger than 23×23 the 2D statistics of vortex points converge on the theoretical values predicted for a continuous spectrum [Ber78] (see Fig. 6.8), furthermore the measured 3D statistics also converge to stable values (tables given in chapter 7). It seems reasonable to assume therefore that the interference patterns created from larger k -space grids are representative of the continuum. Consequently 27×27 k -space grids and larger are used and calculated over Talbot cells of

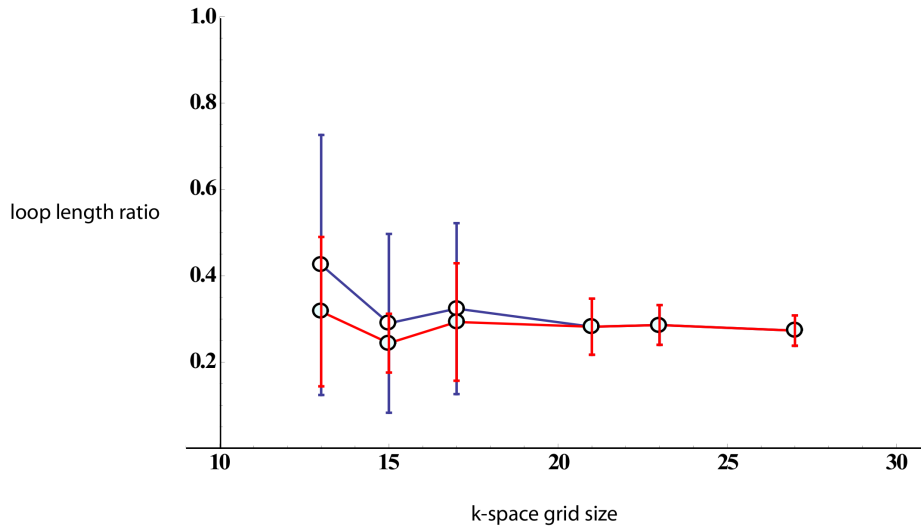


Figure 6.9: The ratio of total vortex loop length to total line length for different k -space sizes. For smaller k -space grids data points are shown (along blue line) for the mean which includes Talbot cells which were composed entirely of loops. This does not happen very often even for the small grid sizes, but does skew the mean considerably. This has not been observed for k -spaces larger than 17×17 .

resolution ($500 \times 500 \times 4000$) to ($800 \times 800 \times 10000$) voxels.

6.3 Speckle model results

6.3.1 Loop to line length ratio and percolation

A visually striking feature of the Talbot cells shown in Figs 6.5, 6.6 and 6.7 is the ratio of white to red. This ratio is the ratio of vortex loop length to vortex line length and for all but a few rare speckle Talbot cells (which have a low $K_\sigma/\delta k$) this number is quite low at 0.27 ± 0.03 for 27×27 k -spaces, where the error is the standard deviation between Talbot cells. On increasing k -space size, this number does not vary outside the error just quoted. Figure 6.9 shows the vortex length loop/line ratio as a function of

k -space size with error bars showing the standard deviation between Talbot cells. For small k -space sizes the variance is greater as the corresponding Talbot cells are of a smaller volume.

The ratio of 0.27 is similar to that numerically observed for random lattice models of $U(1)$ cosmic strings [VV84] in which the phase values on a 3D lattice are randomly chosen from three values (the minimum required for phase singularities to exist). The implication for real, non-periodic but finite extent fields, is that these lines would traverse the entire bright region of the field. Outside the predominantly ‘bright’ regions of the field, in large volumes of very low intensity, the field is dominated by background vacuum fluctuations [Ber04]. The time dependent nature of these fluctuations means that the field is not monochromatic in these regions and as such the vortex lines are no longer stationary structures. Reconnections are now very possible and the topology of the vortex lines becomes time dependent.

Every Talbot cell generated with k -space sizes larger than 17 contains an infinitely repeating vortex line that spans real space. This fact draws a connection with percolation on 3D lattices but into which of the many categories it fits is unclear. In percolation studies, sites or bonds on a lattice are ‘occupied’ with some probability p and there exists a critical probability p_c beyond which the lattice will be percolated. Whatever the connection between vortex lines in speckle fields and percolation, it is clear that the chosen system and parameters to model it with put the generated Talbot cells in a parameter space with $p > p_c$. Although measures such as p_c depend upon the specifics of the system in question, there exist universal exponents which appear in each system no matter the specific construction.

In the speckle model, the sites are occupied not directly randomly, but indirectly through the random choice of waves which superpose at each site. Another difference between percolation and what is being analysed here is the connectedness of vortex lines. As vortex lines cannot end in space, each ‘occupied’ site must be adjacent to two other others. This will result in correlations not present in most percolation studies. In any case, the pur-

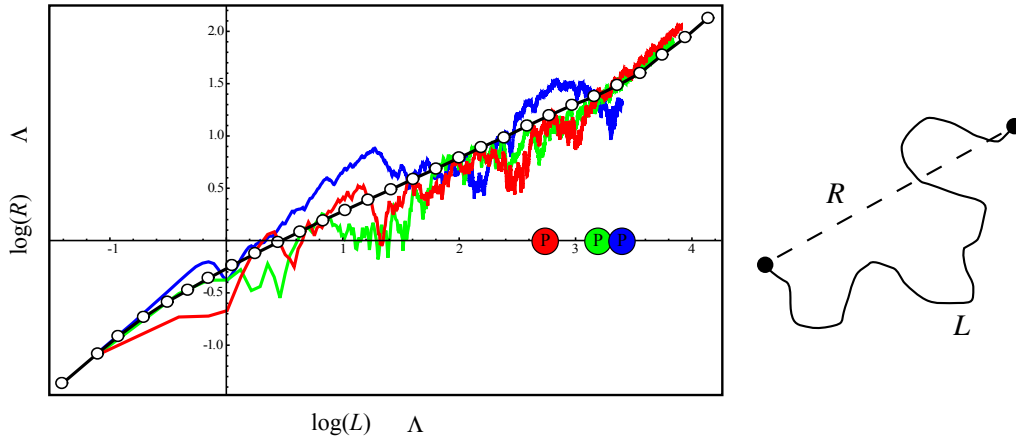


Figure 6.10: The Pythagorean distance between two points on three different vortex lines (in red, green and blue) as a function of vortex line length. The red, green and blue circles indicate the period of the correspondingly coloured lines. Black line shows the mean which is described more fully in Fig. 6.11.

pose here is not to phrase the results in the language of percolation but to draw ideas from a field which has created many tools for analysing random systems and their properties.

6.3.2 Fractality

Brownian behaviour of lines

An obvious measure to make when given a large sample of curves is the fractal dimension of the curves over the whole sample. For this measure, the infinite vortex lines were taken from 100 different Talbot cells generated with k -space grids of 27×27 , totalling an entire vortex length of $\approx 3 \times 10^5 \Lambda$. The fractal dimension was measured by plotting the log average straight line displacement, R , against log arc length, L , of vortex line for a large range of arc lengths.

Using this method and keeping one end of the arc fixed for an individual

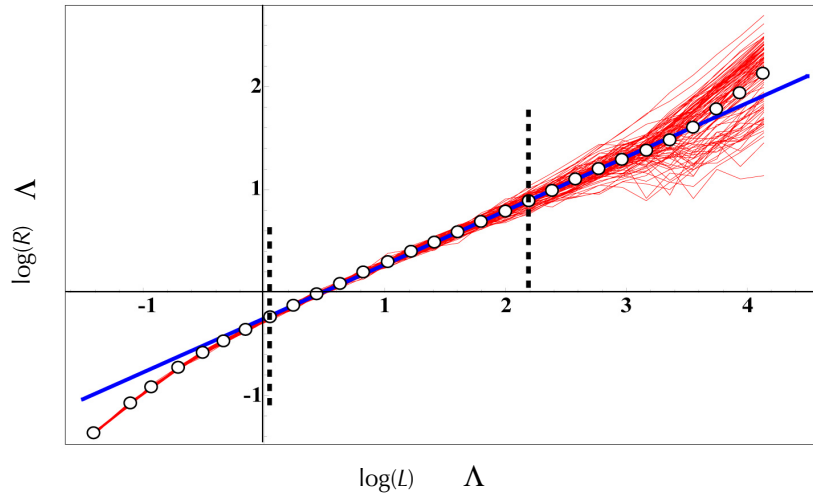


Figure 6.11: The Pythagorean distance between two points on an open vortex line as a function of vortex line length. Data is obtained from various speckle superpositions calculated using a k -space grid size of 27×27 in size. Circles mark the mean from 100 lines from different speckle superpositions and the straight line is the least square fit through the mean values. The faint red lines are the average values for individual lines. The gradient of ≈ 0.5 , fitted over the marked range, suggests a scale invariance over which the vortex lines have a Brownian random walk.

vortex line would result in a very rough and random looking plot (three examples can be seen in Fig. 6.10). To smooth the idiosyncrasies of individual lines, not only are the values averaged for 100 different lines, but each line has hundreds of different arc sections for each L chosen at random and averaged. Each mean point shown in Fig. 6.10 is the average over $\approx 10^4$ measurements.

The average Pythagorean length $\langle R \rangle$ between any two points on a line, separated by an arc of length L , is given by

$$\langle R \rangle = A^{1-n} L^n, \quad (6.7)$$

where A is a lengthscale below which the line is approximately straight. The reciprocal of n is the fractal dimension of the line [SAM93]: for a straight line, $n = 1$, and for a Brownian random walk, $n = 1/2$.

The inverse of the gradient of $\log(R)$ vs. $\log(L)$ is the fractal dimension of the curve, with a gradient of $1/2$ indicating a Brownian random walk. The straight line best fit shown in Fig. 6.11 has a gradient of 0.52 ± 0.01 which suggests that the vortex lines are indeed random walks over the two decades which the plot is near linear. The y -intercept indicates that $A = 0.5\Lambda$, comparable to the coherence length of the optical field. As expected, at lengthscales below A , the vortex lines are straight (the curve gradient converges on 1). The upper limit to this is a result of the periodicity of the constructed fields. On a large enough scale, periodic lines will approximate to straight lines like the small scale the gradient will converge to 1 on $\log(R)$ vs. $\log(L)$.

A gradient of 0.56 would have indicated a self-avoiding Brownian random walk, which seemed a possibility before finishing the analysis. The result of fully Brownian and not self-avoiding Brownian means that points (further apart than A) on vortex lines in speckle fields can come infinitely close to each other, there is no form of ‘repulsion’ between the lines caused by constraints to wave components in k -space — which is the source of the lengthscale A and limits small scales to straight line sections.

Figure 6.12 shows two sections of vortex lines from calculated speckle fields and two random walks generated from using a random number generator to walk 1000 steps on a 3D lattice.

Persistence length

When analysing curves and measuring fractality, a more specific indicator of how straight the lines are at small scales is the persistence length, P , of a curve. The persistence length of a curve of length, L , is defined as:

$$\langle \cos \theta \rangle = e^{-\frac{L}{P}} \quad (6.8)$$

where θ is the angle between the tangent of the curve at the origin to the tangent at a length L along the curve. The left hand side averages over all possible starting positions. Figure 6.13 shows the results of calculating the

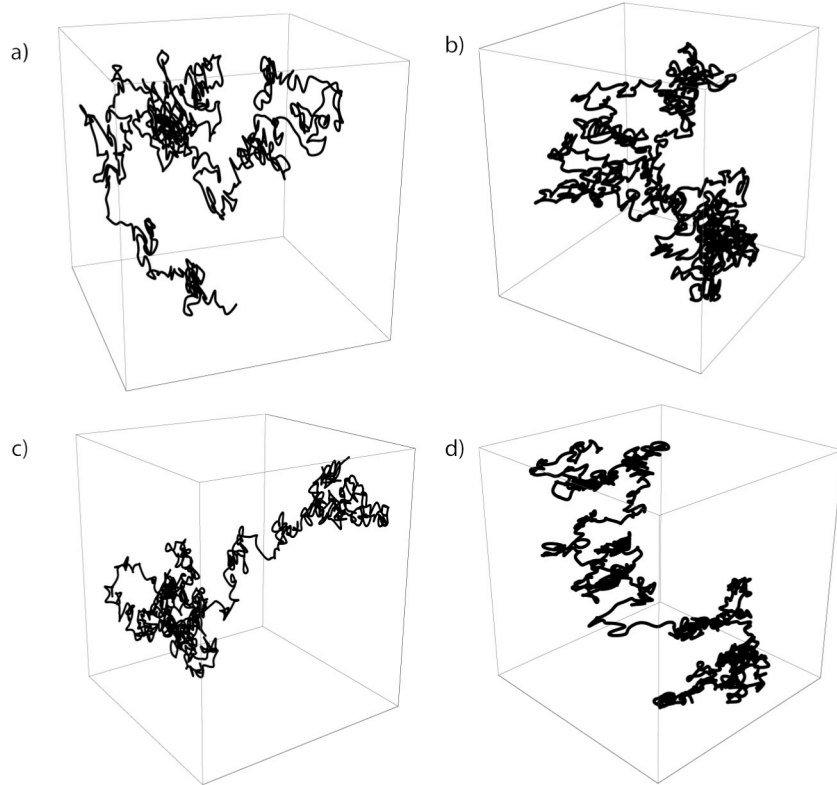


Figure 6.12: (a) and (b) show examples of vortex line sections of length $\approx 1000\Lambda$ from simulations, (c) and (d) show brownian random walks of 1000 steps.

$\langle \cos \theta \rangle$ by picking a vortex line and averaging the tangent correlations over 5000 different starting positions. This was repeated for nine other vortex lines and then results for all ten lines were averaged. The ten curves used were infinite periodic lines from simulations with $K_\sigma/\delta k = 4$. The resulting fit gives $P = 0.17\Lambda$.

Radius of gyration

A parameter which allows similar statements to be made about the vortex loops in speckle fields is the radius of gyration, R_g . This is the root mean square of the distance of points on a vortex line from its centre of mass —

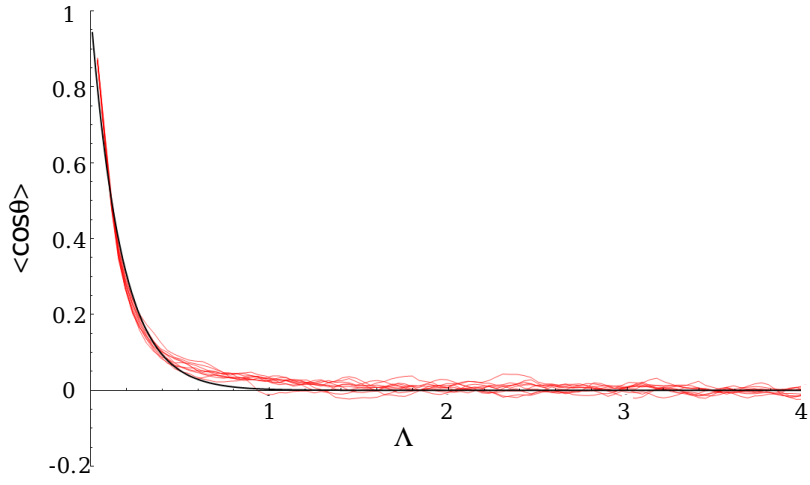


Figure 6.13: The exponential decay in angle, θ , between tangents as a function of length between points on a vortex line. Red lines show $\langle \cos \theta \rangle$ for 10 individual lines and the black line shows the fit $\exp(-L/P)$ where P is the persistence length. The fit gives $P = 1.7$.

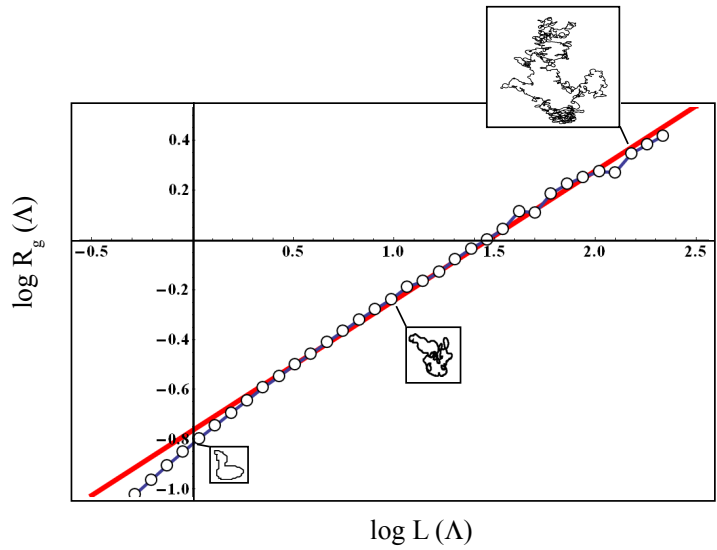


Figure 6.14: A loglog plot of the mean radius of gyration, R_g as a function of loop length, L . Three example loops are shown at different length scales for illustrative purposes. The red line shows a fit to the straight line section (0.2 – 2.0) on the $\log L$ scale and has a gradient of 0.52

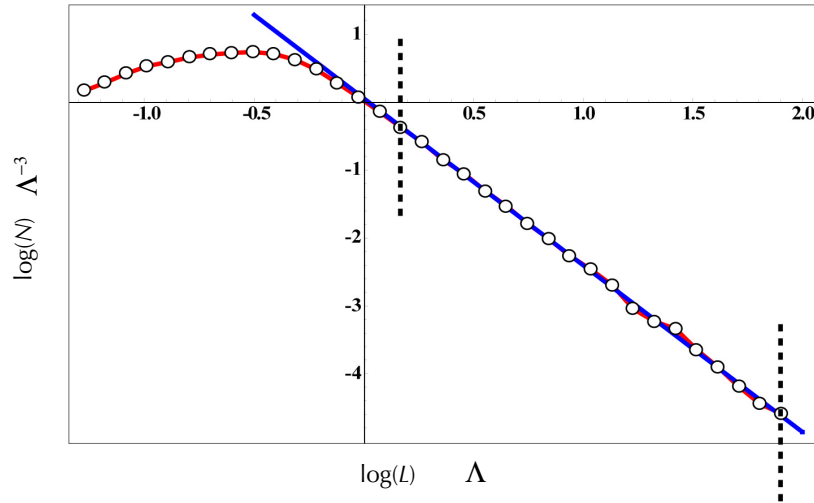


Figure 6.15: The observed length distribution of vortex loops within numerically calculated random speckle patterns. Data is obtained from various speckle superpositions calculated using a k -space grid size of 27×27 in size. Approximately 80,000 loops are included in this distribution. The average number of loops contained within the natural speckle volume is 3.9 and the most common loop length is readily contained within it. The number density of large loops decreases, over the marked range, with a gradient of ≈ -2.5 , consistent with Brownian scale invariance.

which is the average position in each axis ($\langle x \rangle, \langle y \rangle, \langle z \rangle$). For, circular, planar loops of length, L , the radius is simply $R_g = L/2\pi$. For more complicated loops R_g grows more slowly with L . These larger loops tend to be isotropic with no preferred plane. For these random Brownian loops $R_g \propto L^{1/2}$. Figure 6.14 shows the radius of gyration as a function of loop length.

The gradient of 0.52 ± 0.01 (fitted for $L > 1.5\Lambda$) again indicates a Brownian random walk, as would be expected from the fractal dimension analysis of the open vortex lines. The intercept of the curve connecting the mean values on this log log plot is at $L = 1\Lambda$ and $R_g = 0.16\Lambda$, close to the measured persistence length and is of a roughly circular loop.

6.3.3 Scale invariance

A concept which is very closely linked to fractality is scale invariance. A system which is scale invariant exhibits the same properties in the same densities at all scales. A strong indicator of scale invariance is a power law dependence. The universal exponents mentioned in the discussion of 3D percolation are concerned with the density of closed clusters — that is, in a 3D array of randomly connected bonds or sites, clusters of bonds/sites that are connected to each other but do not span the entire array.

Having discussed the infinite vortex lines in terms of percolation it is natural to consider the implication of scale invariance — for lengthscales significantly greater than P — on the size distribution of vortex loops (as studied for random lattice models of cosmic strings [VV84]). If the loop distribution is the same at all scales, then the number dN of closed loops per unit volume with sizes between R and $R+dR$, from equation 6.7 with Brownian exponent $n = 1/2$, is [VV84]

$$dN = CP^{-\frac{3}{2}}L^{-\frac{5}{2}}dL, \quad (6.9)$$

where C is a dimensionless numerical constant.

Figure 6.15 shows the loop length distribution from the simulations. The distribution has a peak in loop size of approximately $0.3\Lambda \approx 2P$, and suggests 3.9 loops per natural volume, both of which are consistent with figure 6.18 which shows example sets of speckle volumes from experiment. For larger loops, the gradient -2.46 ± 0.02 is consistent with equation 6.9, again supporting the observation that the vortex structures have a fractal self-similarity of Brownian character.

6.4 Experimental results

To complement the numerical simulations, vortex line topology in volumes of experimentally created laser speckle was measured. The speckle was generated by inserting a ground glass plate into a collimated HeNe ($\lambda = 633\text{nm}$)

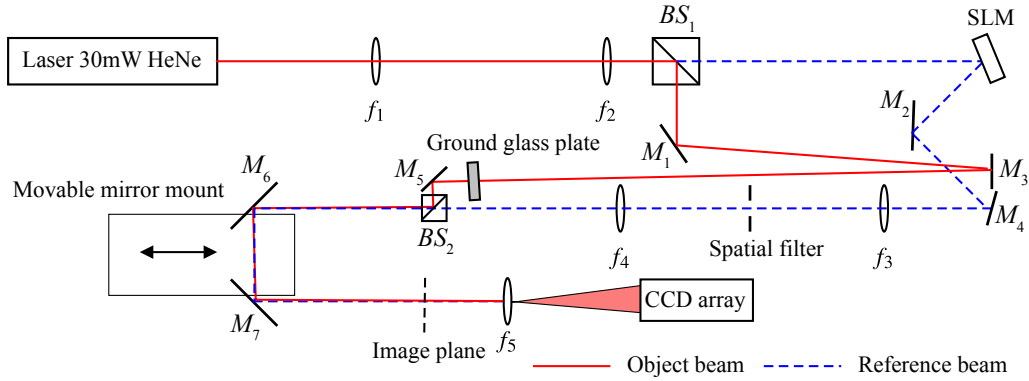


Figure 6.16: Experimental setup for intensity and phase acquisition of a speckle pattern. This apparatus is very similar to Fig. 3.1. The differences are that the first-order reflected beam from the SLM is now used as the reference beam and that the object and reference beams do not overlap until later in the apparatus. This last difference is due to the need for one beam to pass through a ground glass plate but not the other.

laser beam. The experiment apparatus was a modified version of that described in chapter 3 and can be seen in Fig. 6.16. The main modification was the insertion of the ground glass plate into one of the beam paths. In this particular setup, it was best to use the first-order diffracted beam from the SLM as a reference beam, the phase of which could be shifted by modifying a blazed diffraction grating.

In order to insert the ground glass plate, the beams had to deviate from each other by the radius of the plate so that the new reference beam (from the SLM) could propagate unaltered. A beam splitter was used to recombine the two beams. As the object beam was now a wide cone of speckle it was easy to choose a small section that the reference beam could be easily aligned with. Once a volume of speckle has been scanned a different speckle field may be created by simply rotating the ground glass plate. Interferometric measurements of intensity and phase in successive cross sections in this

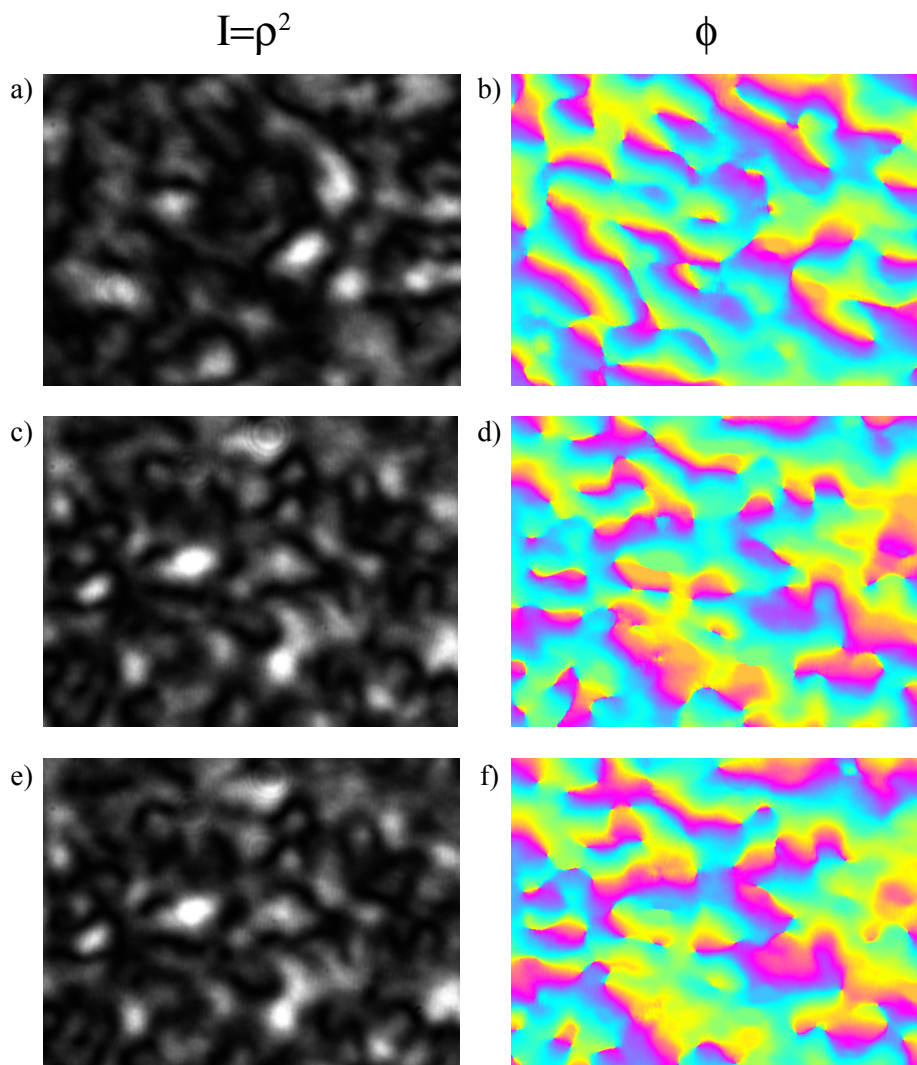


Figure 6.17: Cross-sections from three different speckle fields, (a), (c) and (e) show the intensity of the field normalised and mapped to grayscale while (b), (d) and (f) show the corresponding phase values in the usual colour-wheel mapping of the phase range $[-\pi, \pi]$.

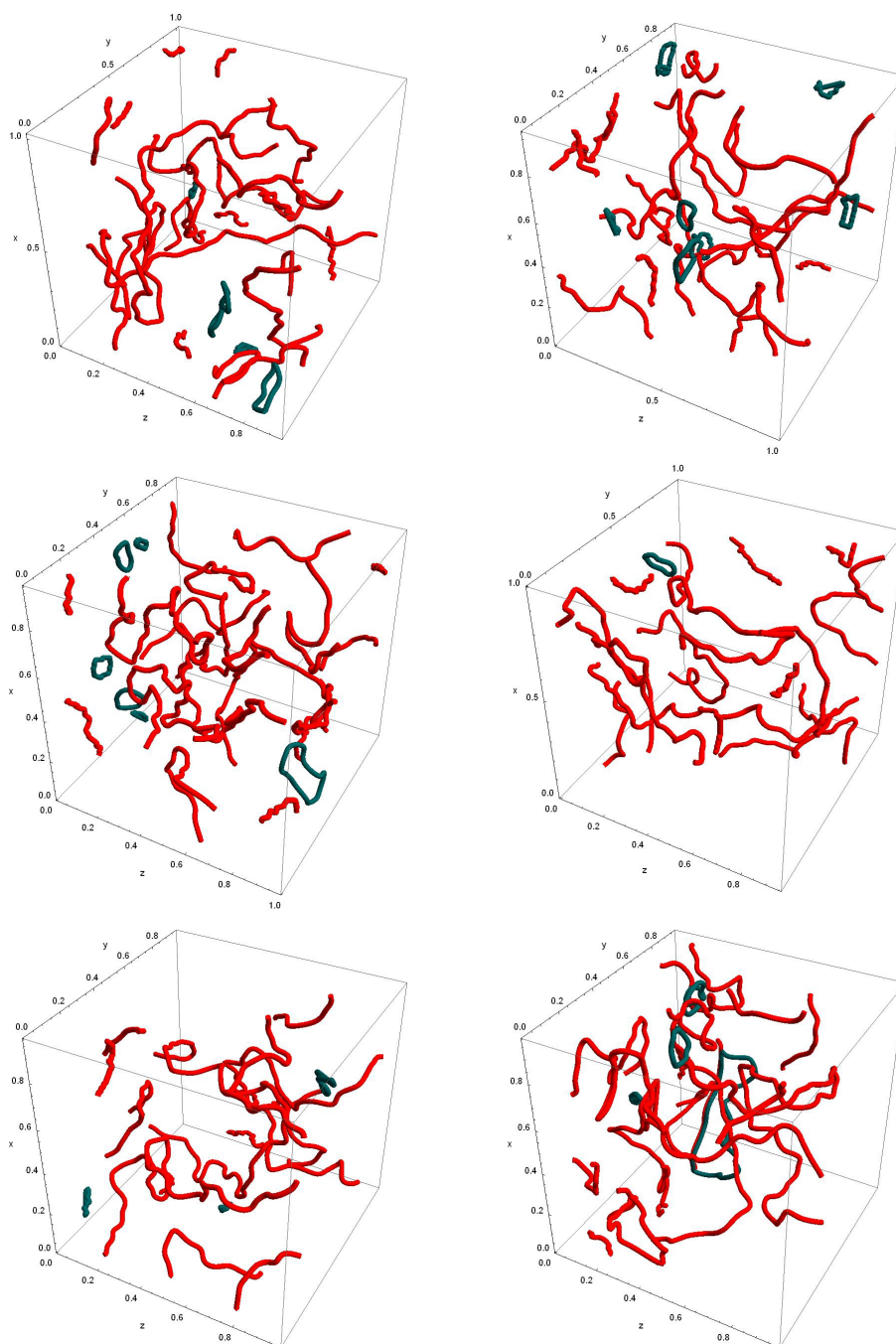


Figure 6.18: Six different volumes from experimental scans of a beam scattered from a ground glass plate. The open vortex lines are plotted in red and the closed loops in dark green. All are plotted over one natural volume of the speckle, Λ^3 .

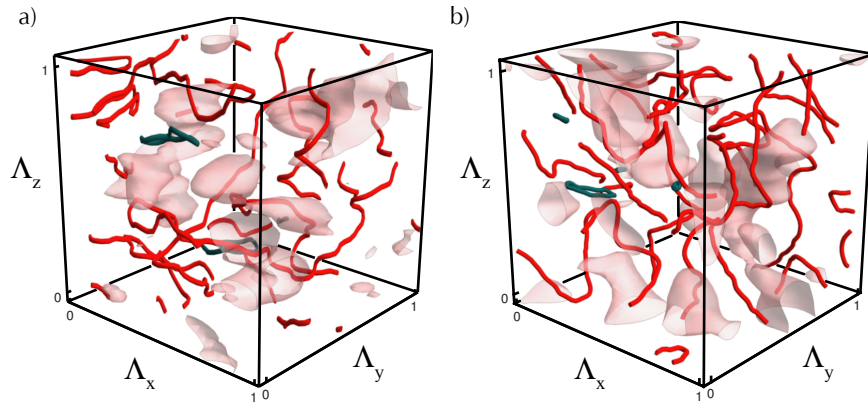


Figure 6.19: Vortex structure in speckle: (a) experimental vortex structure obtained through interferometric measurements of laser speckle from a ground glass screen and (b) numerical simulation of the vortex structure from Gaussian random wave superposition. The open vortex lines are plotted in red and the closed loops in dark green. Surfaces of 50% maximum intensity are also shown. Both are plotted over one natural volume of the speckle, Λ^3 . Although different in detail, the two patterns have similar characteristics.

experimental arrangement allows the three-dimensional vortex structure to be mapped using the techniques described in chapter 3. Figure 6.17 shows example cross-sections of experimentally observed speckle fields and figure 6.18 shows the measured and sorted vortex lines in unit volumes, Λ^3 , of such fields.

In order to locate the vortex positions precisely, the measured field is subject to a small 3D Gaussian filter (of size $3 \times 3 \times 3$ voxels). The phase alone cannot be smoothed as it contains numerical discontinuities between $-\pi$ and π . The measured values of intensity, $I = \rho^2$, and phase, ϕ are combined to create the complex field, $\psi = \rho \exp i\phi$ that will be filtered. The vortex finding and sorting begins once the phase is extracted from the smoothed complex data.

As the field of view of the experimental data is limited by the size of detector array, the topology of vortex lines that terminate at the sides of the measured volume cannot be distinguished. Consequently, the possible statistical

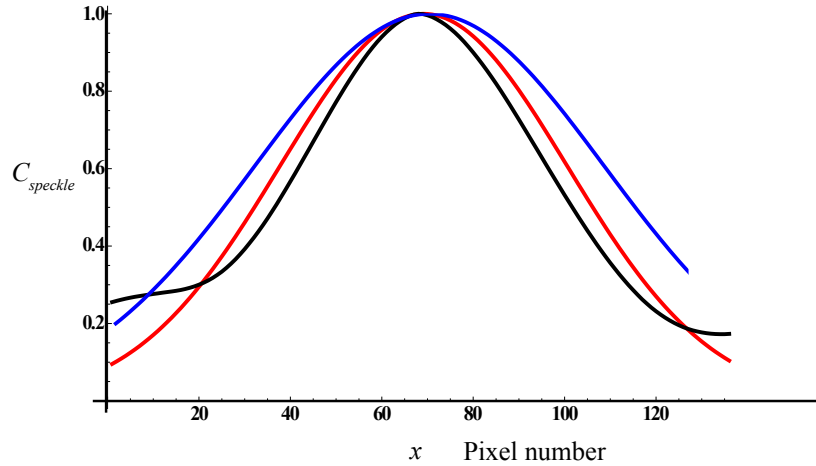


Figure 6.20: The correlation of the complex field with the conjugate of itself over $R = x$. The black line shows the experimental result at $z = 0$ with the red line showing a Gaussian fit. The fit results in an estimation of $\Lambda \approx 194$ pixels ($\approx 80\mu\text{m}$). The blue line shows the corresponding fit at $z \approx \Lambda_z$, resulting in $\Lambda \approx 239$ pixels. It is clear that the numerical aperture varies slightly over the scan range.

comparisons between the experimental and numerical data are limited. Figure 6.19 shows a volume of experimentally measured vortex lines in speckle alongside a numerically generated volume of similar size. Simple inspection of this figure and other sets of data suggests that the simulated vortex structure is indeed similar to that of experimental observations.

Taking the large data sets that were used to conduct the fractal and topology analysis and extracting hundreds of different unit Λ^3 volumes, allows the numerical data to be treated exactly as the experimental data, with only fully contained loops being counted as loops. Figure 6.19 (b) shows one such calculated volume. The number of loops wholly contained within one Λ^3 averaged over 600 extracted volumes is subject to Poissonian statistics (as is the experimental data). The mean number of loops was found to be $2.6 \pm 1.6\Lambda^{-3}$, as opposed to $3.9\Lambda^{-3}$ when the topology of all lines in the entire field is known.

To make the same measurements for the experimentally measured volumes a

method is required for measuring Λ . The most straightforward method, and the method implemented, was the use of the autocorrelation of the speckle field:

$$C_{speckle} = \exp(-K_\sigma^2 R^2/2) = \exp(-2\pi R^2/\Lambda^2). \quad (6.10)$$

By acquiring a plane of full complex data and fitting a Gaussian distribution to $C_{speckle}$, Λ can be estimated. $C_{speckle}$ is measured experimentally by calculating the magnitude of the correlation of the field with the conjugate of itself. Figure 6.20 shows a 1D slice through $C_{speckle}$ measured at two different planes and shows two Gaussian fits, one for each plane.

It is clear from the two Gaussian fits, at $z = 0$ and $z \approx \Lambda_z$, that Λ is increasing across the scan-range of the camera. However, as the number of independent experimental runs was limited, it is difficult to rescale each plane independently as a function of z . $C_{speckle}$ was averaged over all planes measured and the resulting value of Λ used for plotting all results (some of which can be seen in Fig. 6.18). From the ten experiments run (each containing $\approx 8\Lambda^3$), Λ_{xy} was measured to be $90 \pm 11\mu\text{m}$.

Separating the entire measured volume into unit of Λ^3 and counting the number of loops contained within the volumes resulted in the Poisson distribution shown in Fig. 6.21. The average number of loops contained in a unit volume was measured to be 2.0 ± 1.5 (averaged over 70 natural volumes). The discrepancy in the values obtained from simulated speckle fields and real speckle fields may lie in the measurement of Λ . An error in Λ of 10% would result in a volumetric error of about 30%.

6.5 Discussion

The results for the large-scale structure of the vortex lines and the size distribution of vortex loops support the hypothesis that vortex lines in speckle fields have scale invariant structure. The lines are approximately Brownian with fractal dimension of about 2. This Brownian behaviour is also observed in simulations of some types of cosmic string [AEVV86]. However, it is not

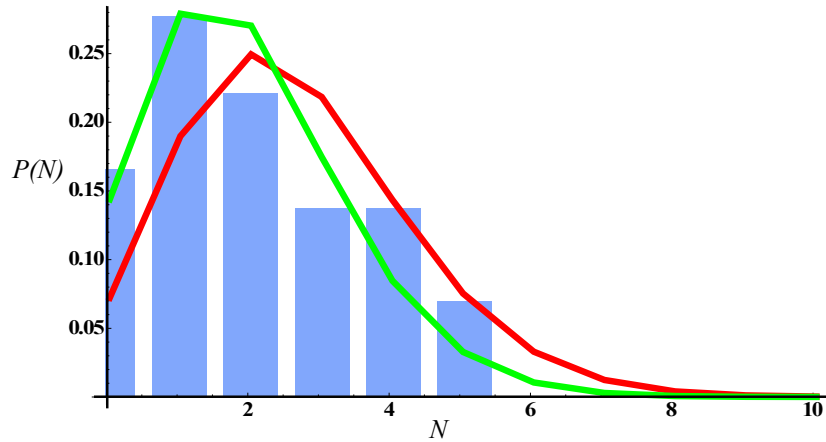


Figure 6.21: Poisson distributions for the probability of a number of loops, N , appearing in a box of size Λ^3 (only counting loops fully contained within box). Red line shows fit to numerical data collected from 600 different samples and the green line shows a fit to experimental data from 70 samples (real experiment values shown as bars). For numerical experiments $\langle N \rangle = 2.6$ and for real experiment $\langle N \rangle = 2.0$

shared by other vortex systems, particularly superfluids, for which the details, including the fractal dimension of the vortex tangle [KBS01] and the distribution of the loop length [MT06] depend on nonlinear dynamics.

It is worth emphasising here that the optical fields considered in this chapter are both linear and monochromatic, so there are no energetic considerations, and the statistics depend only on the probability distribution of the superposed random waves. The findings may be compared with those of reference [BS02], in which nodal domains in random real two-dimensional wave superpositions were empirically found to be in the class of two-dimensional percolation. A closer analogy for these vortex systems may be optical interference in a nonlinear medium, which would give an energy cost associated with vortex line curvature. Further investigation will reveal what other geometric properties of tangled vortex lines in three-dimensional random fields are universal, and whether any properties are system-specific.

Vortex topology in random fields

This chapter will explore the topology of vortex lines generated by the model described in chapter 6. First, the methods used to extract topological information will be described and then results given. The notation in the following sections uses lowercase bold letters to denote continuous or discrete lists of (x, y, z) vectors and capital bold letters to denote the projection of such curves onto a plane.

7.1 Links and threadings

To find two closed curves \mathbf{a} and \mathbf{b} that are linked, the linking number must be calculated. This is achieved by projecting the two curves onto a plane, making \mathbf{A} and \mathbf{B} , and then following one of the curves, noting the sign of the ‘over’ crossings as the line is traversed. The summation of these particular signed crossings gives the linking number. The most simple link is the Hopf link which has linking number ± 1 .

With regards to numerical and experimental data there are a few steps

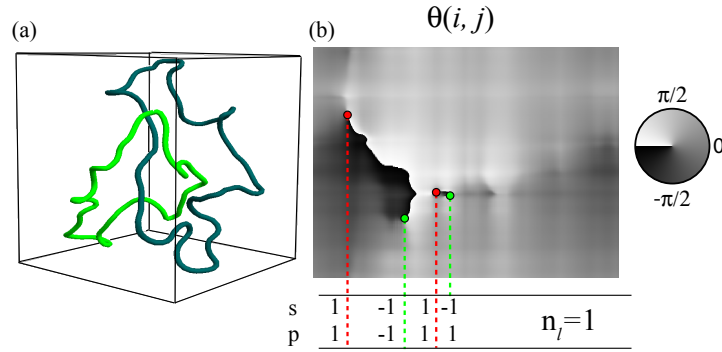


Figure 7.1: A vortex link is shown in (a) with the corresponding chord plot of the xy projection of the link shown in (b). The calculation of the linking number, n_l is also illustrated.

required to get to the linking number. The first is to identify pairs of loops which are close enough to each other to be regarded as potential links. This is done by checking the extreme values of x , y and z of one loop and determining whether or not they invade the bounding box of the other loop. The next step is to identify the crossing points in the xy plane (other planes could be used and would ultimately lead to the same answers).

7.1.1 Identifying crossing points

The method developed for finding crossing points is novel in that it uses singularities of the chord angles between the two curves. Plots of chord angles (such as Fig. 7.1) can be made by evaluating

$$\theta(i, j) = \arctan \left[\frac{(\mathbf{b}(i) - \mathbf{a}(j)) \cdot \hat{y}}{(\mathbf{b}(i) - \mathbf{a}(j)) \cdot \hat{x}} \right], \quad (7.1)$$

over all possible combinations of i and j — which are points along the lengths of the curves..

The singularities in the chord angle plot are clearly visible and are the distinctive markers of crossing points between the two curves. This is understood by fixing one end of a chord at a crossing point $\mathbf{A}(X)$ and moving

the other end of the chord along $\mathbf{B}(i)$. As the point on \mathbf{B} approaches the crossing point the chord shrinks and as it passes the crossing point the chord flips by π . At the crossing point the chord length is zero and its angle is undefined.

Using the same method for finding phase singularities (described in chapter 3) the crossing points can be located. The sign of the chord singularity is also useful. The multiplication of the topological charge of the chord singularity with the sign of the z component of the full 3D chord, $p = \text{sign} [(\mathbf{b}(i) - \mathbf{a}(j)) \cdot \hat{z}]$, gives the sign of the crossing. The sign is defined with a right hand rule following the direction of the curve (increasing i or j).

The linking number, n_l , of two curves is given by [Rol03]:

$$n_l = \frac{1}{2} \sum_{n=1}^N s_n p_n, \quad (7.2)$$

where N is the total number of crossings, s_n is the topological charge of the n^{th} crossing and p_n (defined in the previous paragraph) is the over/under sign of the n^{th} crossing.

7.1.2 Links in speckle

As discussed in the introduction to this thesis optical singularities can exist in more complex topologies than just loops and lines — such as links and knots. However, these vortex knots and links have only been constructed, theoretically and experimentally, with very particular weightings of Laguerre-Gauss or Bessel modes. The question still stood as to whether or not these types of topologies could exist in generic wavefields. This question has been answered to some extent empirically by the observation of linked vortex lines in the model described in the previous chapter. Several data sets were generated using various sizes of k -space grids. These sets were then searched for links using the method described in the previous section.

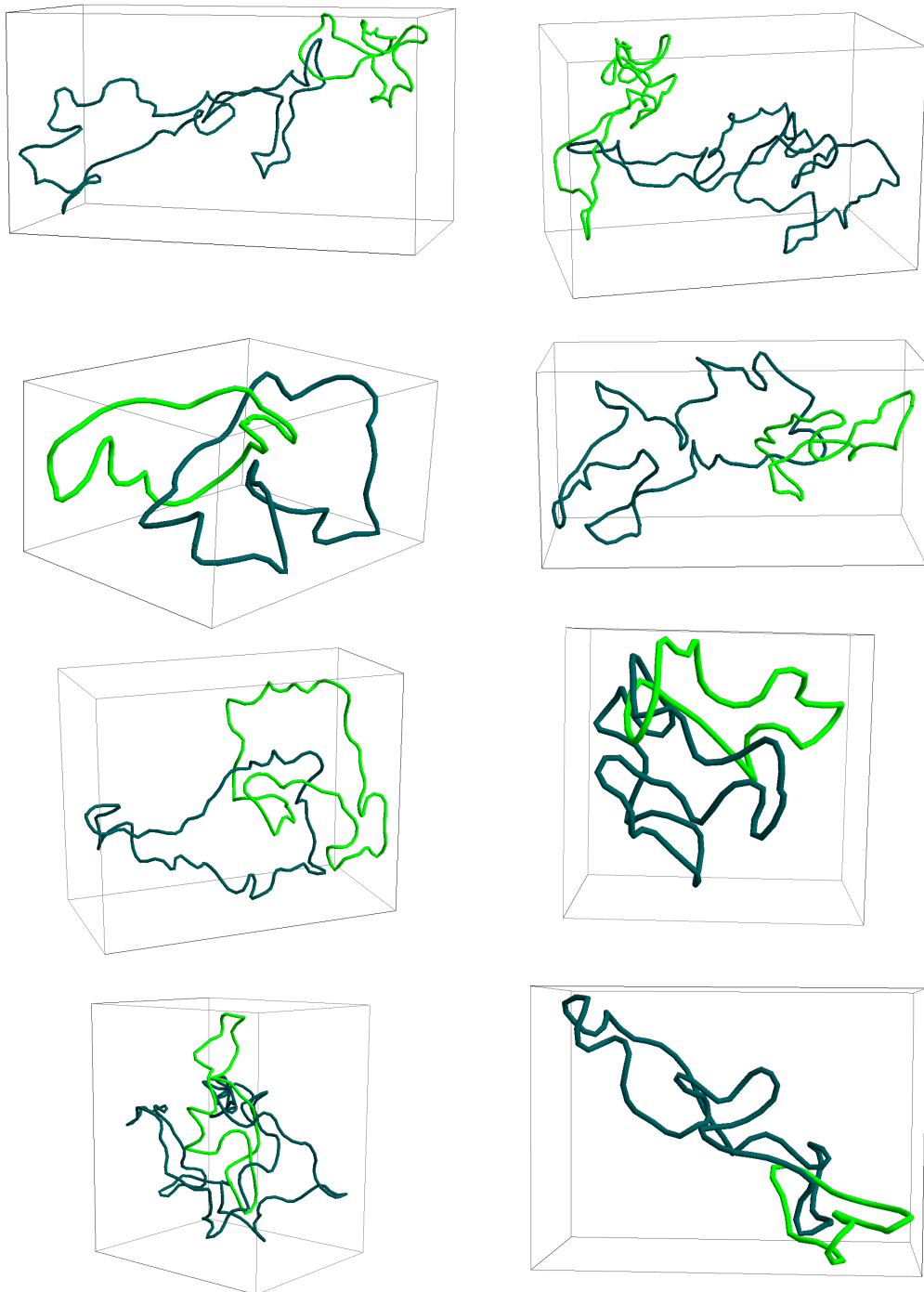


Figure 7.2: Linked vortex lines found in random fields with k -space grid size of 41×41 .

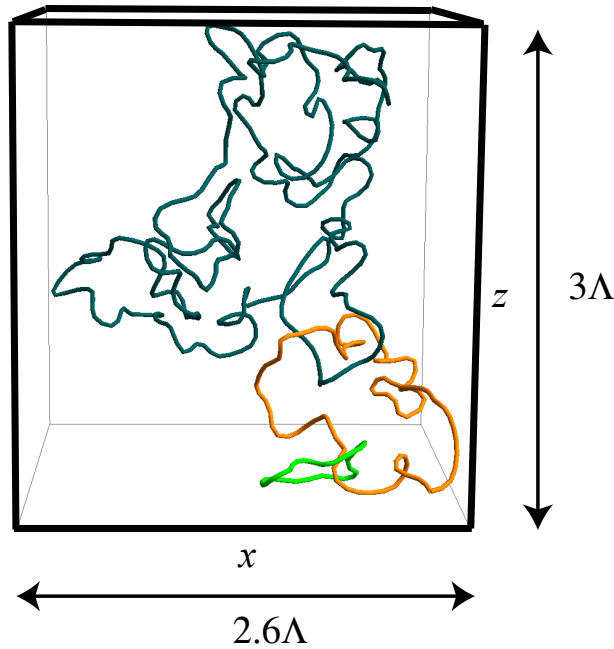


Figure 7.3: One of the three-component ‘chain’ links found in the generated data.

Combining the number of linked loops of length L with the total number of loops of length L allows the probability of a loop *not* being linked to be estimated. As with the unknot probability observed in polymer literature [OW07] an exponential decay was fitted to the unlinking probability and is given in the results section below.

7.1.3 Threadings in speckle

Threadings are identified in the same way as links are. The difference being that one of the curves is not closed. This time when identifying candidates, the long periodic lines (which account for $\approx 73\%$ of the vortex line length in speckle fields) are scanned along their length, flagging sections that invade the bounding boxes of vortex loops. The sections of line that are identified as approaching vortex loops are extracted from the full list of positions and Eqn. 7.2 is evaluated for the line subsection and the full loop.

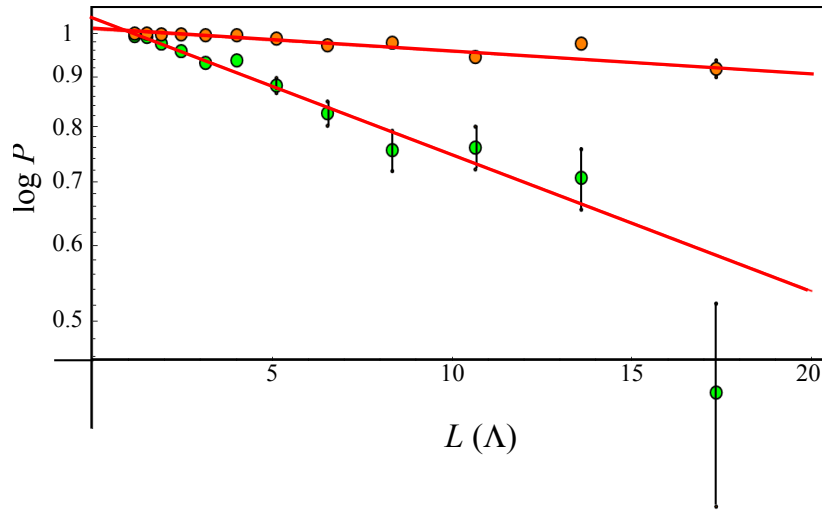


Figure 7.4: The probability of a vortex loop being unthreaded. Orange points show data points for probability of loops *not* being threaded by other loops and the green points show the overall probability of being unthreaded.

7.1.4 Results

Figure 7.4 shows the probability of loops of length L being unthreaded. This measure includes both loops threaded by other loops (forming a link) and loops threaded by lines. The probability of a loop being unthreaded was found to be a decaying exponential of the form

$$P_{unthread} \sim e^{-L/T}. \quad (7.3)$$

where $T \approx 30$ for total unthreading probability and $T \approx 185$ when restricted to loops threaded by other loops (links).

The collected data corresponds to various values of $K_\sigma/\delta k$ from 3 to 6 gives a total volume of simulated speckle field of $\approx 1.4 \times 10^5 \Lambda^3$. Generating this data took approximately 3000 hours of CPU time on a cluster of P4 processors operating at 3GHz. Within this total volume, unthreaded loops, loops threaded by periodic lines and loops linked to other loops have been identified. Figure 7.4 was generated from approximately 350 links and 2800 threadings.

These results appear to be stable with respect to $K_\sigma/\delta k$. This suggests a limited effect of the periodic boundary conditions. The largest k -space grids (41×41) corresponds to a Talbot distance of $x_T = 6\Lambda_{x,y}$ and $z_T = 72\Lambda_z$, meaning that the vast majority of loops are contained within a single Talbot cell, again suggesting that the periodicity is unlikely to be a perturbing factor in the statistical topology.

The number of candidate loop pairs that could be linked, and the number of links actually identified are both comparatively small in number but again show no sign of significant variation across the sizes of k -space. Only four links more complex than the Hopf link have been found — three three-component links (one of which which can be seen in Fig. 7.3) and one link of linking number 2. However, the survey of overlapping loops does not search for links whose net linking number is zero, such as the Whitehead link or Borromean rings [Rol03].

7.2 Knots

The method used to search for knots extends that used to find links. The chord angle plot defined by Eqn. 7.1 is replaced by:

$$\theta(i, j) = \arctan \left[\frac{(\mathbf{a}(i) - \mathbf{a}(j)) \cdot \hat{\mathbf{y}}}{(\mathbf{a}(i) - \mathbf{a}(j)) \cdot \hat{\mathbf{x}}} \right]. \quad (7.4)$$

This has the effect of identifying self crossings and introduces a diagonal symmetry where $i = j$ (here the end-points of the chords are the same point) introducing a π jump in θ . The symmetry results in each crossing being identified twice; once as the line being followed is the over-crossing section and once as it becomes the undercrossing section. An example of a chord plot using just one curve is shown in Fig. 7.6.

7.2.1 Alexander polynomials

The method of identifying links is simpler than that required for knots. Link identification requires the addition of signed crossings — knot identification requires the calculation of a knot invariant, the simplest of which is the Alexander polynomial.

The Alexander polynomial was identified as being a knot invariant in 1928 [Ale28]. Since this discovery the Alexander polynomial has been superseded by various other polynomial invariants such as the Jones polynomials [Jon85] and the more powerful HOMFLY polynomial [FYH⁺85]. Although it is not the most robust polynomial invariant it will uniquely distinguish knots with fewer than nine crossings. This is more than adequate for the purposes of searching vortex data for knots.

The Alexander polynomial can be calculated by creating a $N \times N$ matrix, where N is the number of crossings in a chosen projection. The rows correspond to the crossings and the columns correspond to the arc sections which the crossings divide the projection into (arcs begin and end at an under crossing). In this matrix a positive crossing has entries $(1 - t)$ for the over crossing arc, -1 for the incoming arc and t for the outgoing arc. A negative crossing has entries $(1 - 1/t)$ for the over, -1 for the incoming and $1/t$ for the outgoing arcs [OW07]. Taking any principle minor of this matrix and calculating the determinant results in the Alexander polynomial of the curve (up to a factor of $\pm t$).

As chord plots for single curves have many more crossing points than those for two curves, one needs to be careful in constructing the matrix described above. A problem that is encountered frequently for curves sampled onto a grid is that of multiple crossings — crossings who share the same values of i or j . To construct the matrix described above, each crossing point must exist with its own values of i and j , as degeneracy leads to a number of arc-sections less than N making it impossible to calculate the Alexander polynomial. This is clear from Fig. 7.5 where the projected curve, known

as a planar diagram, with a multiple crossings only has 5 arc-sections has fewer arc-sections than crossings

7.2.2 Multiple crossings

This problem is solved by identifying the multiple crossings and modifying their position in (i, j) whilst respecting the topology of the curve. This manipulation is performed by checking the z values of the crossing points and moving the most extreme (i.e. the ‘highest’ or ‘lowest’ z value) onto an adjacent unoccupied (i, j) position. For multiple crossings of more than two this process is iterated until each crossing has its own unique (i, j) coordinate. This process is illustrated in Fig. 7.5 where three arcs cross at the same point, creating a multiple crossing; these are manipulated, resulting in three individual crossing points. Note in the diagram that the number of crossings in the chord angle plot is the same before and after, it is the number of arc-sections that increases. Without resolving the multiple crossings it would not be possible to construct the $N \times N$ matrix required for evaluation of the Alexander polynomial.

7.3 Test curves

In order to test the algorithm, a trefoil knot was generated numerically from the following parameterisation:

$$\begin{aligned} x &= 3 \sin(2u) - 2 \cos(u) \\ y &= 2 \sin(u) - 3 \cos(2u) \\ z &= 2 \cos(3u). \end{aligned} \tag{7.5}$$

Figure 7.6 shows this curve and the corresponding chord angle plot, $\theta(i, j)$. Also shown are the resulting matrices for determining the Alexander polynomial using the methods described above.

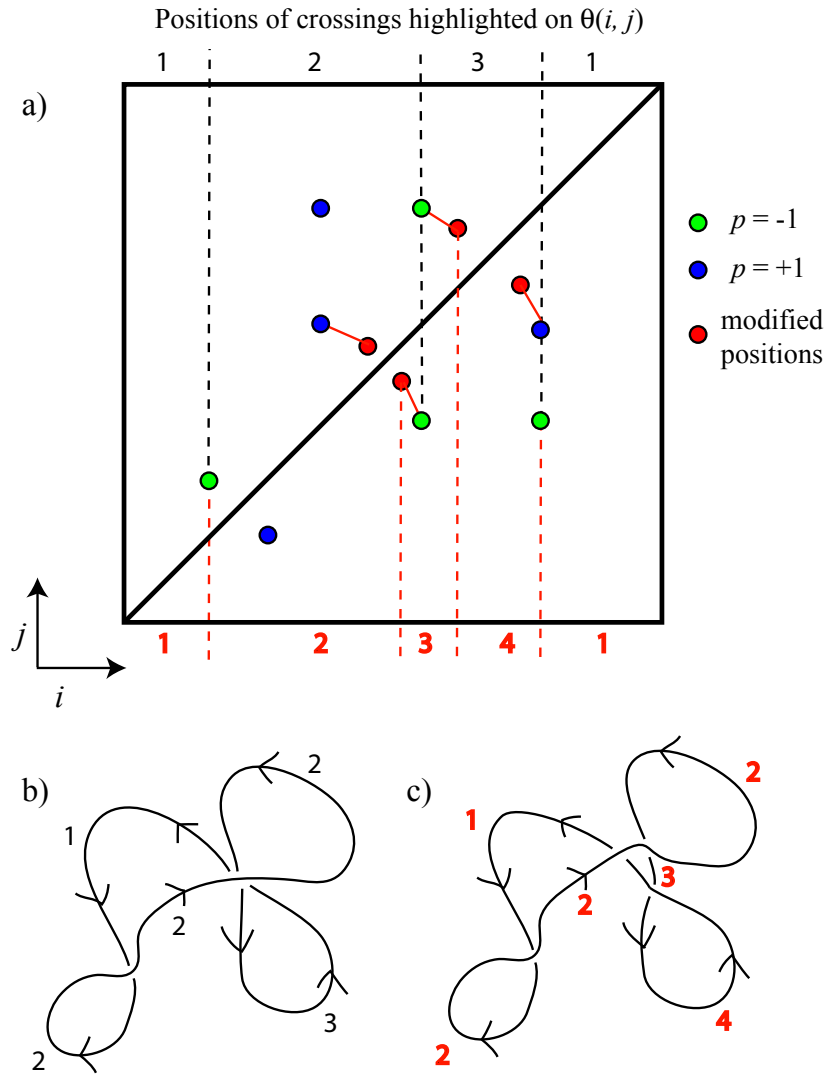


Figure 7.5: a) Positions of crossings highlighted on $\theta(i, j)$ plane for the curve shown in (b). The blue and green spots are $p = +1$ and $p = -1$ crossings. The red spots in (a) indicate the modified positions of crossings which resolves the multiple crossing and results in the curve drawn in (c). Note it is $p = -1$ crossings which divide the curve into arc-sections.

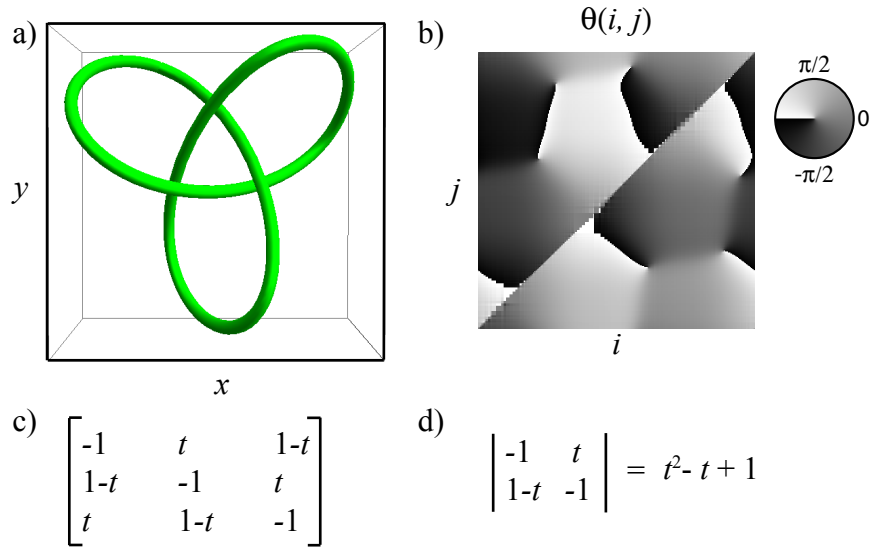


Figure 7.6: a) A prime trefoil knot and (b) the corresponding chord angle plot of the xy projection of the knot. The resulting matrix used to calculate the Alexander polynomial is shown in (c). The Alexander polynomial is the determinant of any principle minor of this matrix. One such principle minor is shown in (d).

A figure eight knot was also generated. The points used were calculated from the following parameterisation:

$$\begin{aligned} x &= \cos(3u)(2 + \cos(2u)) \\ y &= \sin(3u)(2 + \cos(2u)) \\ z &= \sin(4u). \end{aligned} \tag{7.6}$$

Figure 7.7 shows the test figure eight curve and the corresponding chord angle plot, $\theta(i, j)$. Also shown are the resulting matrices for determining the Alexander polynomial using the methods described above

7.4 Absence of knots

Contrary to expectation, a full search of the data (≈ 500000 loops in cells of various sizes) returned a null result for knots, either within the loops or

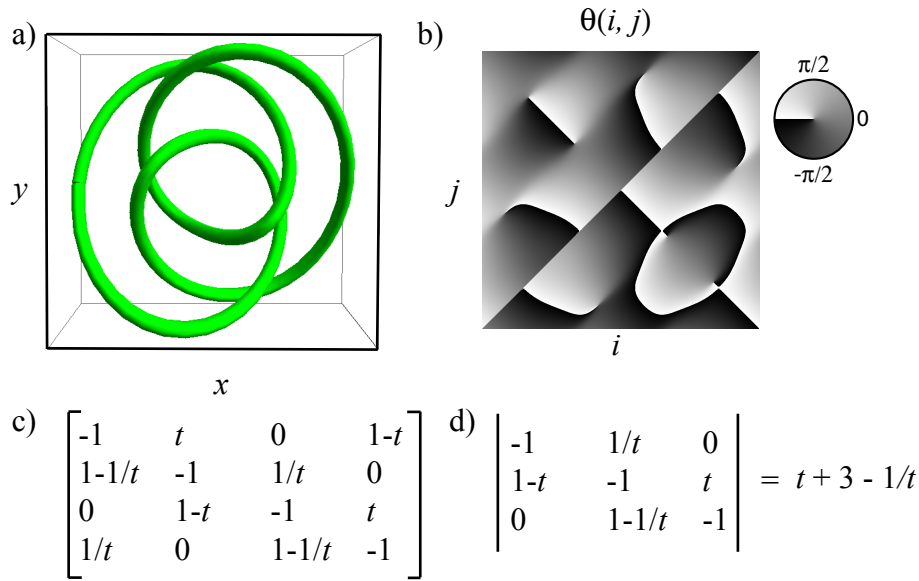


Figure 7.7: a) A prime figure eight knot and (b) the corresponding chord angle plot of the xy projection of the knot. The resulting matrix used to calculate the Alexander polynomial is shown in (c). The Alexander polynomial is the determinant of any principle minor of this matrix. One such principle minor is shown in (d).

indeed on a period of the infinite lines. It is unclear whether this is due to extreme rarity, or, less likely, some hidden prohibition of knots in the modeled ensemble of random fields. It is tempting to conjecture that the probability distribution of a vortex knot of a specific length occurring is similar that of other systems of random tangled filaments, specifically polymers, which has been much studied [OW07]. It is numerically observed, across a range of physical models of random polymer loops, that the probability, P_{\circ} , that a loop of length L is the un-knot is

$$P_{\circ} = e^{-L/CP}, \quad (7.7)$$

where P is the persistence length of the polymer (for vortex lines in speckle $P = 0.17\lambda$) and C is a dimensionless, large number that depends on the details of the specific model. The value of C ranges from ~ 300 for random piecewise linear loops with segments of equal length, to ~ 10000 for closed random walks on cubic lattices [OW07].

It follows that the probability, $P_{\circ}(N)$, of N loops all being un-knots is the product of the individual probabilities and hence related to the sum of all the loop lengths under consideration, i.e.

$$P_{\circ}(N) = \exp \left[- \sum_{i=1}^N L_i / CP \right]. \quad (7.8)$$

Considering only loops of a length within the range of which links have been found ($2\Lambda < L < 35\Lambda$), and restricting the search to the data set with highest number of plane wave components, results in ≈ 15000 loops. These loops amount to a total length of $\approx 1.2 \times 10^5 \Lambda$ and hence result in an estimated lower bound for $C > 1.2 \times 10^5$.

7.5 Discussion

This chapter has established numerically that vortex lines that are formed within random 3D speckle do exhibit complex topologies such as threading and linking. However, such random links are extremely rare, occurring for approximately 2 in 5000 loops. Although all calculated volumes have been searched for knots using the Alexander polynomial, none have yet been found. As it is possible for beams to be designed with vortex knots [BD01b, LDCP04a], it is assumed that knots in random fields do exist but are rare. Comparing the exponential decay of unknotting probability observed in other systems [OW07] with the loop length searched for knots, a lower bound for C can be estimated at 1.2×10^5 . From the loop size density scaling observed in chapter 6 a loop of length $10^5 P$ occurs once in a volume of $\approx 4^{10} \Lambda^3$ — some 10^5 times larger than the total volume generated and searched.

Knots and links in the lab

This chapter gives the first results of isolated knotted and linked vortex lines in Gaussian beams. Results for three different topologies are shown here: the Hopf link, the trefoil knot and the cinquefoil knot. In all three cases there are no other singularities near the structure of interest — they are compact. This is the feature which most distinguishes this work from that of Leach et. al. [LDCP04a, LDCP05]. First the method of calculating the mode coefficients will be described (which was the work of Mark Dennis) then results given. The mode optimisation algorithm and experimental results are the major contribution of the author.

8.1 Embedding algebraic knots in Gaussian beams

The first methods developed for creating knotted vortex lines involved starting with a high charge vortex line threading vortex loops [BD01b, BD01a]. This field would then be perturbed, causing the high charge vortices to split and loops to be nucleated (see chapter 4 for a discussion of this process for the Hopf link). The field would then be perturbed further in a controlled

manner until the desired topology was reached. Due to the initial condition of a high charge vortex line, these structures were always threaded by a number of single charge vortex lines that were not part of the knot or link.

The singularities threading these structures makes experimental efforts difficult, as reconnections can happen if the modes created are not of the correct weighting, or aberrations are present in the optical alignment. From a mathematical viewpoint, these vortex lines made the structure less elegant, as it was no longer compact, the threading lines reaching to infinity.

Creating complex fields with specific singularity structure is not difficult [Den08] if one is not confined to wave equations. For example, a vortex loop can be generated by creating a field which has a $\xi = 0$ contour as a plane and $\eta = 0$ contour as a cylinder or sphere intersecting the plane. This type of field will indeed contain a vortex loop but will most likely not satisfy the wave equation.

Disregarding the conditions that wave equation places on the construction of a complex field, it is possible to engineer fields where the intersections between $\xi = 0$ and $\eta = 0$ create links or knots. This type of mathematical construction relies on the algebraic description of knots, and is easiest for torus knots — curves which are knotted and can be made to lie on the surface of a torus. As vortex lines are lines where all surfaces of constant phase coincide, the phase contours emanating from the vortex line are said to ‘fibre’ the line [Rol03]. Consequently only fibred knots may be candidates for knots in vortex lines (whether restricted by wave equation or not).

8.1.1 Algebraic fibred knots

In the 1960s, Milnor described a method of constructing complex scalar fields that contained knotted or linked vortex lines using polynomials in two complex variables [Mil68],

$$K(u, v) = u^m - v^n \tag{8.1}$$

where

$$u = \frac{r^2 - 1 + 2iz}{r^2 + 1} \quad \text{and} \quad v = \frac{2(x + iy)}{r^2 + 1}. \quad (8.2)$$

Inspection of these polynomials reveals why they can be useful in creating interesting fields. The u term contains a vortex ring perpendicular to the z axis and the v term contains $(x + iy)$, which is arguably the simplest expression to contain a phase singularity. Taken separately, u and v contain vortex lines which are perpendicular to each other.

The following realisations of $K(u, v)$ create complex fields with vortex lines forming a Hopf link, trefoil knot and cinquefoil knot respectively:

$$K_H = u^2 - v^2 \quad \text{Hopf link} \quad (8.3)$$

$$K_T = u^3 - v^2 \quad \text{trefoil knot} \quad (8.4)$$

$$K_C = u^5 - v^2 \quad \text{cinquefoil knot.} \quad (8.5)$$

To understand why the hierarchy of powers of these polynomials in conjunction lead to a hierarchy of topology is beyond the scope of this chapter (and indeed the author).

The next step in realising these knots in Gaussian beams was one made in an effort of enquiry, to see what vortex structure did result from simply embedding the ‘waist’ ($z = 0$ plane) of an algebraic knot, K_0 , in the waist of a Gaussian beam and propagating the field

$$\Psi = K_0(u, v)e^{-r^2/2w_0^2}. \quad (8.6)$$

The result, for a certain range of beam waist, w , was a vortex line of the topology described by $K(u, v)$! This result is yet to be fully understood and is a line of ongoing theoretical research.

Numerical experimentation has shown that there is a critical waist, w_c , below which the topology ceases to be that of $K(u, v)$. At $w > w_c$ there exist vortices at large distances from the waist, coming closer to the vortex lines in the waist plane as w is decreased. In $K(u, v)$ alone there are no such vortices. It would seem at large (and even infinite) waist values, the propagation of

the field does perturb the ‘ideal’ configuration of the structure, but not enough to cause topology changing reconnections. Despite this lack of full understanding, the results of experiments which successfully generated the Hopf link, trefoil knot and cinquefoil knot are reported here, which is the main contribution of the author.

8.2 Modal composition of structures

The following ‘recipes’ for creating links and knots are found by decomposing Eqn. 8.6 into Laguerre-Gauss modes. These structures are experimentally realised by using the following equations in conjunction with the hologram generation methods described in chapter 3.

Hopf link

$$\begin{aligned}
 \Psi_H &= K_H e^{-r^2/2w^2} \\
 &= (1 - 2w^2 + 2w^4) \text{LG}_0^0 \\
 &\quad + (2w^2 - 4w^4) \text{LG}_1^0 \\
 &\quad + (2w^4(9w^2 - 1)) \text{LG}_2^0 \\
 &\quad - 4\sqrt{2}w^2 \text{LG}_0^2
 \end{aligned} \tag{8.7}$$

Trefoil knot

$$\begin{aligned}
 \Psi_T &= K_T e^{-r^2/2w^2} \\
 &= (1 - w^2 - 2w^4 + 6w^6) \text{LG}_0^0 \\
 &\quad + (w^2 + 4w^4 - 18w^6) \text{LG}_1^0 \\
 &\quad + (2w^4(9w^2 - 1)) \text{LG}_2^0 \\
 &\quad - 6w^6 \text{LG}_3^0 \\
 &\quad - 8\sqrt{6}w^3 \text{LG}_0^3
 \end{aligned} \tag{8.8}$$

Cinquefoil knot

$$\begin{aligned}
\Psi_C &= K_C e^{-r^2/2w^2} \\
&= (1 + w^2 - 4w^2 - 12w^6 + 24w^8 + 120w^{10})\text{LG}_0^0 \\
&\quad - w^2(1 - 8w^2 - 36w^4 + 96w^6 + 600w^8)\text{LG}_1^0 \\
&\quad - 4w^4(1 + 9w^2 - 36w^4 - 300w^6)\text{LG}_2^0 \\
&\quad - 64\sqrt{30}w^5\text{LG}_0^5 \\
&\quad + 12w^6(1 - 8w^2 - 100w^4)\text{LG}_3^0 \\
&\quad + 24w^8(1 + 25w^2)\text{LG}_4^0 \\
&\quad - 120w^{10}\text{LG}_5^0
\end{aligned} \tag{8.9}$$

8.3 Optimisation for experiment

Although the modal compositions described above both satisfy the paraxial equation and contain linked/knotted singularities (for $w > w_c$), they may not be easy to create or measure experimentally. In fact, the Hopf link was the most straightforward structure of those reported here as it was comprised of two planar loops, only coming close to each other where the topological charge of each vortex line prohibited reconnections from occurring. However, the trefoil and cinquefoil knots were both problematic, each failing in the first attempts to create them due to reconnections in the very dark central region of the beam. This was overcome through a numerical search optimisation.

8.3.1 Search parameters

The modal compositions described in the previous section give an excellent starting point (i.e. a beam containing a knot) in a very large parameter space (all possible LG mode combinations and weightings). It is a matter of perturbing a set of parameters incrementally to explore the local parameter

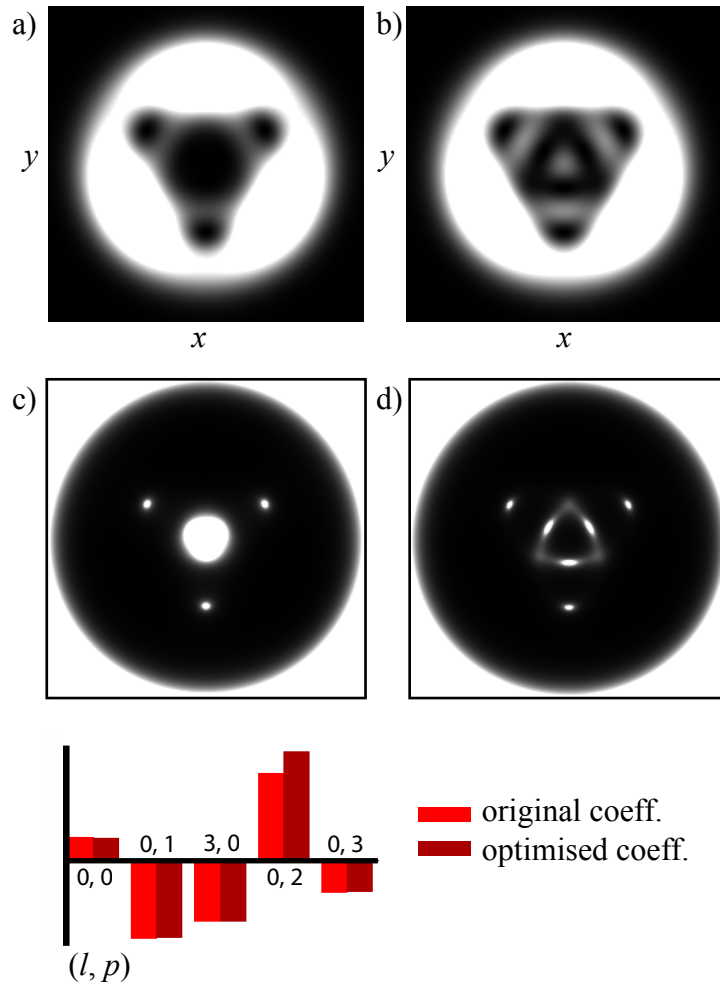


Figure 8.1: Shown are the intensities of (a) the beam waist calculated using Eqn. 8.8 with $w = 1.2$ and (b) the beam after several hours of randomly perturbing mode coefficients and accepting perturbations that minimise the sum of inverse intensity in the volume. Both are shown in grayscale with white corresponding to $1/4$ maximum intensity in the beam waist. The corresponding inverse intensities (also with a grayscale threshold) are shown in (c) and (d) respectively. The relative LG_p^l coefficients are shown in the bar plot.

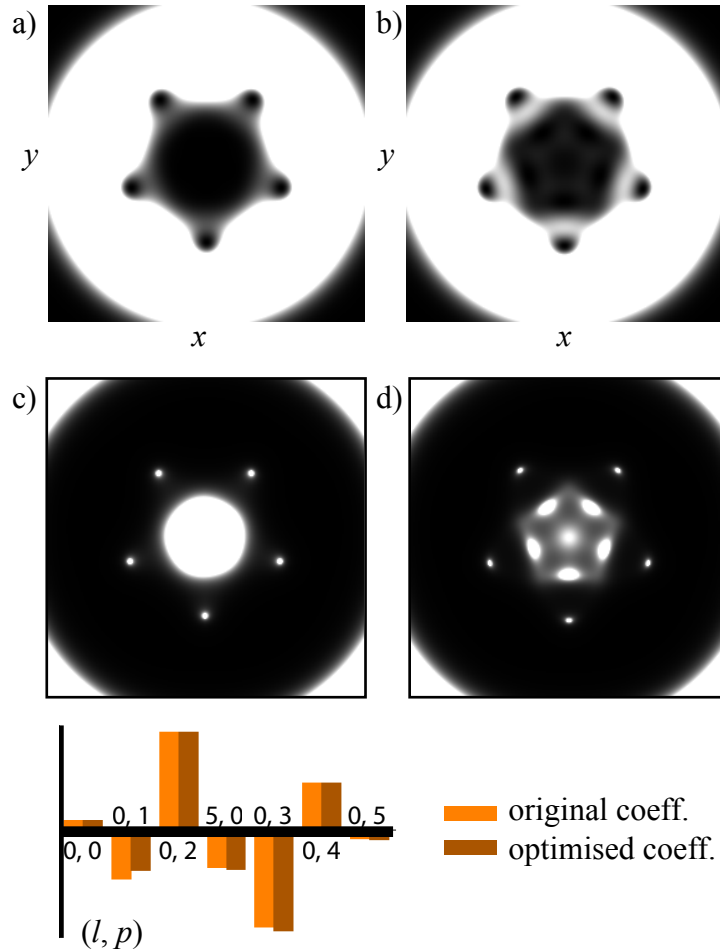


Figure 8.2: Shown are the intensities of (a) the beam waist calculated using Eqn. 8.9 with $w = 0.93$ and (b) the beam after several hours of randomly perturbing mode coefficients and accepting perturbations that minimise the sum of inverse intensity in the volume. Both are shown in grayscale with white corresponding to 5% maximum intensity in the beam waist. The corresponding inverse intensities (also with a grayscale threshold) are shown in (c) and (d) respectively. The relative LG_p^l coefficients are shown in the bar plot.

space. An obvious choice of parameters, which allow minor deformations of the field, are the real amplitudes of the LG modes making the field.

Other parameters could be used, such as the random inclusion of modes not present, or modification of w (which is set as a constant in the method implemented here). However, in an initial optimisation attempt, without much ‘feeling’ for the parameter space, or indeed the merit function landscape, it is best to keep the number of variables low. Following this guide, the only parameters allowed to vary were the magnitudes of modes present in the initial field and only by small amounts — a Gaussian spread around the selected magnitude with a standard deviation of $\approx 3\%$ of its value.

Once a mode was selected and modified, the field was propagated using a standard Fourier transform technique. The propagation distance was set such that the original structure was easily encompassed in all dimensions. Using the methods described in chapters 3, 6 and 7 for finding, sorting and identifying topology of vortex lines, the resulting field was analysed and the return values for the iteration were a TRUE/FALSE value for the topology of the vortex line (the topology must remain constant throughout the optimisation), a TRUE/FALSE value on there being only one vortex line in the calculated volume (as the purpose of the experiment is to produce a compact structure) and finally, a TRUE/FALSE value evaluated on some merit function which defines the optimisation.

At the end of each iteration, the modification to the mode amplitude is made permanent if all of the return values are TRUE. The first two boolean values are drawn from necessity, they are absolutely required to achieve the field desired. The merit function can be defined arbitrarily and must be considered carefully.

8.3.2 Merit function

Although a few different merit functions were tried, the most successful (and most simple to implement) was the minimisation of inverse intensity

(or maximising intensity). This merit function might seem contradictory towards the goal — trying to achieve a better knotted line of zero intensity by adding more light. However, as the initial field already contains a knotted zero line *and* there is an absolute requirement to retain this line in its original topology, the optimisation proceeds in a direction in parameter space that fullfills both requirements — more light but still with a knotted zero.

Other, more complex, merit functions may have arrived at a solution quicker, or better than the one used to generate the results given here, but these optimisation routines are a means to an end. If a particular merit function converges in minutes or hours then the details are not so important as long as the converged set of parameters are successful.

Figures 8.1 and 8.2 compare optimised fields with the forms given in Eqn.s 8.8 and 8.9. In both figures, part (a) shows the beam waist of Ψ_T and Ψ_C , with $w = 1.2$ and $w = 0.93$ respectively, while (b) shows the beam waist after several hours (corresponding to several hundred iterations) of optimisation, using the merit function described above. The inverse intensities are shown in parts (c) and (d) as it is clearly visible from these images that the merit function has been successfully minimised.

8.4 Results

The results given here were obtained using the methods described in chapter 3 and the Laguerre-Gauss recipes described above. With the exception of the Hopf link, the beams were also optimised using the random search algorithm described in the previous section, with the merit function being the minisation of inverse intensity.

Figure 8.3 shows the measured vortex structure in a field generated using the field, Ψ_H described in Eqn. 8.7 with $w = 1.4$. This value of w results in a structure which spans $z = -0.5z_r$ to $z = 0.5z_r$. The volume scanned was a region approximately 50mm in length and 1mm^2 transversely. The axial

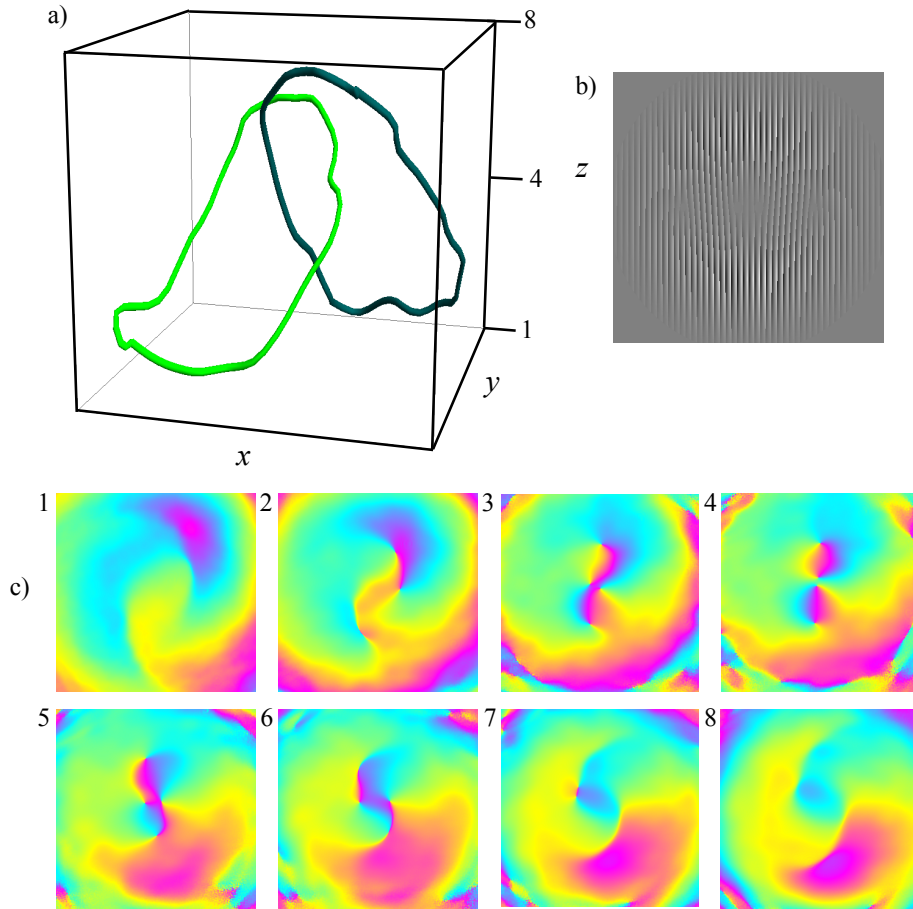


Figure 8.3: a) Two vortex loops forming a Hopf link. b) Phase hologram used to generate the field. c) phase cross-sections (xy plane) at the z values indicated in (a).

extent of the structure corresponds to a beam waist size of $\sim 120\mu\text{m}$.

Figure 8.4 shows the measured vortex structure in a field generated using the field, Ψ_T described in Eqn. 8.8 with $w = 1.2$ and optimising the field using the minimisation of inverse intensity as a merit function. The volume scanned was of the same length and proportions to that of the previous experiment. Although it is clear from inspection that the vortex line is a trefoil knot, the Alexander polynomial was calculated using the method developed in chapter 7. As expected the result was a match for the trefoil: $(t - 1 + t^{-1})$.

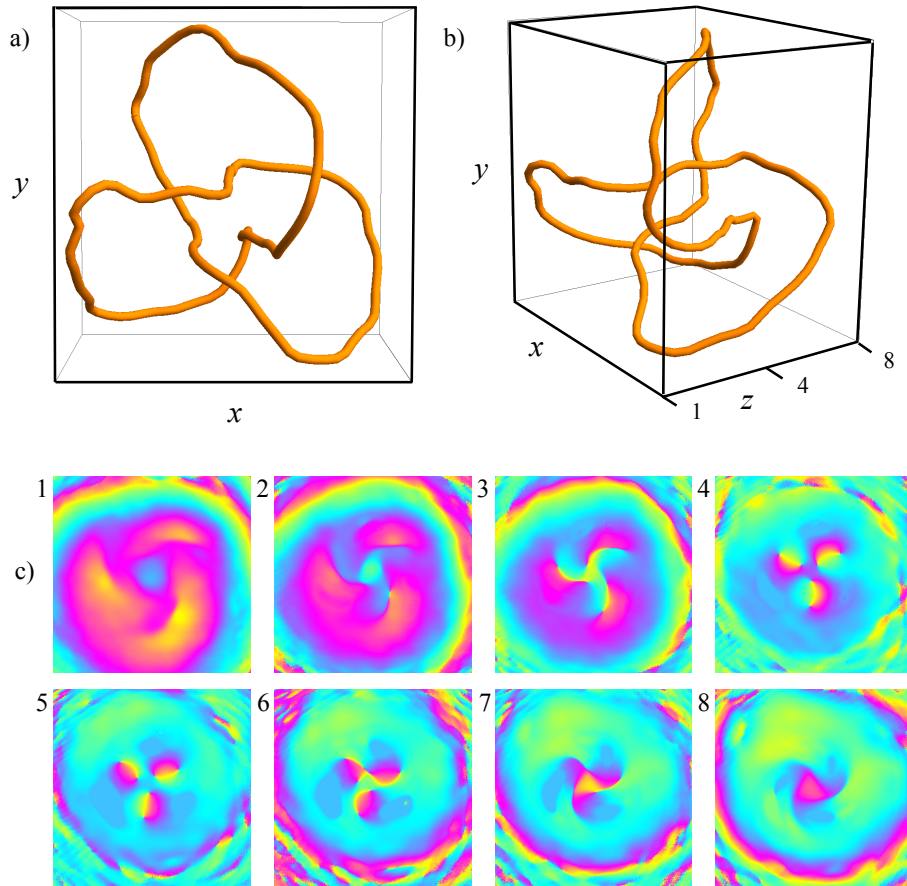


Figure 8.4: a) and (b) show two different viewpoints of the vortex line forming a trefoil Knot. c) shows phase cross sections in the xy plane at the z values indicated in (b). This knot was generated by first using the ideal LG modal composition and then iterating a random search for a composition which was easier to generate and measure in the lab.

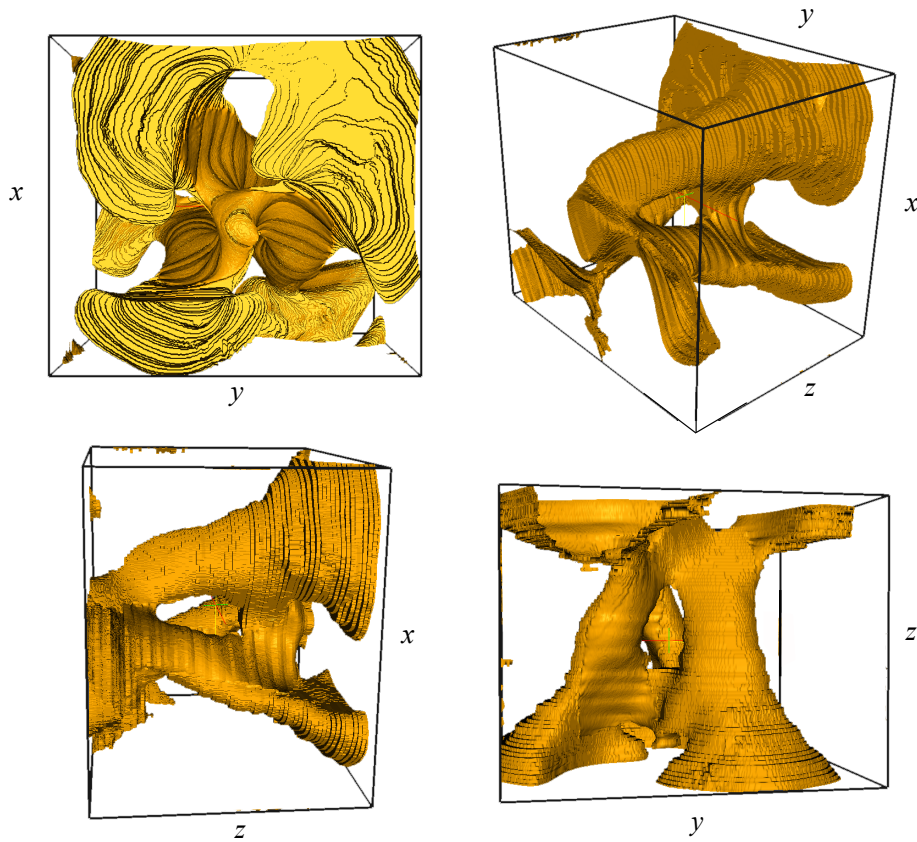


Figure 8.5: Four different viewpoints of the $\xi = 0$ surface which ‘fibres’ the trefoil knot, in the bottom two views it can be seen that this surface is a two-holed torus.

As the field structure is not too complicated, the $\xi = 0$ surface, which ‘fibres’ the knot has also been plotted in Fig. 8.5. It the topology of the surface can be seen as a two-holed tori, as expected.

Figure 8.6 shows the measured vortex structure in a field generated using the field, Ψ_C described in Eqn. 8.9 with $w = 0.93$ and optimising the field using the minimisation of inverse intensity as a merit function. The volume scanned was of the same length and proportions to that of the previous experiments.

If allowed to manipulate the viewpoint of the 3D plot in Fig. 8.6, it is clear that the vortex line forms a cinquefoil. To confirm, the Alexander polynomial

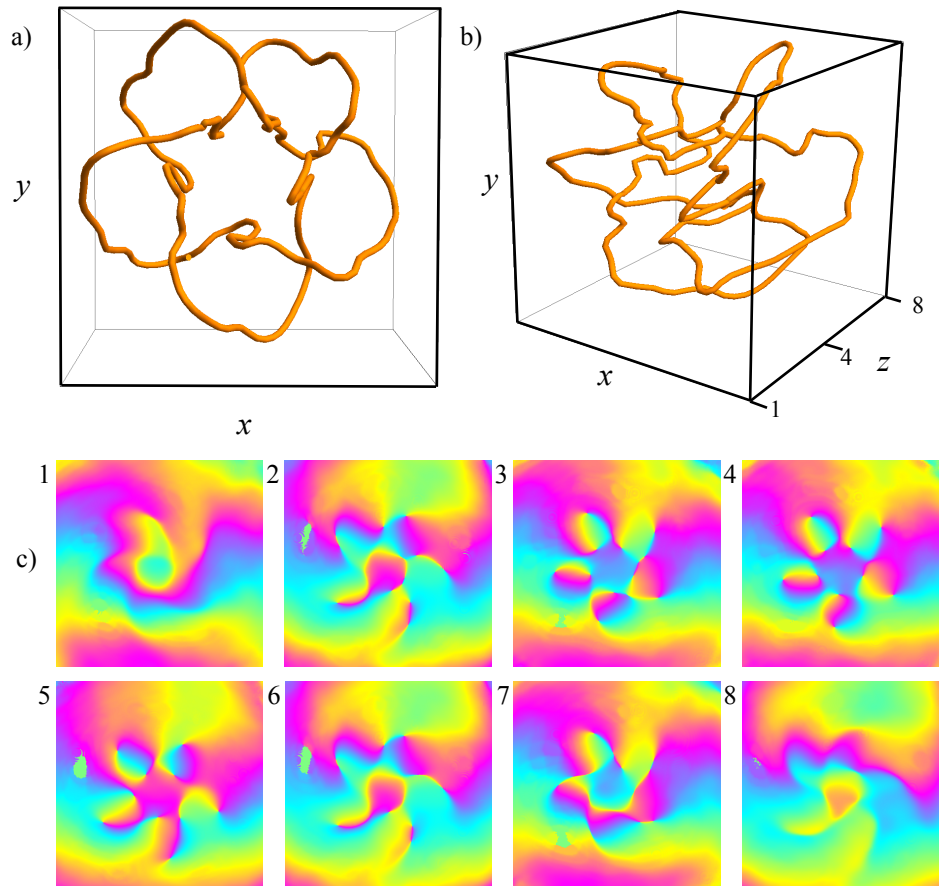


Figure 8.6: a) and (b) show two different viewpoints of the vortex line forming a cinquefoil Knot. c) shows phase cross sections in the xy plane at the z values indicated in (b). This knot was generated by first using the ideal LG modal composition and then iterating a random search for a composition which was easier to generate and measure in the lab.

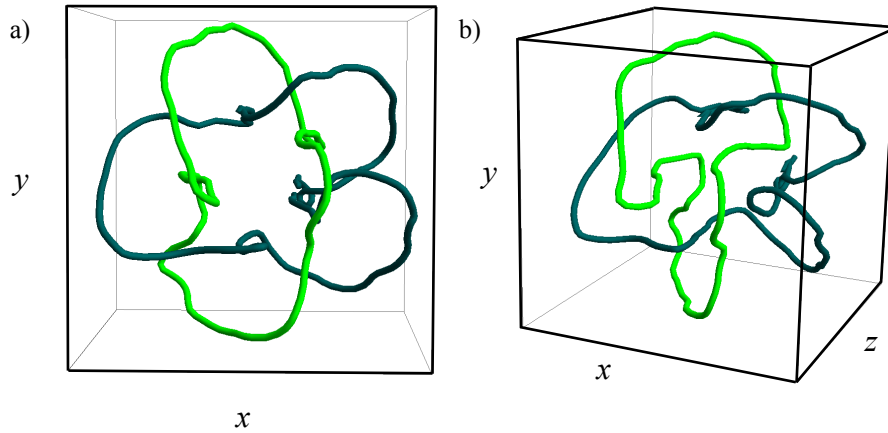


Figure 8.7: a) and (b) show two different viewpoints of two vortex lines forming a 4-twist link, which has a linking number of two. This was a failed attempt to generate a cinquefoil knot from the original unoptimised mode coefficients

was calculated to be $(t^2 - t + 1 - t^{-1} + t^{-2})$, as expected.

Surprise in failure

In attempting to create the cinquefoil knot from Ψ_C with $w = 0.93$ without optimising a 4-twist link was created. The measured vortex lines are shown in Fig. 8.7. This was purely accidental, but highlights the interesting topological region of parameter space that these polynomial/Gaussian embeddings have found.

8.5 Discussion

This chapter saw the first reports of compact knotted vortices in real Gaussian beams. The Hopf link, trefoil knot and cinquefoil were all successfully generated and measured. Why the embedding of algebraic knots in Gaussian beams works is still not clear, however it is clear that this implementation is not perfect. Even with a large Gaussian waist size (relative to the knot)

there are other singularities in the far-field — the knot itself is compact but the field does contain other singularities. This feature is highlighted when the critical waist size is approached and the singularities which were restricted to the far-field are now much closer to the knot and cause topology changing reconnections.

During the optimisation, generation and measurement of these structures, all methods discussed and developed in previous chapters for finding and analysing vortex lines were used. These methods included: numerical beam propagation; hologram design; phase retrieval through interferometry; vortex locating in three dimensions; vortex sorting and topology identification. As such it is fitting that this chapter concludes the phase singularity content of the thesis.

The remaining chapter will give experimental results for the densities of polarisation singularity types and again phrase the terminology in three dimensions, showing visually how star, lemon and monstar singularity types relate to each other in three dimensions.

Polarisation Singularities

In the transverse plane of paraxial optical fields with position-dependent elliptic polarisation, there are isolated points of circular polarisation (C-points), around which the major axis of the polarisation ellipse (tangent to the polarisation *streamline*), rotates by $\pm\pi$, [Nye83b]. The positive index singularities occur in two forms: the *lemon* type, on which only one streamline terminates, and the less common *monstar*, on which three straight streamlines terminate. On negative-index singularities, termed *stars*, there are always three streamlines that terminate [Ber77]. These singularities occur throughout polarisation optics, e.g. tightly-focused beams and near-field optics [LPS⁺07], skylight [Ber04] and crystal optics [FSMD05, FSMD06]. As these fields propagate, the polarisation changes continuously and the C-points sweep out C-lines.

9.1 Polarisation singularity statistics

As explained in chapter 2, certain statistics for polarisation singularities, such as point densities, are simply double that of phase singularities in scalar fields of the same type. For example, in speckle fields with spatially varying

polarisation, the polarisation singularity density is double the phase singularity density in scalar speckle, i.e. $4\pi/\Lambda^2$. This doubling is understood by decomposing the vector field that describes polarisation into two orthogonal components: left- and right-circularly polarised light. These two components are described by complex scalar fields and as such are subject to all of the results contained in previous chapters. By superposing the two fields together, the network of zero intensity lines that existed in each become lines of circular polarisation of the opposite.

The advantage of this realisation is the immediate knowledge of some properties of C-lines in random vector fields: C-lines will share the same fractal/scale invariant properties of phase singularities and each left and right-handed set of C-lines will share the topological densities investigated in chapter 7. However, there are properties which do not exist in complex scalar fields. These properties are predominately the result of the π symmetry in the headless vector that describes the polarisation state of light and are the subject of this chapter.

Firstly, methods will be described for distinguishing singularity type. Experimental and simulated results for densities of star, lemon and monstar type singularities, as well as elliptic and hyperbolic type, will be given and compared with predictions [Den02]. Other quantities measured which currently have no theoretical predictions are the length densities of different singularity types.

9.2 Distinguishing singularity type

The singularity index is evaluated from the sign of D_I , calculated from the spatial derivatives of Stokes parameters,

$$D_I = S_{1,x}S_{2,y} - S_{1,y}S_{2,x}, \quad (9.1)$$

where x, y subscripts denote spatial derivatives. Having distinguished stars from monstars and lemons, the sign of D_L distinguishes between monstars

and lemons [Den02]:

$$\begin{aligned}
 D_L = & ((2S_{1,y} + S_{2,x})^2 - 3S_{2,y}(2S_{1,x} - S_{2,y})) \\
 & \times ((2S_{1,x} - S_{2,y})^2 + 3S_{2,x}(2S_{1,y} + S_{2,x})) \\
 & - (2S_{1,x}S_{1,y} + S_{1,x}S_{2,x} - S_{1,y}S_{2,y} + 4S_{2,x}S_{2,y})^2.
 \end{aligned} \tag{9.2}$$

If three straight streamlines meet at the singularity then $D_L > 0$ and the singularity is a star or monstar, if $D_L < 0$ then the singularity is a lemon. Figure 9.2 shows the experimentally measured polarisation streamlines in the vicinity of a number of C-points.

A third classification, the contour classification, divides C-points into hyperbolic or elliptic types [Nye99]. This classification relates to the shape of contours of the polarisation ellipse axes which forms a double cone structure [Ber77, Nye99], and is an additional prediction against which observations can be compared. A C-point is elliptic or hyperbolic depending on the sign of D_C , given by [Den02],

$$\begin{aligned}
 D_C = & (S_{1,x}S_{2,y} - S_{1,y}S_{2,x})^2 - (S_{1,x}S_{0,y} - S_{1,y}S_{0,x})^2 \\
 & - (S_{0,x}S_{2,y} - S_{0,y}S_{2,x})^2,
 \end{aligned} \tag{9.3}$$

where D_C is negative for hyperbolic C-points and positive for elliptic C-points.

9.3 Experiment

The experimental apparatus used to obtain the results reported here was that shown in chapter 3. For this experiment, the area highlighted in Fig. 3.15 as ‘object which alters polarisation’ contained a polarising beam splitter, relay mirrors and a ground glass plate. This component of the apparatus is illustrated in Fig. 9.1. The polarising beam splitter splits the initially linearly polarised beam into two orthogonal linearly polarised beams. The two beams are then incident on a ground glass plate. After being scattered by the ground glass plate, the beams are recombined. The resulting field is

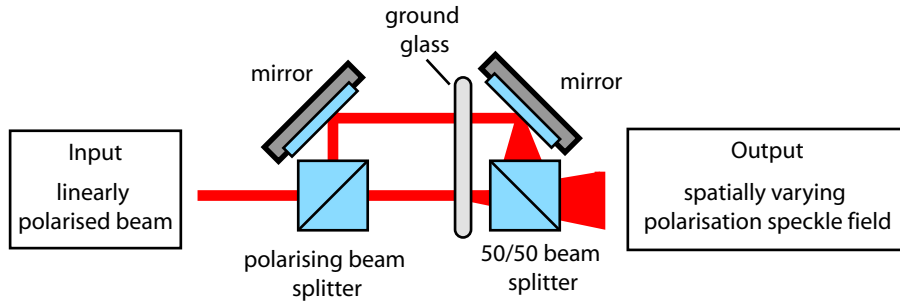


Figure 9.1: The integral part of the apparatus shown in chapter 3 Fig. 3.15 that generates a spatially varying polarisation speckle field. The incident linearly polarised light is oriented such that the polarised beam splitter splits the beam into two beams of equal power and orthogonal linear polarisation. The two beams are incident on a ground glass plate, resulting in two orthogonally polarised speckle fields. These two fields are then recombined.

superposition of two linearly polarised orthogonal speckle fields. The methods used to measure Stokes parameters are described in chapter 3 and will not be repeated here.

9.4 Numerical experiments

To accompany the experimental measurements, speckle fields were also numerically simulated. These simulations were based on the superposition of two random scalar wave fields with opposite signs of circular polarisation. Each of these fields was a superposition of ≈ 3000 plane waves, randomly distributed in direction and with Gaussian distributed complex amplitudes. These amplitudes were then subject to a Gaussian envelope to simulate the transverse power spectrum of laser light scattered from a rough surface (this method is detailed in chapter 6). The resulting field was calculated over a large number of cross-sections to obtain the statistical distribution of stars, monstars and lemons. Calculating neighboring cross-sections creates a 3D structure of C-lines and L-surfaces. As with the work on scalar fields (chap-

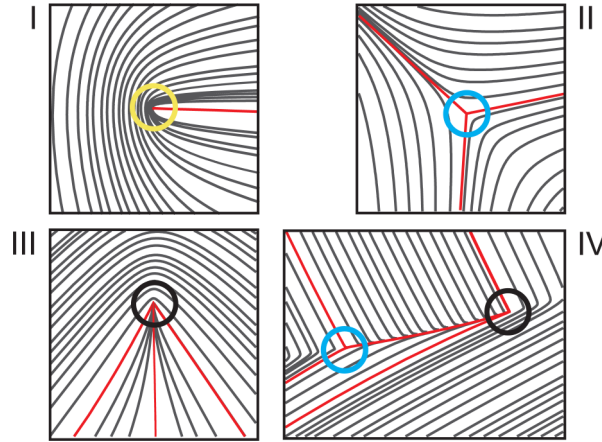


Figure 9.2: Examples of four C points and nearby polarisation streamlines as measured in experiment. Part I is lemon type, part II star, part III monstar, and part IV a cross-section near a star-monstar transformation.

ter 6), interference between a hundred plane waves, or more, repeatedly calculated over one or two coherence lengths, gives stable statistics for the singularities.

The data from the experiments and numerical simulation was a 3D grid of voxels, each with numerical values for the four Stokes parameters. In every cross-section, the singularity index is calculated at each pixel from a line integral of the polarisation ellipse axis, $\frac{1}{2} \arg(S_1 + iS_2)$ (algorithmically the same method used for finding phase singularities). Once singularities were identified, the Stokes parameters S_1, S_2 were interpolated to quadratic order and subjected to a root-finding algorithm to more precisely locate C-points. This was a processing step not used in the studies of phase singularities but was necessary here to measure derivatives accurately in order to determine singularity type using Eqn.s 9.1 and 9.2.

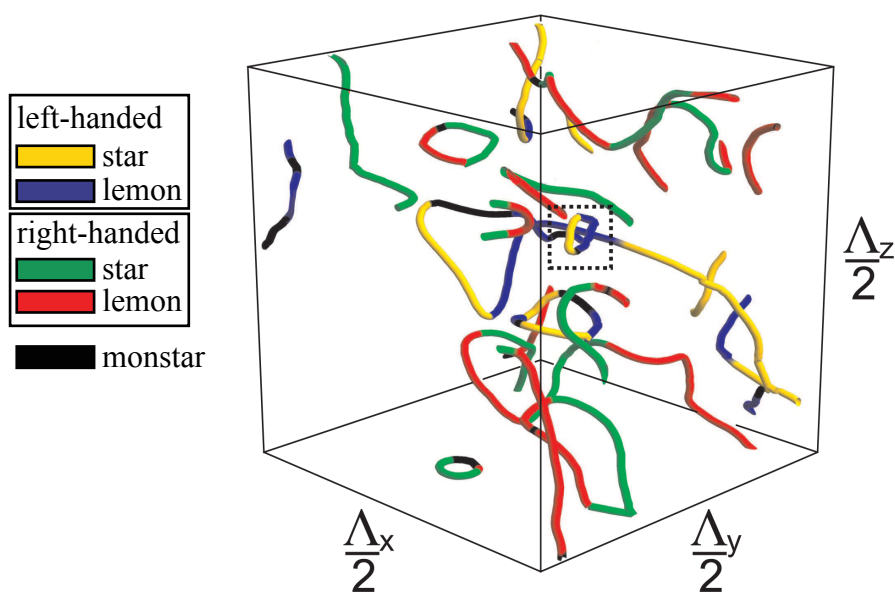


Figure 9.3: A volume of experimentally measured C-line structure.

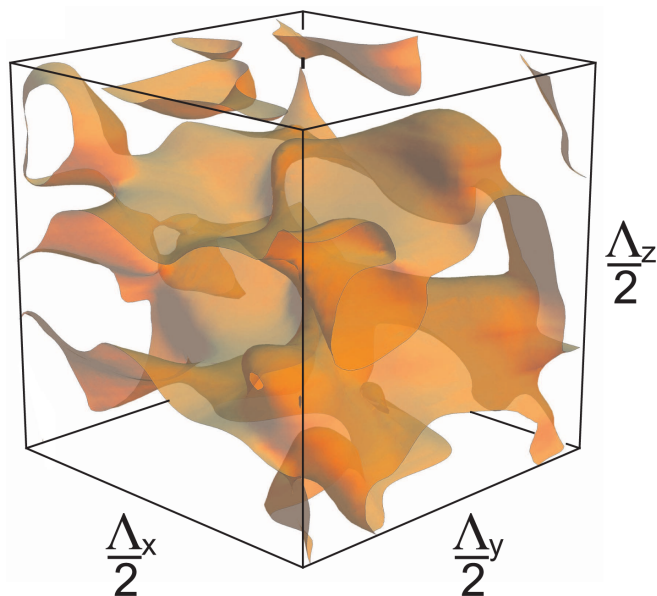


Figure 9.4: A volume of experimentally measured L-surface structure. This is the same volume shown in Fig. 9.3.

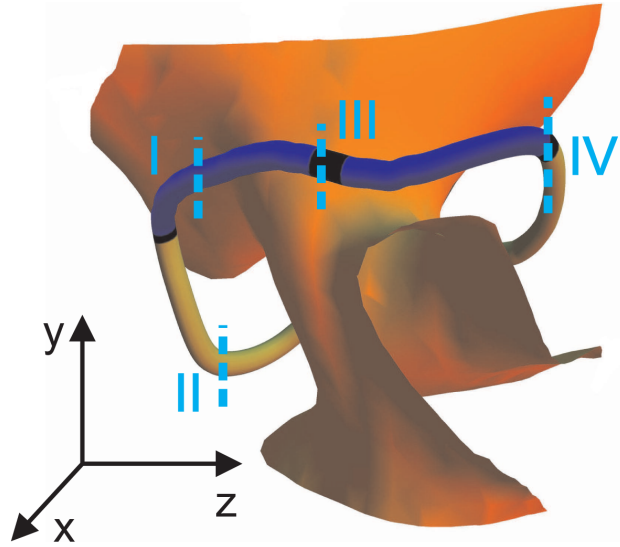


Figure 9.5: Shown here are both the singularity type and L-surface in the vicinity of C-line forming a loop. The colour coding is the same as used in Fig. 9.3. The Roman numerals show the points for which the streamlines are plotted in Fig. 9.2.

9.5 Results

Dennis [Den02], generalizing earlier work by Berry and Hannay on umbilic points on random surfaces [Ber77], calculated the density of C-points and the ratios of their different types in an isotropic random wave model. These predicted that the density of C-points per unit area is $4\pi\Lambda^{-2}$ (where Λ is the transverse coherence length of the complex vector field) and the star:lemon:monstar ratio is 50 : 44.72 : 5.28. Since C-points in random vector speckle fields are the vortices in the independent, identically distributed left and right circular components, the C-point density is twice the underlying vortex density of $2\pi\Lambda^{-2}$ [BD00, Ber78], which has been verified experimentally [WHMT05]. Polarisation singularity densities have been investigated in experiments, but with data sets that were too small to give average densities [DES04]. Table 9.1 shows the breakdown of observed and simulated C-points into their singularity type, further specified by the corresponding Stokes matrix into elliptic or hyperbolic singularities. The quoted

Singularity type	simulation	experiment	Dennis[Den02]
Star	0.501 ± 0.002	0.506 ± 0.003	0.5000
Lemon	0.450 ± 0.003	0.443 ± 0.002	0.447
Monstar	0.049 ± 0.002	0.050 ± 0.003	0.053
Star [E/H]	1.035 ± 0.054	1.073 ± 0.078	1.000
Lemon [E/H]	1.133 ± 0.078	1.086 ± 0.112	1.104
Monstar [E/H]	0.418 ± 0.056	0.487 ± 0.031	0.404

Table 9.1: Fraction of C-points of different types in transverse cross-sections and ratio of elliptic to hyperbolic types (E/H). The simulations average over > 90000 C points, the experiments over > 35000 C points.

Singularity type	simulation	experiment
Star	0.504 ± 0.008	0.496 ± 0.011
Lemon	0.420 ± 0.005	0.422 ± 0.010
Monstar	0.076 ± 0.005	0.082 ± 0.011
Star [E/H]	0.814 ± 0.039	0.727 ± 0.081
Lemon [E/H]	0.944 ± 0.058	0.787 ± 0.010
Monstar [E/H]	0.260 ± 0.028	0.274 ± 0.038

Table 9.2: Fraction of C lines of different type and ratio of elliptic to hyperbolic (E/H) types, evaluated over numerically simulated ($5 \times \Lambda^3$) and experimentally observed ($2 \times 1.25\Lambda^3$) volumes.

errors are a combination statistical uncertainty based on the finite numbers of singularities found and by varying the radius of the line integral around the C-points. However, in all cases the agreement with the analytic predictions [Den02] is excellent. Additionally, the density of numerically simulated C points is $12.51\Lambda^{-2}$, which is close to the predicted value of $4\pi\Lambda^{-2} \approx 12.57\Lambda^{-2}$.

Figures 9.3 and 9.4 show a typical experimental observation of a C-line and the associated L-surface structure within a random vector speckle field. They are plotted over one eighth of a natural volume Λ^3 ($\Lambda/2$ in each axis). Throughout the volume, the C-lines are colour-coded to denote stars, monstars and lemons of both right- and left-handed circular polarisation. As anticipated [Nye83b, Nye99], the C-line loops comprise mainly of stars and

lemons, with short monstar sections at the maximum and minimum z -extent. Monstars also frequently occur within the lemon section of the C-line, far away from the turning points, and it is these monstars that appear most commonly. Figure 9.5 shows a small section of the volume in Fig. 9.3, highlighting one C-line loop and the linearly polarised L-surface in its vicinity, separating it from the C-lines of opposite handedness. Sections I-IV are those for which the streamlines are plotted in Fig. 9.2.

By rescaling z , so the coherence lengths $\Lambda_{x,y,z} = \Lambda$, the tangent direction of C-lines is expected to be uniformly distributed. From the solution to the classical ‘Buffon needle problem’ [AZ01], generalized to lines in 3D [Den07], the C-line density per unit volume ought to be twice the C-point density in transverse section, i.e. $8\pi\Lambda^{-2} \approx 25.133\Lambda^{-2}$, which again is double that expected from phase singularities. The numerical simulations give this line density as $25.76\Lambda^{-2}$.

In addition to the C-line density, the distribution of singularity type as a fraction of C-line length is considered, given in Table 9.2. These are different from the results of Table 9.1, where the density is weighted in proportion to the z -component of the C-line tangent. In particular, since monstars occur when C-lines are approximately perpendicular to the propagation direction, their 3D weighting is higher (7.6%) than in transverse sections (5.3%). It appears also that the elliptic weighting dominates over the hyperbolic. As yet there are no analytic calculations for these numbers to match the results of Table 9.2, although for fields where the polarisation ellipse plane orientation is also random [BD01b], the 3D weightings are expected to match Table 9.1.

9.6 Summary

Polarisation singularities – C-lines and L-surfaces – have been experimentally visualised in random vector speckle fields. Given that polarisation fields can be decomposed into orthogonal complex scalar fields, it is reasoned that

the large scale structure is identical to that reported in chapter 6 for phase singularities in scalar speckle fields. In addition to verifying the singularity type distribution in 2D against theoretical predictions, new experimental and simulated predictions for their three-dimensional counterparts have been presented, including through the Buffon needle problem a link between their 2D and 3D statistics.

CHAPTER 10

Conclusions

This thesis has covered many properties of optical singularities, from the vortex topology resulting from few plane-wave interference, to the vast network of Brownian vortex lines in speckle fields and the subtle interplay between polarisation singularity types in three-dimensions. The thesis also contained experimental reports of new, novel beams which contain compact knots. During its course to develop and report these main results, peripheral work, which at the time were a means to an end, have themselves become worthy of note. Such examples are the development of a 3D complex optical data acquisition system, a polarisation camera and the topology searching algorithms described in chapter 7.

The thesis has consistently emphasised the ubiquitous nature of optical singularities, and although there are fields which do not contain singularities [Ber07], the vast majority do, generally occurring whenever three or more plane wave components interfere. The generic nature of phase singularities is not only apparent in diffraction catastrophes, but also in the ‘haze’ of speckle seen in any laser beam. The fractal and scale-invariant properties investigated in chapter 6, namely fractal dimension and loop density scaling, imply that vortex lines in three-dimensional random fields exhibit universal properties.

Further investigations, involving different random wave-distributions would reveal what other geometric properties of tangled vortex lines in random fields are universal, and which properties are system-specific. Distributions other than Gaussian speckle which may be of interest to study include hard-edged apertures and those with larger (or smaller) kurtosis than a Gaussian distribution. The density of phase saddle points and scaling of vortex point densities are related to the second and fourth moments of the distribution of wave-vector magnitudes. This suggests that fields generated with differing values of kurtosis may generate statistically different field topologies and serve to highlight any universal properties of vortex structure.

The experimental reports of compact knots in Gaussian beams in the thesis are very significant. Using polynomials for algebraic knots and embedding them in Gaussian beams has found a region of beam parameter space which contains lots of interesting vortex topologies. For instance, in attempting to numerically optimise a figure eight knot, beams were generated (numerically) which contained linked trefoil knots and three-component links. The figure eight knot itself was not reported in this thesis as the dynamic range of the spatial light modulator was not high enough to encode all Laguerre-Gauss mode amplitudes (some being 10^3 times larger than others). The figure eight knot would be the first non-torus knot to be created in a light beam and as such is still a line of ongoing research, both theoretically and experimentally.

At a personal level, the results of greatest value reported in the thesis are the inequalities which govern vortex topologies in four-wave interference and the algorithms that identified curve topology.

Publications

F. Flossmann, K. O'Holleran, M. R. Dennis and M. J. Padgett. Polarization Singularities in 2D and 3D Speckle Fields. *Phys. Rev. Lett.*, **100**, 203902, (2008).

M. R. Dennis, K. O'Holleran and M. J. Padgett. The fractal shape of speckled darkness - art. no. 69050C. *Complex light and optical forces II*, **6905**, C9050-C9050, (2008).

K. O'Holleran, F. Flossmann, M. R. Dennis and M. J. Padgett. Fractality of light's darkness. *Phys. Rev. Lett.*, **100**, 053902, (2008).

J. B. Götte, K. O'Holleran, D. Preece, F. Flossmann, S. Franke-Arnold, S. M. Barnett and M. J. Padgett. Light beams with fractional orbital angular momentum and their vortex structure. *Opt. Express*, **16**, 993-1006, (2008).

J. Courtial and K. O'Holleran. Experiments with twisted light. *Eur. Phys. J. Special Topics*, **145**, 35-47, (2007).

K. O'Holleran, M. R. Dennis, and M. J. Padgett. Illustrations of optical vortices in three dimensions. *Journal of the European Optical Society - Rapid Publications*, **1**, :06008, (2006).

K. O'Holleran, M. J. Padgett and M. R. Dennis. Topology of optical vortex

lines formed by the interference of three, four and five plane waves. *Opt. Express*, **14**, (7):3039-3044, (2006).

M. J. Padgett, K. O'Holleran, J. Leach and J. Courtial. The topology of vortex lines in light beams. *Topology in ordered phases — Proc. TOP 2005*, 287-294, (2005).

O. Steuernagel, E. Yao, K. O'Holleran and M. J. Padgett. Observation of Gouy-phase-induced transversal intensity changes in focused beams. *J. Mod. Opt.*, **52** (18):2713-2712, (2005).

Bibliography

- [ABSW92] L. Allen, M. W. Beijersbergen, R. J. C. Spreeuw, and J. P. Woerdman. Orbital angular-momentum of light and the transformation of laguerre-gaussian laser modes. *Phys Rev A*, 45(11):8185–8189, Jan 1992.
- [AEVV86] M. Aryal, A. E. Everett, A. Vilenkin, and T. Vachaspati. Cosmic string networks. *Phys. Rev. D.*, 34:434–439, 1986.
- [Ale28] J. W. Alexander. Topological invariants of knots and links. *Trans. Amer. Math. Soc.*, 30:275–306, 1928.
- [AP00] L. Allen and M. J. Padgett. The poynting vector in laguerre-gaussian beams and the interpretation of their angular momentum density. *Opt. Commun.*, 184:67–71, 2000.
- [AZ01] M. Aigner and G. M. Ziegler. *Proofs from THE BOOK*. Springer, New York, 2001.
- [BD00] M. V. Berry and M. R. Dennis. Phase singularities in isotropic random waves. *Proc. R. Soc. Lond. A*, 456:2059–2079, September 2000.
- [BD01a] M. V. Berry and M. R. Dennis. Knotted and linked phase singularities in monochromatic waves. *Proc. R. Soc. Lond. A*, 457:2251–2263, March 2001.
- [BD01b] M. V. Berry and M. R. Dennis. Knotting and unknotting of phase singularities: Helmholtz waves, paraxial waves and waves in 2+1 dimensions. *J. Phys. A: Math. Gen.*, 34:8877–8888, 2001.
- [BD01c] M. V. Berry and M. R. Dennis. Polarization singularities in isotropic random vector waves. *Proc. R. Soc. Lond. A*, 457(2005):141–155,

January 2001.

- [BD07] M. V. Berry and M. R. Dennis. Topological events on wave dislocation lines: birth and death of loops, and reconnection. *J. Phys. A: Math. Theor.*, 40:65–74, 2007.
- [Ber77] M. V. Berry. Regular and irregular semiclassical wavefunctions. *J. Phys. A.*, 10:2083–2091, 1977.
- [Ber78] M. V. Berry. Disruption of wavefronts: statistics of dislocations in incoherent gaussian random waves. *J. Phys. A: Math. Gen.*, 11(1):27–37, 1978.
- [Ber04] M. V. Berry. Optical vortices evolving from helicoidal integer and fractional phase steps. *J. Opt. A: Pure Appl. Opt.*, 6:259–268, 2004.
- [Ber07] M. V. Berry. Vortex-free complex landscapes and umbilic-free real landscapes. *J. Phys. A: Math. Theor.*, 40:F185–F192, 2007.
- [BNW79] M.V. Berry, J. F. Nye, and F. J. Wright. The elliptic umbilic diffraction catastrophe. *Phil. Tran. R. Soc.*, 291:454–483, 1979.
- [BS02] E. Bogomolny and C. Schmit. Percolation model of nodal domains of chaotic wave functions. *Phys. Rev. Lett.*, 88:114102, 2002.
- [BVS90] V. Y. Bazhenov, M. V. Vasnetsov, and M. S. Soskin. Laser beams with screw dislocations in their wavefronts. *JETP Lett.*, 52(8):429–431, October 1990.
- [BW59] M. Born and E. Wolf. *Principles of optics*. Pergamon, Oxford, 1959.
- [CDAP97] J. Courtial, K. Dholakia, L. Allen, and M. J. Padgett. Second-harmonic generation and the conservation of orbital angular momentum with high-order laguerre-gaussian modes. *Phys Rev A*, 56(5):4193–4196, Jan 1997.
- [CGR89] P. Couillet, I. Gil, and F. Rocca. Optical vortices. *Opt Commun*, 73(5):403–408, Jan 1989.
- [Den02] M. R. Dennis. Polarization singularities in paraxial vector fields: morphology and statistics. *Opt Commun*, 213:201–221, 2002.
- [Den04] M. R. Dennis. Local phase structure of wave dislocation lines: twist and twirl. *J. Opt. A: Pure Appl. Opt.*, 6(5):S202–S208, 2004.

- [Den07] M. R. Dennis. Nodal patterns in physics and mathematics. *Eur. J. Phys. Special Topics*, 145:191, 2007.
- [Den08] M. R. Dennis. Topological configurations of optical phase singularities. *In press*, 2008.
- [DES04] V. G. Denisenko, R. I. Egorov, and M. S. Soskin. Measurement of the morphological forms of polarization singularities and their statistical weights in optical vector fields. *JETP Lett.*, 80:17, 2004.
- [Dir31] P. A. M. Dirac. Quantised singularities in the electromagnetic field. *Proc. R. Soc. Lond. A*, 133:60–72, 1931.
- [FSMD05] F. Flossmann, U. T. Schwarz, M. Maier, and M. R. Dennis. Polarization singularities from unfolding an optical vortex through a birefringent crystal. *Physical Review Letters*, 95(25):253901, 2005.
- [FSMD06] F. Flossmann, U. T. Schwarz, M. Maier, and M. R. Dennis. Stokes parameters in the unfolding of an optical vortex through a birefringent crystal. *Opt. Express*, 14(23):11402–11411, 2006.
- [FYH⁺85] P. Freyd, D. Yetter, J. Hoste, W. B. R. Lickorish, K. Millett, and A. Oceanu. A new polynomial invariant of knots and links. *Bull. Amer. Math. Soc.*, 12:239–246, 1985.
- [Goo85] J. W. Goodman. *Statistical Optics*. John Wiley & Sons Inc, 1985.
- [GOP⁺08] Jörg B. Götte, Kevin O’Holleran, Daryl Preece, Florian Flossmann, Sonja Franke-Arnold, Stephen M. Barnett, and Miles J. Padgett. Light beams with fractional orbital angular momentum and their vortex structure. *Opt. Express*, 16(2):993–1006, 2008.
- [HK95] M. B. Hindmarsh and T. W. B. Kibble. Cosmic strings. *Rep. Prog. Phys.*, 58:447–562, 1995.
- [HMS⁺92] N. R. Heckenberg, R. McDuff, C. P. Smith, H Rubinsztein-Dunlop, and M. J. Wegener. Laser-beams with phase singularities. *Opt Quant Electron*, 24(9):S951–S962, Jan 1992.
- [Jon85] V. Jones. A polynomial invariant for knots via von neumann algebras. *Bull. Am. Math. Soc.*, 12:103–111, 1985.
- [KBS01] D. Kivotides, C. F. Barenghi, and D. C. Samuels. Fractal dimension

- of superfluid turbulence. *Phys. Rev. Lett.*, 87:155301, 2001.
- [Kib07] T. W. B. Kibble. Phase-transition dynamics in the lab and the universe. *Physics Today*, 60:47–52, 2007.
- [LDCP04a] J. Leach, M. R. Dennis, J. Courtial, and M. J. Padgett. Knotted threads of darkness. *Nature*, 432:165, November 2004.
- [LDCP04b] J. Leach, M. R. Dennis, J. Courtial, and M. J. Padgett. Laser beams: Knotted threads of darkness. *Nature*, 432(7014):165–165, Jan 2004.
- [LDCP05] J. Leach, M. R. Dennis, J. Courtial, and M. J. Padgett. Vortex knots in light. *New J. Phys.*, 7:55, February 2005.
- [LPS⁺07] K. Lindfors, A. Priimagi, T. Setälä, A. Shevchenko, A. T. Friberg, and M. Kaivola. Local polarization of tightly focused unpolarized light. *Nat. Photon.*, 1:228, 2007.
- [LYP04] J. Leach, E. Yao, and M. J. Padgett. Observation of the vortex structure of a non-integer vortex beam. *New J. Phys.*, 6:71, 2004.
- [Mil68] J. Milnor. *Singular points in complex hypersurfaces*. Princeton University Press, 1968.
- [MT06] A. Mitani and M. Tsubota. Self-organization of vortex-length distribution in quantum turbulence: An approach based on the barabasi-albert model. *Phys. Rev. B.*, 74:024526, 2006.
- [NB74] J. F. Nye and M. V. Berry. Dislocations in wave trains. *Proc. R. Soc. Lond. A*, 336:165–190, 1974.
- [NN87] K. W. Nicholls and J. F. Nye. Three-beam model for studying dislocations in wave pulses. *J. Phys. A: Math. Gen.*, 20:4673–4696, 1987.
- [Nye83a] J. F. Nye. Lines of circular polarization in electromagnetic wave fields. *Proc. R. Soc. Lond. A*, 389:279–290, 1983.
- [Nye83b] J. F. Nye. Polarization effects in the diffraction of electromagnetic waves: the role of disclinations. *Proc. R. Soc. Lond. A*, 387:105–132, 1983.
- [Nye99] J. F. Nye. *Natural focusing and fine structure of light*. Institute of Physics Publishing, 1999.
- [Nye03] J. F. Nye. From airy rings to the elliptic umbilic diffraction catastro-

- phe. *J. Opt. A: Pure Appl. Opt.*, 5:503–510, 2003.
- [Nye04] J. F. Nye. Local solutions for the interaction of wave dislocations. *J. Opt. A: Pure Appl. Opt.*, 6:S251–S254, 2004.
- [Nye06] J. F. Nye. Dislocation lines in the hyperbolic umbilic diffraction catastrophe. *Proc. R. Soc. Lond. A*, 462(2072):2299–2313, August 2006.
- [OPD06] K. O’Holleran, M. J. Padgett, and M. R. Dennis. Topology of optical vortex lines formed by the interference of three, four, and five plane waves. *Opt Express*, 14(7):3039–3044, Jan 2006.
- [OW07] E. Orlandini and S. G. Whittington. Statistical topology of closed curves: Some applications in polymer physics. *Reviews of Modern Physics*, 79(2):611, 2007.
- [Pap84] A. Papoulis. *Probability, random variables, and stochastic processes*. McGraw-Hill Companies, 1984.
- [RA01] J. Ruostekoski and J. R. Anglin. Creating vortex rings and three-dimensional skyrmions in bose-einstein condensates. *Phys. Rev. Lett.*, 86(18):3934–3937, 2001.
- [RLS97] D. Rozas, C. T. Law, and G. A. Swartzlander. Propagation dynamics of optical vortices. *J. Opt. Soc. Am. B*, 14(11):3054–3065, 1997.
- [Rol03] D. Rolfsen. *Knots and Links*. American Mathematical Society, 2003.
- [SAM93] D. Stauffer, A. Aharony, and B. B. Mandelbrot. Self-similarity and covered neighbourhoods of fractals: A random walk test. *Physica A.*, 196:1–5, 1993.
- [Sch88] K. W. Schwarz. Three-dimensional vortex dynamics in superfluid He4: homogeneous superfluid turbulence. *Phys. Rev. B*, 38:2398–2416, 1988.
- [SWNA07] D. R. Scherer, C. N. Weiler, T. W. Neely, and B. P. Anderson. Vortex formation by merging of multiple trapped bose-einstein condensates. *Phys. Rev. Lett.*, 98:110402, 2007.
- [Tal36] H. F. Talbot. Facts relating to optical science. *Philos. Mag.*, 9:401–407, 1836.

- [TGCS06] J. S. Tyo, D. L. Goldstein, D. B. Chenault, and J. A. Shaw. Review of passive imaging polarimetry for remote sensing applications. *Appl. Opt.*, 45:5453, 2006.
- [TRS⁺96] G. A. Turnbull, D. A. Robertson, G. M. Smith, L. Allen, and M. J. Padgett. The generation of free-space laguerre-gaussian modes at millimetre-wave frequencies by use of a spiral phaseplate. *Opt. Commun.*, 127:183–188, December 1996.
- [TSM07] H. Tsai, H. Smith, and R. Menon. Fabrication of spiral-phase diffractive elements using scanning-electron-beam lithography. *J Vac Sci Technol B*, 25(6):2068–2071, 2007.
- [VV84] T. Vachaspati and A. Vilenkin. Formation and evolution of cosmic strings. *Phys. Rev. D.*, 30:2036–2044, 1984.
- [VW79] J. M. Vaughan and D. V. Willetts. Interference properties of a light-beam having a helical wave surface. *Opt Commun*, 30(3):263–267, Jan 1979.
- [WFW⁺04] T. Watanabe, M. Fujii, Y. Watanabe, N. Toyama, and Y. Iketaki. Generation of a doughnut-shaped beam using a spiral phase plate. *Rev Sci Instrum*, 75(12):5131–5135, 2004.
- [WHMT05] W. Wang, S. G. Hanson, Y. Miyamoto, and M. Takeda. Experimental investigation of local properties and statistics of optical vortices in random wave fields. *Phys. Rev. Lett.*, 94:103902, 2005.
- [Wol50] H. Wolter. Zur frage des lichtweges bei totalreflexion. *Z. Naturforschg.*, 5:276–283, 1950.
- [WS83a] A. T. Winfree and S. H. Strogatz. Singular filaments organize chemical waves in three dimensions .1. geometrically simple waves. *Physica D*, 8:35–49, 1983.
- [WS83b] A. T. Winfree and S. H. Strogatz. Singular filaments organize chemical waves in three dimensions .2. twisted waves. *Physica D*, 9:65–80, 1983.
- [WS83c] A. T. Winfree and S. H. Strogatz. Singular filaments organize chemical waves in three dimensions .3. knotted waves. *Physica D*, 9:333–345, 1983.